Subsurface Damage Detection in CFRP using Dynamic Shear Strain Analysis of Lamb Wave

MD. SANAUL RABBI

Department of Advanced Technology Fusion
Graduate School of Science and Engineering
Saga University, Japan

September 2018

APPROVAL

Graduate School of Science and Engineering, Saga University
1 Honjomachi, Saga 840-8502, Japan

Certificate of Approval

This is to certify that the Ph.D. dissertation submitted by

MD. SANAUL RABBI

Titled "Subsurface Damage Detection in CFRP using Dynamic Shear Strain Analysis of Lamb Wave" has been approved by the dissertation committee of Doctor of Philosophy (Ph.D.) in the department of Advanced Technology Fusion at the September 2018.

Dissertation Committee

Supervisor: Professor. Dr. Kenbu TERAMOTO
Department of Advanced Technology Fusion, Saga University

Member: Professor Dr. Takeshi TSUJIMURA
Department of Advanced Technology Fusion, Saga University

Member: Professor Dr. Naohiro UENO
Department of Advanced Technology Fusion, Saga University

Member: Associate Professor Dr. Md. Tawhidul Islam KHAN
Department of Advanced Technology Fusion, Saga University

ABSTRACT

Carbon Fibre Reinforced Polymer (CFRP) is a reliable and light fibre-reinforced plastic which contains carbon fibre, nowadays are extensively used wherever high strength-to-weight ratio and rigidity are required, such as aerospace, automotive, structures, sports goods and technical applications. The material properties of such kind of composites depend on the strength-providing part, carbon fibre, and the bonder of the reinforcements together, a polymer resin. Composites offer the designer a combination of properties not available in traditional materials. As with all materials that are used to make objects and structures, there is a need to be able to inspect the equipment to determine its fitness for purpose or use. Inspection of composite material poses a particular challenge since the materials are often non-homogeneous and anisotropic. Flaws can occur in composites at any stage of the lifecycle, i.e., during production or in-service, most likely in fibre distribution or the matrix. Typical examples of flaws found in composites are delamination, cracks, disbonds, impact, fibre breakage, voids, etc.

The integrity and degradation of composite structures have been traditionally evaluated by nondestructive testing (NDT) or by nondestructive evaluation (NDE), now being potentially assessed by structural health monitoring (SHM), to assure the performances of these structures. The detection of flaws is vital in ensuring the safety and timely repair of structures. In comparison with conventional NDE techniques such as ultrasonic scanning and radiography which have been well developed over half a century, damage identification using Lamb waves is in a stage of burgeoning development. Lamb waves are guided waves having dispersive behaviors that propagate in the thin plate or shell structures. The use of Lamb wave in SHM is attractive for the last couple of decades since a large area of structure can be interrogated from only a few locations. The detection of damages comes from the interaction of Lamb waves with disturbances in the compositions.

In 2011, Prof. Teramoto has proposed a novel NDE technique named by dy-

namic shear strain analysis [90]. In this research, the effectiveness of dynamic shear strain analysis is assessed to detect the subsurface damage in the composite laminates. The technique focusing on the near-field imaging method over the fundamental mode of antisymmetric Lamb wave field. The incoming wave field strikes at the boundary of the flaw generates evanescent wave field which diminishes exponentially. The orthogonal pair of out-of-surface shear strains follows linearity condition in the flawless region. In contrast, at the boundary of the defect, the requirement violates as the scattered wave field does not follow the path of incident one. A covariance matrix consisting the vector of shear strain has been adopted in such way that the determinant of the matrix exhibits any value other than zero at the region of violation. As a whole, the image of the defect is reconstructed. This thesis makes explicit the applicability of the dynamic shear strain analysis to orthotropic material in the context of unidirectional, bi-directional, and quasi-isotropic laminate by means of numerical experiments.

ACKNOWLEDGEMENT

At the outset, I would first want to express my gratitude to almighty for the gifts that I have been given which have allowed me to travel so far in life.
Working on Ph.D. has been a wonderful and great exciting experience. But, it is hard to complete the Ph.D. dissertation without the bits of help and supports of the people around me. During my tenure in the Ph.D., I am indebted to many people for their efforts in favor of me.
First and foremost, the guidance and encouragement provided by my supervisor Professor Kenbu Teramoto are much appreciated. I am thrilled to say, he was not just my thesis advisor but is also a great mentor and friend. I am significantly indebted to him for his inspirational and valuable guideline, encouragement and patience. His suggestions and support have been invaluable towards the completion of this thesis work.
I would like to thank my co-supervisor Dr. Md. Tawhidul Islam Khan for introducing me to Professor Teramoto and especially for his advice, support and thoughtful discussions over my stay here. His motivation and constant encouragement helped me a lot to look forward to the future with enthusiasm and confidence in my abilities.
Next, I would like to acknowledge the support of the members from Ulterasonic laboratory, especially Mr. Nishiwaki Hiroki. I will always remember him for his sincere friendship, encouragement, and supports he has provided me at the very beginning of my Japan life.
I am thankful to MEXT (Ministry of Education, Culture, Sports, Science, and Technology, Japan) for providing me the Monbukagakusho scholarship during my entire study life in Saga University, Japan.
I also acknowledge with gratitude and thanks to the authority of Chittagong University of Engineering and Technology (CUET) for granting my study leave. I would like to express my sincere thanks to all faculty members of Mechanical Engineering Department, CUET, particularly Professor Sajal Chandra Banik for inspiring me to pursue my higher study in Japan. Distinc-

tive thanks to Professor Md. Moinul Islam for his valuable suggestions and criticisms throughout my living in Japan.
Special thanks to all of the members of SABAS (Saga Bangladesh Somity) I met. Your cordial reception and valuable cooperation are sincerely appreciated. I have too many to list everyone, but I must particularly mention Mohendro, Ayon, Rimi, Professor Arif, Junayed Uddin Ahmed, Iqbal Ahmed for tolerating me and making my stay here enjoyable all these years. And last but certainly not least, the support and encouragement from Matiul Islam, Zannatul Kowser, Mostaqur Rahman, Rehnuma Haque played an essential and crucial role in this achievement.
Finally, I want to thank my beloved mother and sister for their enduring patience and encouragement, uncles, aunts, and cousins for their support throughout everything and in particular my wife, Hasfia Zannat, for her reassurance, inspiration and overwhelming positive influence on my life.

LIST OF FIGURES

Fig. 1.1 An overview of potential application fields for SHM techniques 2

Fig. 1.2 Schematic of various steps followed in liquid penetrant testing 3

Fig. 1.3 Sketch of magnetic particle testing 4

Fig. 1.4 Radiographic testing 5

Fig. 1.5 Eddy current testing 6

Fig. 1.6 Acoustic emission testing 7

Fig. 1.7 Pulse echo technique 7

Fig. 1.8 Displacement of the array of points due to longitudinal wave 9

Fig. 1.9 Displacement pattern of points due to transverse wave . . 9

Fig. 1.10 Particle trajectory in Rayleigh wave 10

Fig. 1.11 Orientation of carbon fibre in unidirectional laminate . . . 15

Fig. 1.12 Stacking sequence of fibre in symmetrically balanced laminate 16

Fig. 1.13 Schematic representation of delamination and crack occurred in CFRP 16

Fig. 1.14 Real life examples of typical defects encountered in CFRP 18

Fig. 1.15 CFRP demand projections by weight for the applications analyzed [52] 19

Fig. 2.1 Generalized displacement of a line segment $\mathbf{dx}$. Point $\mathbf{x}_0$ displaces by amount $\mathbf{u}(\mathbf{x}_0)$, whereas the other end point, $\mathbf{x}_0 + \mathbf{dx}$, displaces by $\mathbf{u}(\mathbf{x}_0 + \mathbf{dx})$ 24

Fig. 2.2 Deformation follows (a) pure share (b) pure rotation characteristics 25

Fig. 2.3 An elastic half space 35

Fig. 2.4 Lines along two succeeding peaks of the plane wave . . . 38

Fig. 2.5 Elastic half space with a plane compressional wave incident on the boundary 39

Fig. 2.6 The reflected compressional and shear wave 41

Fig. 2.7 Elastic half space with a plane shear wave incident on the boundary 42

Fig. 2.8 A plate of elastic material with free surfaces 43

Fig. 2.9 Wave propagation in a thin plate as a result of superimposing of compressional and shear waves 44

Fig. 2.10 (a) Antisymmetric and (b) symmetric distributions of u_1 . 45

Fig. 2.11 (a) Symmetric and (b) Antisymmetric distributions of u_3 . 45

Fig. 2.12 Lamb wave 48

Fig. 2.13 Fundamental order Lamb wave dispersion curves in a steel plate of 1.00 mm in thickness 50

Fig. 3.1 Waves in solids 52

Fig. 3.2 HTI model due to a system of parallel vertical cracks . . . 53

Fig. 3.3 Material behavior symmetric with a plane 58

Fig. 3.4 Material behavior symmetric with two orthogonal plane . 60

Fig. 3.5 In a homogeneous anisotropic medium, the group-velocity (ray) vector points from the source to the receiver (angle ϑ). The corresponding phase-velocity (wave) vector is orthogonal to the wavefront (angle θ) 71

Fig. 3.6 Wave packet advancing forward in isotropic media, i.e. envelope and carrier wave forwarding in the same direction 72

Fig. 4.1 Calculated A_0-mode phase velocity dispersion curves for HTI material 75

Fig. 4.2 Theoretically calculated angular dependency of phase velocity of the A_0-mode Lamb wave for $f = 30$ kHz 77

Fig. 4.3 Polar variation of phase velocity of the A_0-mode Lamb wave for $f = 30$ kHz 77

Fig. 4.4 Theoretically calculated A_0-mode dispersion curve for 30° fiber direction 78

Fig. 4.5 Theoretically calculated A_0-mode dispersion curve for 60° fiber direction 79

Fig. 4.6 Procedure of distance measurement from the middle plane to the layer of CL to calculate ABD matrix 80

Fig. 4.7 Fibre orientation of $[0, \pm 45, 90]_s$ QI laminate 82

Fig. 4.8 Stacking sequence of (Left) $[0, \pm 45, 90]_s$ QI laminate and (Right) $[(0, 90)_2]_s$ cross-ply laminate 82

Fig. 4.9 Fibre orientation of $[(0, 90)_2]_s$ cross-ply laminate 84

Fig. 5.1 Geometrical relation among the plane wave and the cylindrical defect 86

Fig. 6.1 3D model plate meshing in flawless region 95

Fig. 6.2 Fiber direction (red arrow) along the horizontal axis, blue vertical line indicates the model boundary 96

Fig. 6.3 Wave propagation in HTI model at 20 μs after irradiation (x axis indicates the fibre direction) 96

Fig. 6.4 Meshing of the 3D model surround the defect 97

Fig. 6.5 3D FE zoomed in model at the cylindrical hole defected region 97

Fig. 6.6 Geometrical specifications and schematic diagram of the configuration for FE simulations 98

Fig. 6.7 Typical contour snapshots of FE simulated out-of-plane displacement for the $[0]_8$ laminate at different time instances, (a) soon after excitement at 3 μs, (b) just after A_0-mode Lamb wave interaction with a 1 mm diameter circular subsurface defect at 7 μs, (c) wave after leaving the defected zone at 11 μs, and (d) wavefront just before arriving on the boundary at 14 μs. 105

Fig. 6.8 Normalized amplitude of the (a) reflected and (b) transmitted waves from a 1 mm diameter circular subsurface defect as a function of θ by 30 kHz incident wave. 106

Fig. 6.9 Amplitude comparison between the flawless plate and defected plate during the interaction of 30 kHz incident A_0-mode Lamb wave and 1 mm subsurface defect after 14 μs of the excitement at the boundary of the defect for (a) $[0]_8$ laminate, (b) $[30]_8$ laminate, (c) $[60]_8$ laminate. . . . 107

Fig. 6.10 Amplitude comparison between the flawless plate and defected plate during the interaction of 30 kHz incident A_0-mode Lamb wave and 1 mm subsurface defect after 14 μs of the excitement at the boundary of the defect for (a) $[90]_8$ laminate, (b) $[(0,90)_2]_s$ laminate, (c) $[0,\pm45,90]_s$ laminate. 108

Fig. 6.11 DP for (a) $[0]_8$ laminate, (b) $[30]_8$ laminate, (c) $[60]_8$ laminate at the boundary of the subsurface defect after interaction with 30 kHz incident wave. 109

Fig. 6.12 DP for (a) $[90]_8$ laminate, (b) $[(0,90)_2]_s$ laminate, (c) $[0,\pm45,90]_s$ laminate at the boundary of the subsurface defect after interaction with 30 kHz incident wave. 110

Fig. 6.13 Out-of-plane displacement distribution in a $[0]_8$ flawless laminate after 7 μs micro-s of irradiation 111

Fig. 6.14 Analysis process of orthogonal pair of shear strains by *Sobel* filtering 111

Fig. 6.15 Calculated determinant of the covariance matrix corresponding to the out-of-plane displacement in a flawless specimen, normalized by its maximum value 112

Fig. 6.16 Snapshot of out-of-surface displacement and calculated distribution of normalized determinant after 14 μs after irradiation for $[0]_8$ laminate (dashed circle indicates the original position of artificial cylindrical defect) 113

Fig. 6.17 Snapshot of out-of-surface displacement and calculated distribution of normalized determinant after 14 μs after irradiation for $[30]_8$ laminate (dashed circle indicates the original position of artificial cylindrical defect) 114

Fig. 6.18 Snapshot of out-of-surface displacement and calculated distribution of normalized determinant after 14 μs after irradiation for $[60]_8$ laminate (dashed circle indicates the original position of artificial cylindrical defect) 115

Fig. 6.19 Snapshot of out-of-surface displacement and calculated distribution of normalized determinant after 14 μs after irradiation for $[90]_8$ laminate (dashed circle indicates the original position of artificial cylindrical defect) 116

Fig. 6.20 Snapshot of out-of-surface displacement and calculated distribution of normalized determinant after 14 μs after irradiation for $[(0,90)_2]_s$ laminate (dashed circle indicates the original position of artificial cylindrical defect). 117

Fig. 6.21 Snapshot of out-of-surface displacement and calculated distribution of normalized determinant after 14 μs after irradiation for $[0,\pm45,90]_s$ laminate (dashed circle indicates the original position of artificial cylindrical defect). . 118

Fig. 7.1 Example of defect to be studied 121

Fig. 7.2 A wavelet advancing toward the defect in anisotropic material 122

CONTENTS

Abstract ii

Acknowledgement iii

List of Figures xi

1 INTRODUCTION 1

1.1 Background and motivation 1

1.2 Conventional Techniques on NDT 2

1.3 Modes of Sound Wave Propagation in Elastic Solid 8

1.3.1 Longitudinal Wave 8

1.3.2 Transverse Wave 9

1.3.3 Surface wave (Rayleigh Wave) 10

1.3.4 Plate wave (Lamb Wave) 10

1.4 Overview on Lamb wave based NDT 11

1.5 Introduction to CFRP 14

1.5.1 Classification of CFRP laminate 14

1.5.2 Common defects in CFRP 16

1.5.3 Application and demand of CFRP 18

1.6 Objective 20

1.7 Thesis outline 20

2 FUNDAMENTALS OF LAMB WAVES 23

2.1 Linearized theory of elasticity 23

2.2 Steady-state two-dimensional wave 35

2.2.1 Reflection of compressional wave 39

2.2.2 Reflection of shear wave 41

2.3 Lamb waves 43

2.4 Velocity dispersion of Lamb waves 49

2.5 Lamb waves in multiple layer 50

3 ANISOTROPIC WAVE PROPAGATION 52

3.1 Anisotropic Symmetry Classes 53

3.2 Plane waves in HTI media 64

3.3 Concept of Group velocity 70

4 MATERIAL PROPERTIES AND MECHANICS OF COMPOSITE LAMINATES 73

4.1 Properties of material 74

4.2 Mechanics of composite laminates 79

4.2.1 Quasi-Isotropic (QI) laminate 81

4.2.2 Cross-ply laminate 83

5 DYNAMIC SHEAR STRAIN ANALYSIS 85

6 NUMERICAL EXPERIMENTS 94

6.1 Finite element model 94

6.2 Interaction of A_0-mode Lamb wave with subsurface defect . . . 98

6.3 Data Analysis 101

6.4 Experimental results and discussion 103

7 CONCLUSION 119

7.1 Future work 121

Bibliography 124

1

INTRODUCTION

1.1 BACKGROUND AND MOTIVATION

In structural designs, the trend is always to become more ambitious. For example, buildings get taller, bridges get longer and aircrafts get bigger. This lead to an increase in the requirement to provide both cost savings concerning maintenances and safer environments by preventing structural failures. One of the possible means to achieve this goal is by the application of the Structural Health Monitoring (SHM) systems (Fig.1.1). By providing additional safety measures, the SHM systems enable the life of the structures to be maximized and reduce the structural life costs.
Nowadays, CFRP materials have been a growing popularity in a wide spectrum of the industries. They have been extensively used in the engineering process and become an important material in aircrafts, power plants, constructional structures, ships, cars, rail vehicles, robots, prosthetic devices, sports equipment, etc. CFRP based products offer a better strength-to-weight and stiffness-to-weight ratios due to the reduced weight of the structure. The major advantage of such kind of material is the ability of controllability fiber alignment. Other advantageous properties include good acoustic and thermal insulation, low fatigue and corrosion.
CFRP can be damaged during manufacturing as well as in service by many ways, and these damages are most likely depend on the working environment experienced and the sensitivity of the particular materials used. The mechanism of damage includes static overload, impact, fatigue, hygrothermal effects, overheating, lighting strike, creep, etc. It can be either local or covering a wide area. Damage constitutes a severe discontinuity because they do not transfer interlaminar shear stresses and, under compressive loads, they can cause rapid and catastrophic buckling failure [1]. The integrity of such

structures needs to be determined NDT to assure the performance of service.

(a) Wind turbine inspection (*photo courtesy of Kaufer online*).

(b) Aircraft fuselage inspection (*photo courtesy of Sandia National Lab.,USA*).

(c) Bridge inspection (*photo courtesy of Aspen Aerials, USA*).

Fig. 1.1: An overview of potential application fields for SHM techniques

1.2 CONVENTIONAL TECHNIQUES ON NDT

NDT methods are developed to detect and characterize flaws and also to determine the material properties of the test specimen. The development of computational tools, along with a more widespread understanding made it possible to devise techniques for NDT. There has no clearly defined boundary for NDT [38]; traditionally, it is considered that there are five primary and established methods that are discussed below:

Liquid Penetrant Testing (PT)

PT is thought of one of the most widely used NDT methods in the detection of surface discontinuities in nonporous solid materials. It is a popular way of NDT as it is useful for both magnetic and nonmagnetic materials. The technique focuses on the ability of a liquid to be drawn into a clean surface discontinuity by capillary action. After a period usually called the "dwell time", excess surface penetrant is removed and a developer applied. The developer acts as a blotter that draws the penetrant from the discontinuity. Several steps following in PT method are schematically illustrated in Fig.1.2. PT inspection offers the advantage of a visual inspection by making defects easier to see for the inspector.

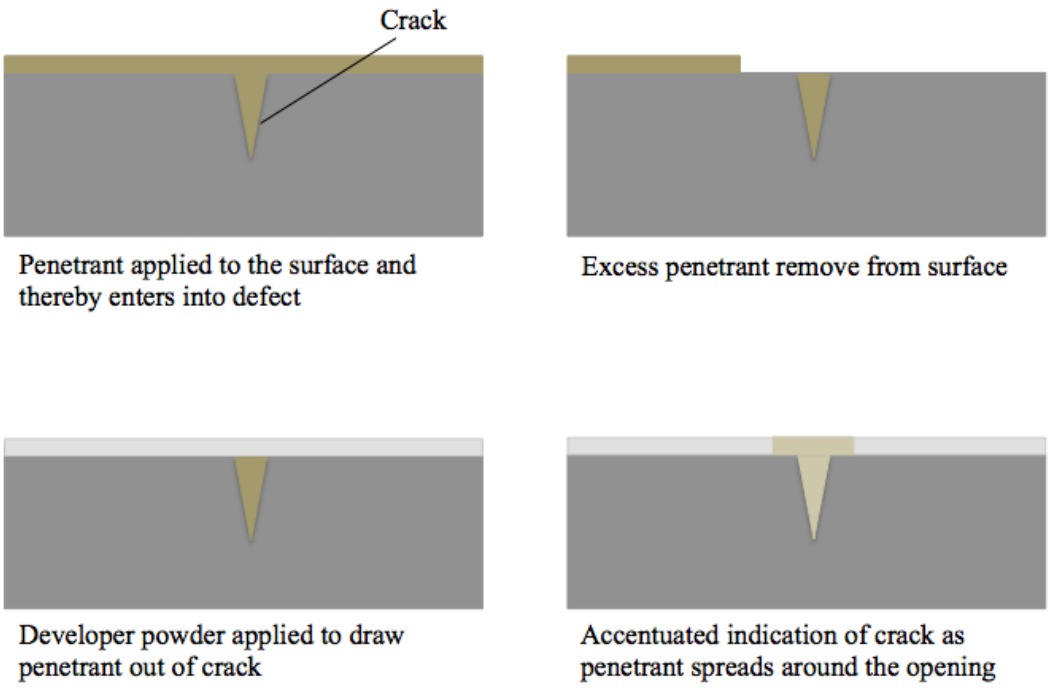

Fig. 1.2: Schematic of various steps followed in liquid penetrant testing

Magnetic Particle Testing (MT)

MT is one of the most widely utilized NDT methods since it is fast and relatively easy to apply. Part surface preparation for MT is not as critical as it is for some other methods. MT can be used to inspect a variety of product forms including castings, forgings, and weldments. To magnetize the component be investigated is the first step of MT. Presence of any defects on or near the surface will create a leakage field. After the component has been magnetized, iron particles are employed to the surface of the magnetized part either in a dry or wet suspended form. The particles will be attracted and cluster at the flux leakage fields, thus forming a visible indication that the inspector can detect (Fig.1.3). MT works best for flaws which are elongated rather than round.

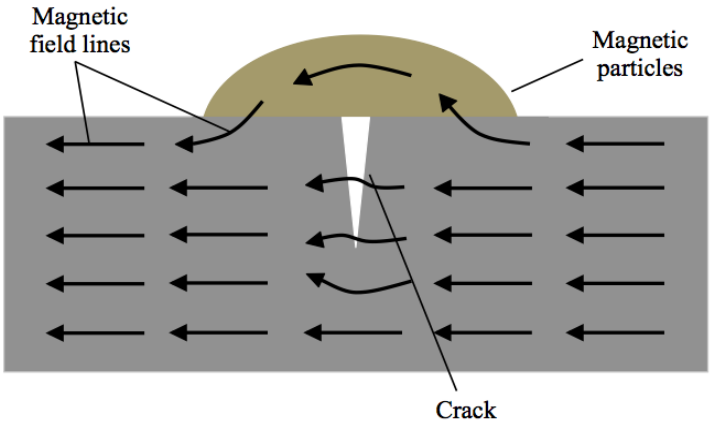

Fig. 1.3: Sketch of magnetic particle testing

Radiographic Testing (RT)

RT is practiced in a wide range of applications including medicine, engineering, forensics, security, etc. In NDT, radiography is one of the most important and widely employed methods. In RT, the part to be inspected is placed between the radiation source and a piece of radiation sensitive film. The ra-

diation that passes through the component will expose the film and forms a picture of that. The film solidity depends on the amount of radiation reaching the film through the test component where darker areas indicate more exposure (higher radiation intensity) and lighter areas indicate less exposure (lower radiation intensity). This variation in the image darkness can be used to determine thickness or composition of material and would also reveal the presence of any flaws or discontinuities inside the material (Fig.1.4). The strength of RT is its ability to detect internal, no-linear imperfections whereas the two dimensional views sometimes drawback of the technique[82][51][72].

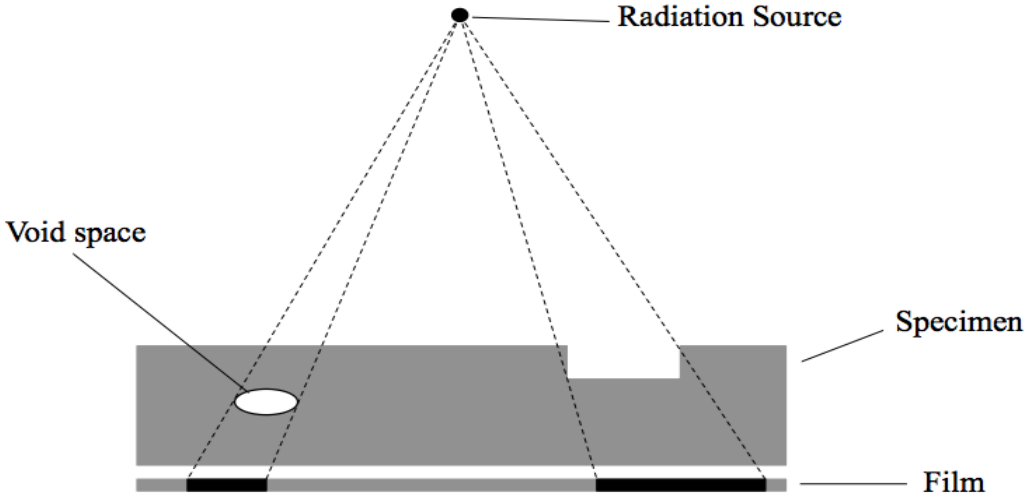

Fig. 1.4: Radiographic testing

Eddy Current Testing (ECT)

ECT instruments are usually small and portable. The method is utilized only on electrically conductive materials, and just a tiny area can be interrogated at a time. An energized electromagnetic coil induces an AC magnetic field into the test specimen. The fluctuating magnetic field generates a circulating electric eddy current. The presence of a flaw increases the resistance to the flow of eddy currents. This is indicated by a deflection on the measuring

instruments (Fig.1.5). It is suitable for detection of surface cracks and subsurface damage as well [82][74].

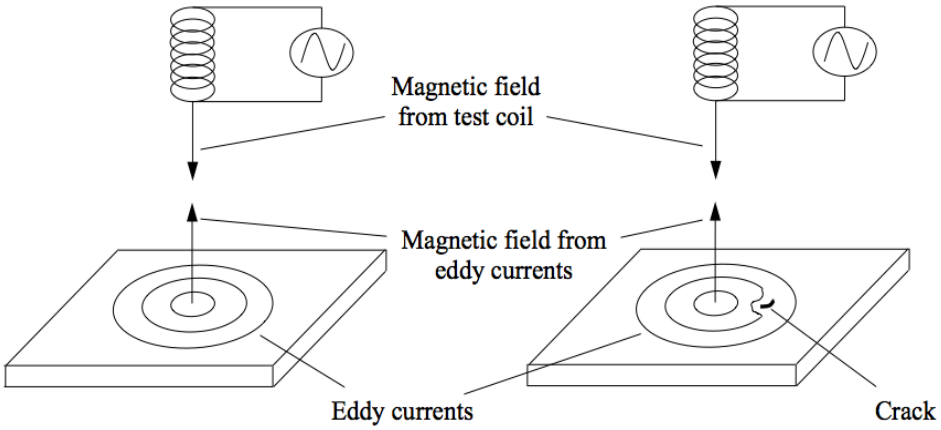

Fig. 1.5: Eddy current testing

Acoustic Emission Testing (AET)

AET can provide the information on the origination of a flaw in a stressed component. The technique based on the concept that discontinuities in parts release energy while subjected to stress. This energy travels in the form of high-frequency stress waves. The waves received with the transducers, converts the energy into the voltage, further processed as AE signal data (Fig.1.6). Analysis of collected data comprises the characterization of the received signals according to their respective source location, voltage intensity, and frequency content [59][82][55][30][21].

Ultrasonic Testing (UT)

UT uses high-frequency sound waves (typically in the range between 0.5 and 15 MHz) to conduct examinations and make measurements. In general, UT

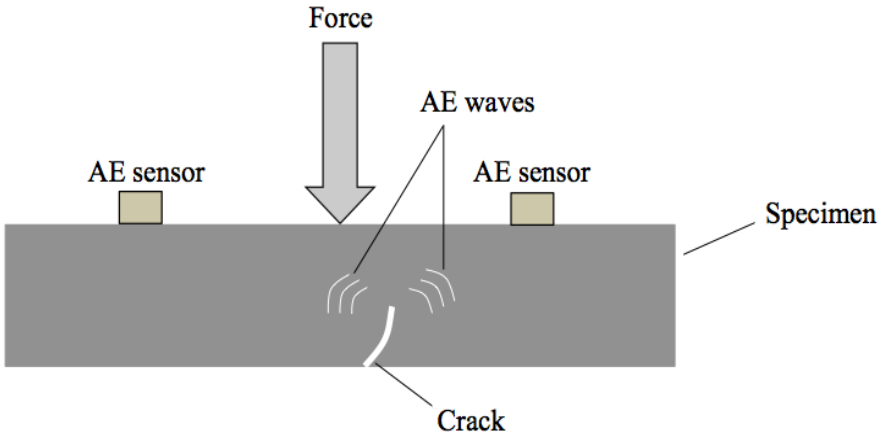

Fig. 1.6: Acoustic emission testing

is based on the capture and characterization of either the reflected waves (pulse-echo) or the transmitted waves (through-transmission). Each of them is used in particular applications, though the former system is more useful since it requires one-sided access to the object. In pulse echo technique, the instrument converts electrical pulses into mechanical vibrations. These pulses travel across the tested specimen and reflect from flaws because of their different acoustic nature. The returning reflected pulses are re-converted to electrical energy and displayed as signals or images. The position and size of these signals correspond to the position and size of the flaws (Fig.1.7). Appropriate choosing of the instrument can display the information in various ways. These techniques are referred as A-, B-, and C-scans. A-scan refers to

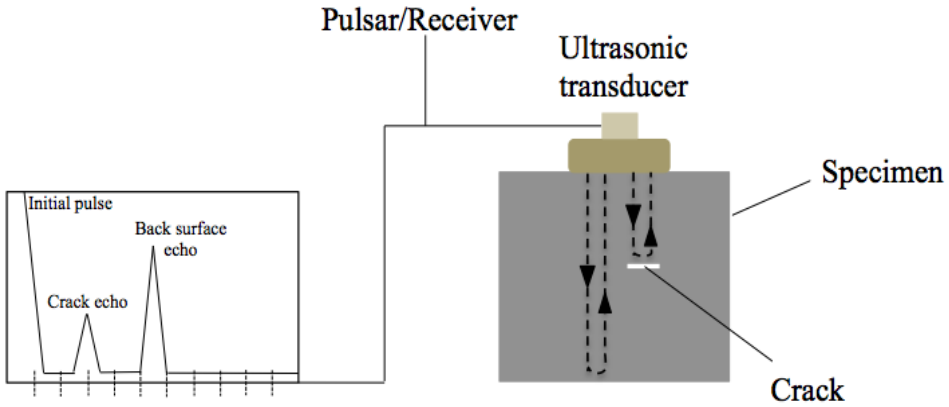

Fig. 1.7: Pulse echo technique

a single point measurement whereas the B-scan measures along a single line. The C-scan nothing but collection of B-scan forming a surface contour plot. In general, this method is highly sensitive to small surface and deep flaws in the material [82][69][38].

1.3 MODES OF SOUND WAVE PROPAGATION IN ELASTIC SOLID

Ultrasound based NDT based on the vibration in materials can be termed as acoustics. Acoustics is focused on particles that contain many atoms that move in harmony to produce a mechanical wave. When the particles of a medium are displaced from their equilibrium positions, internal restoration forces arise. These elastic restoring forces between particles, combined with the inertia of the particles, lead to the oscillatory motions of the medium. In solids, sound waves can propagate in four principal modes that are based on the way the particles oscillate, termed as the longitudinal wave, shear wave, surface wave (Rayleigh wave), and in thin materials as plate wave (Lamb wave).

1.3.1 *Longitudinal Wave*

Longitudinal waves are the waves that transfer energy in the same direction as the disturbance in the medium of propagation (Fig.1.8). Sometimes longitudinal waves are called compressional or compression waves, because they produce compression or rarefaction during traveling through the medium and pressure waves because they provide increases and decreases in pressure. This type of waves include sound waves (particle displacement, the velocity of particles propagated in the elastic media, and vibrations in pressure) and seismic P-waves (created by earthquakes and explosions).

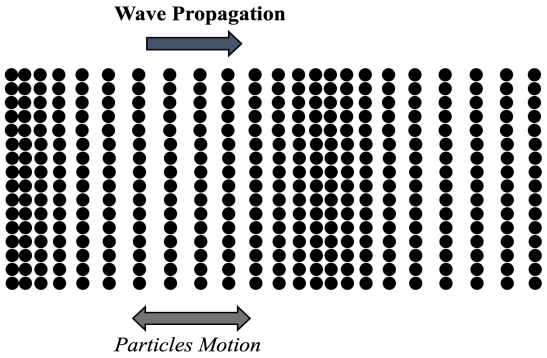

Fig. 1.8: Displacement of the array of points due to longitudinal wave

1.3.2 *Transverse Wave*

In case of transverse waves, the displacement of the medium is in right angle to the direction of wave propagation (direction of energy transfer). If a transverse wave is moving in the horizontal direction, particles motion are in up and down directions that lie in the vertical direction (Fig.1.9). Here the formation of crest and trough takes place at regular interval. Vibration in strings, ripples on the water surface, seismic S-waves and electromagnetic waves are the example of a transverse wave.

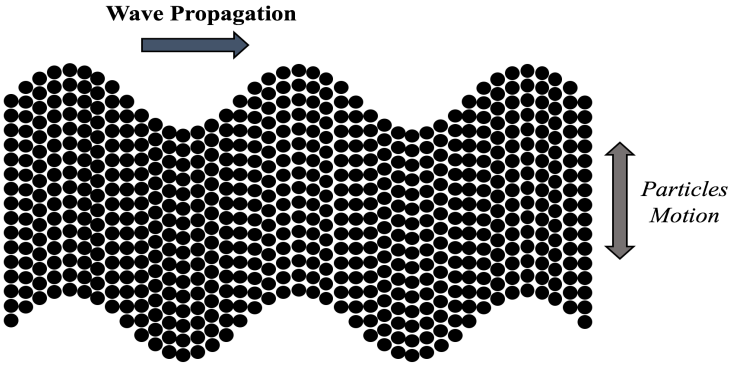

Fig. 1.9: Displacement pattern of points due to transverse wave

1.3.3 *Surface wave (Rayleigh Wave)*

The wave propagating on the surface of an infinite solid half-space is firstly described by Lord Rayleigh [73]. They are always generated when a free surface exists in a continuous boundary and include both longitudinal and transverse motions. In an elastic, homogeneous half space, particle motion on the surface always follow an elliptic path normal to the surface and parallel to the direction of wave propagation whereas the major axis of the ellipse is vertical (Fig. 1.10). Particles motion decrease exponentially in amplitude with the increase of the distance from the surface. This type of surface wave may generate from the massive earthquake and can travel around the globe several times before dissipating.

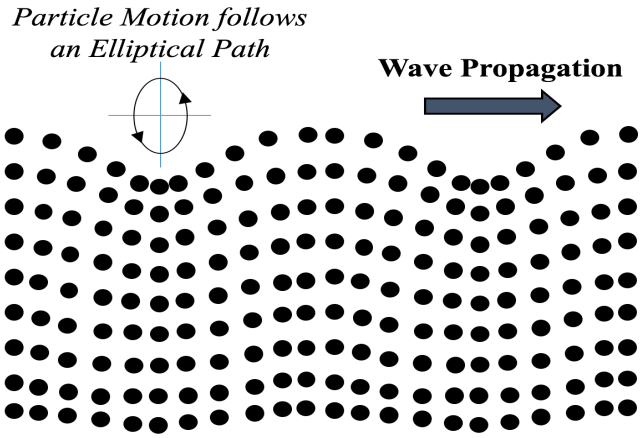

Fig. 1.10: Particle trajectory in Rayleigh wave

1.3.4 *Plate wave (Lamb Wave)*

Though the longitudinal wave and shear wave are most widely used in conventional UT, the application of guided structural waves, i.e., Lamb waves in SHM applications for thin structures gain a high interest within the research communities due to its considerably long propagation ranges [87]. Lamb (or plate) waves are similar to the surface waves and can only be generated in

thin plates. Horace Lamb [54] extended Rayleigh analysis to wave propagating within the free isotropic plates with the parallel surface. They usually produce when a wave strikes a surface at an incident angle where the identical component of the incident source wave velocity is equal to the test specimen wave velocity. The particle motions are similar to the elliptical path for surface waves. Among a number of modes with Lamb wave, symmetrical and anti-symmetrical modes (named by the motion pattern about the mid-plane of the plate) draw a deep concern for their broad applicability in the field of NDT. Lamb wave propagate at high frequencies giving it high resolutions from its smaller wavelengths. This behavior makes Lamb waves sensitive to small damages in the structure i.e. impact damages. The use of lamb waves is potentially a practical solution to detect the damage with traction free boundaries [3]. In this type of elastic wave, particle motion lies in the plane that contains the direction of wave propagation and the plate normal (the direction perpendicular to the plate) [54]. Lamb waves are dispersive and multi-modal causing complicated wave signals and data interpretations in damage detection processes. In general composite materials, these dispersive and multi-modal characteristics are also directionally dependent [70]. The main advantage of Lamb wave is that both sides, as well as the interior of the structure, can be sensed from only one location on one side of the structure, which makes in situ monitoring viable.In general, Lamb waves belong to a family of guided waves, which is guided by the plate boundaries when it propagates. Thus, in literature, it is also known as guided waves in plates. Other classes of guided waves have also been studied in the research. Love showed mathematically that SH waves are also solutions to the wave equation in plates [56] . These waves have a shearing motion in the plane of the plates. Later, Stonely described wave propagating at the interface between two solids [83]. Conditions for the propagating and the leaky wave modes between two solid are given in [79][68]. Leaky waves are the waves that lose its energy to the surrounding.

1.4 OVERVIEW ON LAMB WAVE BASED NDT

NDT systems involving Lamb waves can be classified in two ways [85]:

- Passive system: Only sensors are required to detect the Lamb waves produced by damages in the structures. It deals mainly with the problem of damage localization.
- Active system: Lamb waves are excited into the structures using actuators and sensed by sensors with the damage information. It gives the opportunity for utilizing certain mode types and frequency ranges.

Lamb waves can be generated by many types of transducers [87]. Among them, some well used systems are: Ultrasonic probe, Laser transducers, Piezoelectric transducers, Interdigital/Comb transducers, and Optical fiber transducers.
Following Snell's law, ultrasonic probes are used widely for actuating and sensing of single Lamb modes using angled wedge prism [53, 28, 62, 92]. Besides these contact based innovations, several non-contact methods were introduced like air-coupled [17, 16] and fluid coupled [31] transducers to omit the difficulties arise by the earlier types. The main problems for these transducers are, (i) The required downtime of the inspected structures, and (ii) the inspected structures must be accessible from both sides. Moreover, such methods may be less efficient for detecting near-surface damage [4].
The Lamb waves excitation using the laser-based ultrasonic waves and the lamb wave sensing using the laser interferometers are high precision measurement techniques [37, 95, 29]. Fabry-Perrot and heterodyne interferometers are the most frequently employed devices for this purpose.
The piezoelectric transducers (PZT) deliver excellent performance in Lamb wave generation and acquisition [10, 26, 27]. Easy integration, negligible mass and volume, excellent mechanical strength, wide frequency response, low power consumption, low acoustic impedance are several advantages in using such kind of transducers. Composite versions of PZT transducers are available i.e., the microfiber composites and the active fiber composites [9, 6].
Polyvinylidene fluoride (PVDF) piezoelectric polymer transducer features better flexibility, higher dimensional ability, more stable piezoelectric coefficients over time in comparison with piezoelectric ceramic transducers [45]. This kind of interdigital transducer is suitable to accommodate more versatile applications with reduced cost [61, 13]. Bu was adjusting the space between interdigital electrodes, Lamb waves with controllable wavelength can be pro-

duced by PVDF [60]. PVDF transducers are mainly used as sensors due to the low actuating force.

Optical fibre sensors have been increasingly adopted in damage identification due to its lightweight, wide bandwidth, good compatibility, long life and low power consumption [15]. Fibre Bragg Grating (FBG) sensor is successfully and effectively used in this class to detect the Lamb waves.The embedded FBG sensors have more sensitivity to the Lamb waves than the surface mounted FBG sensor [87].

A proper Lamb mode efficient for damage detection should show several distinguishing characteristics such as (1) non-dispersion, (2) low attenuation, (3) high sensitivity, (4) secure excusability, (5) good detectability and (6) toilets selectivity [100]. As the narrow bandwidth input signal can prevent wave dispersal effectively, windowed tone burst, rather than pulse is frequently adopted as the Lamb signal. The *minimum resolvable distance* (MRD) approach can determined the most suitable cycle number and frequency for a Lamb mode [99]. Modes S_0 and A_0 are usually possess very low MRD values. The basic symmetric mode and anti-symmetric mode are usually used in practice. Although S_0 is preferred in the majority of the studies utilization of A_0 is increasing due to its short wavelength. It was found that S_0 exhibits reasonable sensitivity to defects anywhere in the thickness, while A_0 is more sensitive to surface cracks or corrosion. In particular, it has been shown that A_0 is highly effective for detecting delamination and transverse ply cracks [25, 45, 60, 48, 33].

The Lamb wave signals from the sensors are processed to indicate the presence of damage. Various signal processing and identification techniques are available, in particular: (i) time domain analysis [94, 81, 102], (ii) frequency domain analysis[19, 96, 50, 41], and (iii) integrated time-frequency domain analysis [49, 98, 86, 71].

Except for a few successful applications in damage identification, the direct times series analysis is normally incapable of isolating defect-scattered information appropriately from noise. Moreover, a benchmark signal is essential for comparison. Frequency domain analysis needs a significant volume of the signal captured from different positions, a number of transducers must be ensured to scan the entire structural surface. To overcome the shortcoming of previous two methods, the combination of time information with fre-

quency data is introduced. Rather than direct time-frequency analysis, in practice, several variants are more popular, such as *short time Fourier transform*, *Winger-Ville distribution*, and *Wavelet transform*. From a historical perspective, a wavelet transform is a dominant tool for signal processing than others.
Other signal processing tools that can be used for Lamb wave signal analysis include cepstrum investigation [103], blind deconvolution [104], cyclostationary processes [78] and probability analysis [5].
Concerning in overall damage identification, the Lamb wave based damage identification algorithms can be either forward or inverse. The forward analysis deals with the uniqueness of the solution whereas in case of inverse analysis, the solution can be ambiguous. The triangulation method [48, 94] and the time reversal imaging method [97, 46] are the well known direct analysis for damage detection. Inverse algorithm is well capable iof identifying damage by applying artificial intelligence and tomography [43, 39, 80, 75, 65]. Advanced neural network system is the pivotal technique among all in AI-based method [88, 84, 67].

1.5 INTRODUCTION TO CFRP

CFRP is a composite made with carbon fibres embedded in a polymar, commonly an epoxy matrix. the fibres, which are usually $7 - 15\ \mu$m in diameter, are bundled together to form a tow, which can then be woven into fabric or laid down unidirectionally to form a lamina. A single lamina has a thickness of about $0.05 - 0.2$ mm, and so to obtain suitable mechanical engineering components, many laminae are stacked in same or different directions to form a laminate. This fibre directionality contributes to the anisotropy in CFRP, which means the phase velocity is typically much higher in the fiber direction and lower perpendicular to the fiber direction.

1.5.1 *Classification of CFRP laminate*

Usually, CFRP can be classified according to the fiber orientation, as:

- Unidirectional laminate: In this sort of laminate, the fiber angle in any ply is parallel to the fiber angle in every other ply (Fig.1.11). From a mechanics point of view, this is a thick lamina.
- Cross-ply laminate: Here, the fiber angle in any plane is normal to at least one other rely upon and parallel to any other ply or plies (i.e., contains only 0 and 90° plies)
- Angle-ply laminate: Fibre angle of any ply is not restricted to parallel and normal directions.

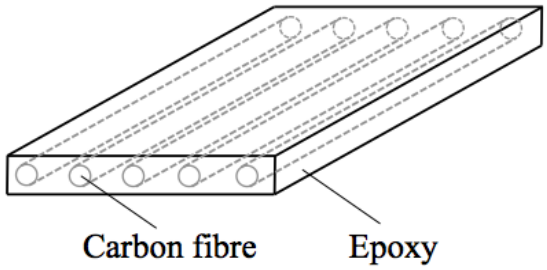

Fig. 1.11: Orientation of carbon fibre in unidirectional laminate

Besides the above sorting criteria, CFRP can also be classified based on the stacking sequence of fiber:

- Symmetric laminate: In a symmetric laminate all plies above the mid plane have the same angle as the ply in the equivalent position below the half space of the material (Fig.1.12). The plane contains the half space acts as the plane of symmetry.
- Antisymmetric laminate: Here, the centerline plane is a plane of antisymmetry, i.e., all plies above this plane have the opposite angle as the ply in the equivalent position below the centerline.
- Asymmetric laminate: the centerline plane of the material does not act either as a plane of symmetry or antisymmetry.

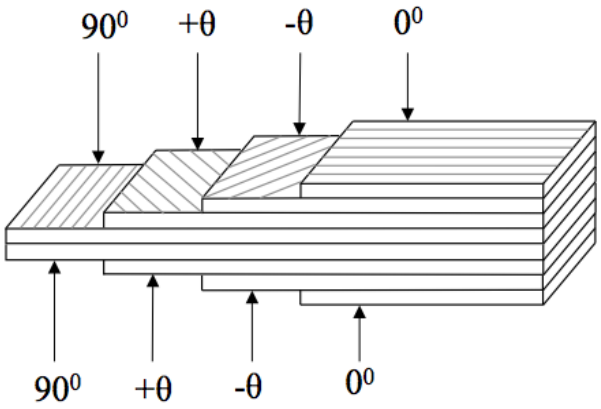

Fig. 1.12: Stacking sequence of fibre in symmetrically balanced laminate

1.5.2 *Common defects in CFRP*

CFRP components encountered various types of damage, and their mechanism might differ one from another based on their physical and mechanical properties, results in the adverse influence in performance. These include in-plane flaws (delamination), across the plane flaws (matrix crack), and volumetric flaws (void). Such flaws can be schematically shown in Fig 1.13. According to the formation of the defect, they can be discussed as follows:

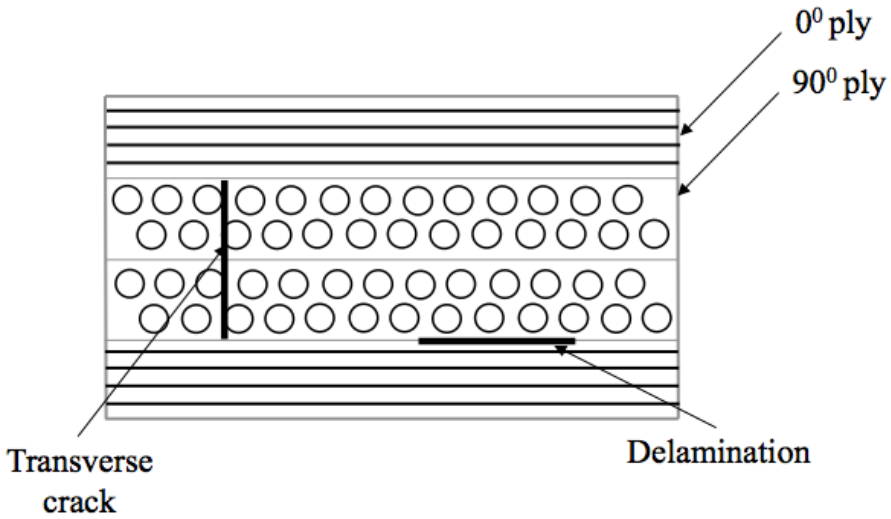

Fig. 1.13: Schematic representation of delamination and crack occurred in CFRP

Impact damage

Impact damage of composites during manufacture and in-service can occur in different locations including near the edge or on the edge of the structure. This kind of defect is the result of foreign object damage such as stone, bird strike, dropping of an object, etc. This defect results in matrix cracks, fibre breaking and delamination in composites. Good correlation has been found between the impact energy and its corresponding damage initiation in glass-fiber composites [105]. A noticeable agreement also been found between the impact and its bad effect on the laminate thickness [24][89] and stacking sequence as well [58]. The impact damage may cause the reduction of residual strength by up to 50% in CFRP [36].

Fibre breakage

Most of the fibres tend to fracture in tension in a brittle manner [44]. Damage is initiated at failure points of weaker fibre which break during initial loading. The shear stresses around those points cause the resin and the interfaces to degrade and leads to crack which propagate along the fibre-matrix interfaces.

Delamination

In composites, repeated cycle stresses, the impact can cause layers to separate with significant loss of mechanical toughness is called delamination. It means the lack of adhesion between two layers of laminates [34]. Due to weak adhesive bonding, fibre pull-out may occur which causes the delamination [47].

Voids

A void is a pore that remains unoccupied in a laminate. Voids in CFRP can regularly occur in small or large. Large voids may be occur during the manufacturing process while small ones are often found adjacent to the fibre. It can affect the mechanical properties of the composite as a void is a non-uniformity in a composite material. It can act as a crack nucleation site as

well as allow moisture to penetrate the composite [44]. A small change in the percentage of void content ($1 - 3\%$) can reduce the mechanical properties of the composite by up to 20% percent. Voids exist in all forms of composite with variations in their incidence depending on the fabrication route and matrix type [14]. Typical defects are shown in Fig. 1.14

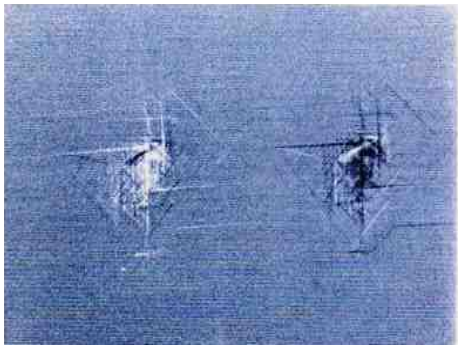

(a) Toughened CFRP panel damaged by impact [35]

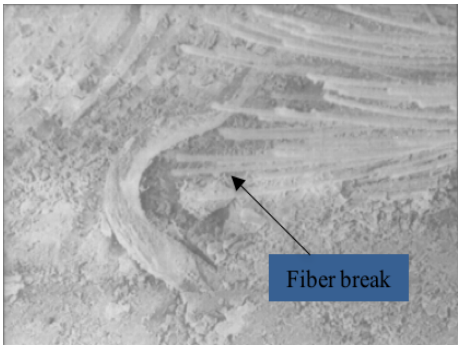

(b) Micrograph of a composite showing broken fiber [36]

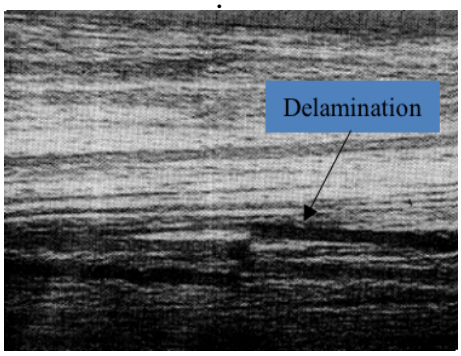

(c) Delamination between fiber layers [42]

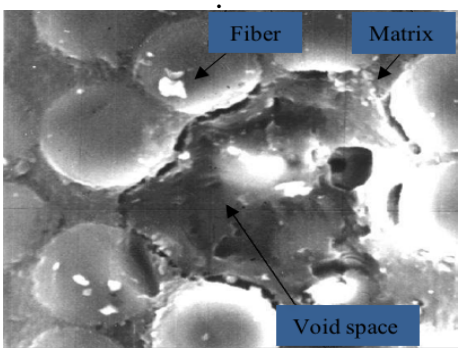

(d) Zoomed view of the CFRP plate having void [42]

Fig. 1.14: Real life examples of typical defects encountered in CFRP

1.5.3 *Application and demand of CFRP*

CFRP composites are usually preferred in the application where strength, low weight, stiffness and outstanding fatigue characteristics are requirements. CFRP allows 'light-weighting' in transportation applications such as auto-

mobiles and aircrafts which leads to the reduction of energy consumption through fuel savings. It is approximated that every 10% of vehicle mass savings results in a $6\% - 8\%$ improvement in fuel economy [23]. This benefit enhances alternative fuel based vehicles to improve fuel economy as well as achieve longer driving distances between refueling. Nowadays in aerospace sector, CFRP offers the best alternative of aluminum and because of that from 2015, the aerospace and aviation sector consumes the most significant amount of CFRP than any other practical field. In case of designing of wind turbines, uses of CFRP enables blade length extension, leading to more wind energy capture per turbine as well as the development of a maximum range of wind resources. Using CFRP in pressure vessel allows the wide range of operating pressure with lighter weight and thus increases the lifespan than the conventional metal-based containers. Other than these sectors, CFRP can exclusively use in oil and gas industry, civil infrastructure, sports utility, marine, etc. Global demand for CFRP in various sectors projected by industry experts with a constant compound annual growth rate (CAGR) of $9 - 10\%$, is shown in Fig. 1.15. Due to growth of end-use industries, in the inevitable

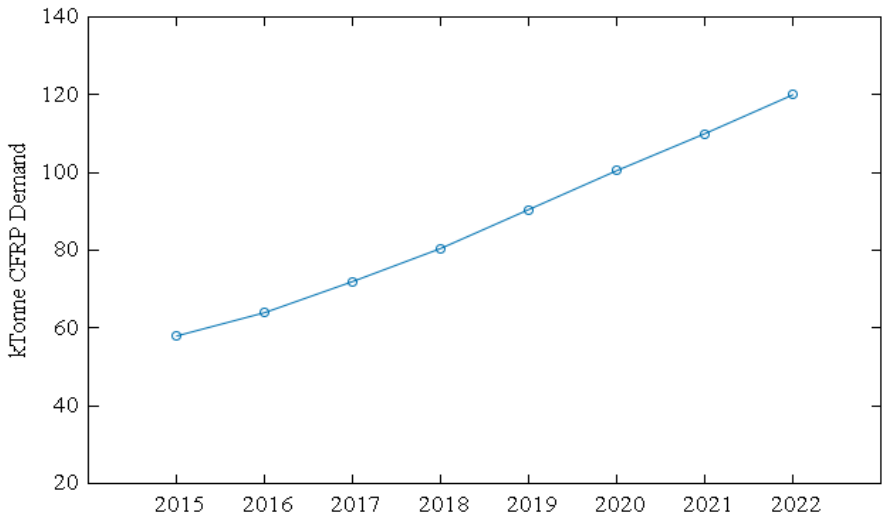

Fig. 1.15: CFRP demand projections by weight for the applications analyzed [52]

future, North America is anticipated to continue its domination as the most extensive market of CFRP.

In contrast with the excellent use of composites in a wide area of industry, it

is inevitable to secure its perfect and secured functional application. NDT of such materials offers a vast area of research.

1.6 OBJECTIVE

The behavior of the Lamb wave propagation in plates needs to be understood first before any meaningful utilization in the NDT applications either through analytical, numerical and experimental investigations. The first step in utilizing Lamb waves is to understand its dispersive behaviors [87]. Study on the Characteristic dispersive curves of fundamental anti-symmetric (A_0) mode Lamb wave for Composite Laminates (CL) thus clears the priority before applying the damage detection technique. Subsurface damages and obstacles in plates are typically detected through the scattering effects of Lamb waves. Analytical perfect solutions to study the scattering phenomena do not exist due to the anisotropic behavior and multilayer characteristics of composite laminates. This study uses a three-dimensional (3D) Finite Element Model (FEM) to provide physical insight into the scattering characteristics of in composite laminates. An analysis of the application of dynamic shear strain technique to detect subsurface damage in CFRP laminates is the primary goal of this thesis.

1.7 THESIS OUTLINE

This thesis discussed the efficient and effective application of the novel near-field imaging technique based on the fundamental anti-symmetric A_0 Lamb wave mode, dynamic shear strain analysis to detect the subsurface damage in anisotropic (CFRP) material.
Focusing on that, the introductory chapter gave the fundamental of the wave propagating modes in elastic solid and NDT techniques existing nowadays with summarized illustration along with the review on Lamb wave based technique in the context of NDT. Following, the background knowledge of CFRP material including its classification and probable types of damage they

are often encountered in the working area are also stated. Later chapters are discussed the following topics.

Chapter 2 gives the fundamentals of Lamb wave. Beside explaining the linearized theory of elasticity and steady state two dimensional wave characteristics, derivation of Lamb wave is discussed in this chapter. The chapter ended up with the velocity dispersion criteria of Lamb wave.

Chapter 3 discusses the wave propagation in anisotropic media. Starting from a perfect anisotropic material, all of the symmetry classes with the derivation of characteristic stiffness matrix for each class are described satisfactorily. The nature of the plane wave propagation in the horizontally transverse isotropic (HTI) media is discussed in the second part of the chapter with the mathematical formulation of the phase velocity.

Based on the deduced phase velocity and frequency equation of Lamb wave in previous chapters, chapter 4 illustrates the velocity dispersion characteristics for unidirectional laminate based on the material properties considered in this study. Besides that, stiffness of bi-directional laminate and quasi-isotropic laminate is evaluated based on the fundamentals mechanics of CL.

The novel near-field imaging technique is discussed in chapter 5. The method deals with the quantitative evaluation in the overlapping region of the incident and scattered wave. For isotropic material, the technique concluded with the image reconstruction of subsurface defect in the vicinity of the defect by considering the time based out-of-plane displacement of each node over the A_0-mode Lamb wave field.

Chapter 6 describes the 3D FEM modeling and simulation for characterization of CFRP. The geometry of probes and tested samples are modeled, and their parameters are set up in the simulation software. The multiphysics explicit software LS-DYNA is used to develop the geometry, meshing, and simulation as well. The interaction of A_0-mode Lamb wave and the subsurface defect for each laminate are characterized by the directivity pattern of the scattered wave at the boundary of the defect. Stored time series data is analyzed using the C program. Numerical results are thoroughly discussed in the later part of the chapter in the context of image reconstruction of the defect for unidirectional, bi-directional and quasi-isotropic laminate.

Chapter 7 concludes the results and achievements of the entire research work.

The future work includes the system development of damage inspection in the anisotropic material.

2

FUNDAMENTALS OF LAMB WAVES

Derivation of Lamb wave equation started with the deformation of an elastic body. An elastic body has a neutral undeformed state to which it returns when all external loads are removed.

2.1 LINEARIZED THEORY OF ELASTICITY

The equations governing the linearized theory of elasticity are presented in the following used notation:

$$\begin{aligned} \text{position vector}: \ & \mathbf{x} \ \ (\text{coordinates} \ \ x_i) \\ \text{displacement vector}: \ & \mathbf{u} \ \ (\text{components} \ \ u_i) \\ \text{strain tensor}: \ & \boldsymbol{\varepsilon} \ \ (\text{components} \ \ \varepsilon_{ij}) \\ \text{stress tensor}: \ & \boldsymbol{\tau} \ \ (\text{components} \ \ \tau_{ij}) \end{aligned}$$

Apart from these, differentiation with respect to a variable will be indicated by a comma followed by an index as:

$$u_{i,j} = \frac{\partial u_i}{\partial x_j}$$

Deformation

When all the particles that make up a body move together without any considerable change in the shape of the body, it can refer to *rigid body motion*. In contrast, if the shape of the body changes, we can refer to this as *deforma-*

tion. To differentiate between this two, we are going to consider the relative motion of neighboring points. Consider the displacement $\mathbf{u}$ of a point at $\mathbf{x}$ corresponding to an arbitrary origin $\mathbf{x}_0$ (Fig.2.1).

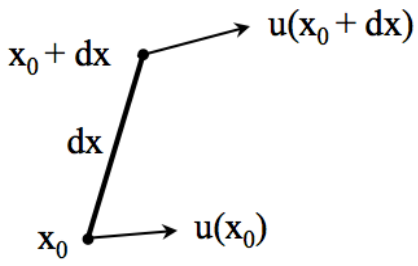

Fig. 2.1: Generalized displacement of a line segment $\mathbf{dx}$. Point $\mathbf{x}_0$ displaces by amount $\mathbf{u}(\mathbf{x}_0)$, whereas the other end point, $\mathbf{x}_0 + \mathbf{dx}$, displaces by $\mathbf{u}(\mathbf{x}_0 + \mathbf{dx})$

The first two terms in a Taylor's series expansion about the origin,

$$u_i(\mathbf{x}) = u_i(\mathbf{x}_0) + \left.\frac{\partial u_i}{\partial x_j}\right|_{x_0} dx_j + \cdots\cdots \qquad i = 1,2,3 \tag{2.1}$$

The first term, $u_i(\mathbf{x}_0)$, represents a *rigid body translation* whereas all neighborhood points of x_0 share the equal displacement. The second term gives the relative displacement in terms of the gradient of the displacements $\frac{\partial u_i}{\partial x_j}$, or $\nabla \mathbf{u}$ in vector notation.

Displacement equation

The partial derivatives $\frac{\partial u_i}{\partial x_j}$ make up the *displacement gradient tensor*, a second rank tensor with nine independent components:

$$\begin{bmatrix} \frac{\partial u_1}{\partial x_1} & \frac{\partial u_1}{\partial x_2} & \frac{\partial u_1}{\partial x_3} \\ \frac{\partial u_2}{\partial x_1} & \frac{\partial u_2}{\partial x_2} & \frac{\partial u_2}{\partial x_3} \\ \frac{\partial u_3}{\partial x_1} & \frac{\partial u_3}{\partial x_2} & \frac{\partial u_3}{\partial x_3} \end{bmatrix} \tag{2.2}$$

The displacement gradient tensor can be distracted into two parts, symmetric and antisymmetric, as follows:

$$u_i(\mathbf{x}) = u_i(\mathbf{x}_0) + \underbrace{\frac{1}{2}\left(\frac{\partial u_i}{\partial x_j} + \frac{\partial u_j}{\partial x_i}\right)}_{\text{Symmetric part}} dx_j + \underbrace{\frac{1}{2}\left(\frac{\partial u_i}{\partial x_j} - \frac{\partial u_j}{\partial x_i}\right)}_{\text{Antisymmetric part}} dx_j + \cdots . \tag{2.3}$$

Symmetric part of the displacement gradient tensor can be defined as *Infinitesimal strain tensor* with six independent components whereas the antisymmetric part can be termed as *Rotation* with remaining three independent components. Symmetric part arises in case of pure shear condition whereas the antisymmetric part takes place in pure rotation condition (Fig.2.2). Neglecting the higher order terms, we can see that the displacement **u(x)** is composed of three components- *rigid body translation*, *strain* and *rigid body rotation*.

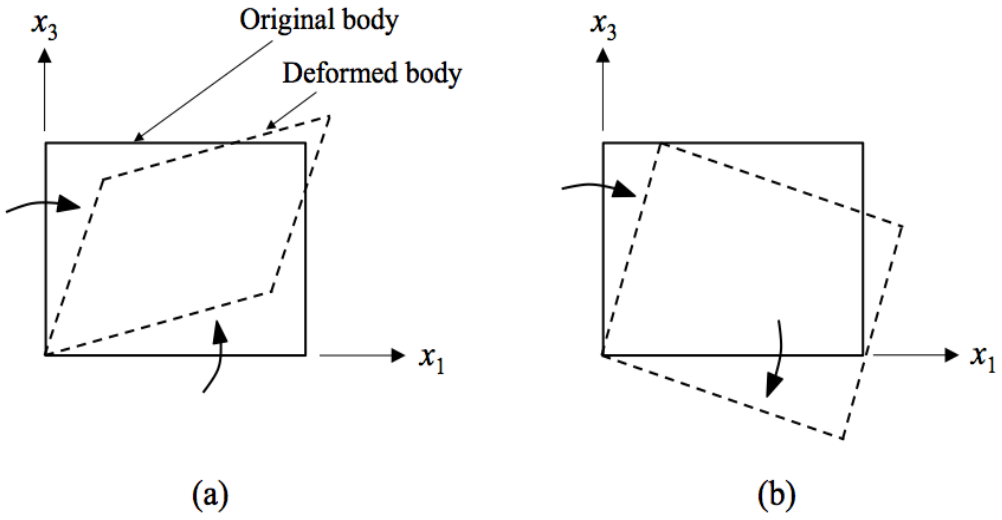

Fig. 2.2: Deformation follows (a) pure share (b) pure rotation characteristics

The Strain Tensor

The infinitesimal strains are given by

$$\varepsilon_{ij} = \frac{1}{2}(u_{i,j} + u_{j,i}) \tag{2.4}$$

The Linear strain tensor in the x_i coordinate system is

$$\varepsilon_{ij} = \begin{bmatrix} \varepsilon_{11} & \varepsilon_{12} & \varepsilon_{13} \\ \varepsilon_{21} & \varepsilon_{22} & \varepsilon_{23} \\ \varepsilon_{31} & \varepsilon_{32} & e_{33} \end{bmatrix} \tag{2.5}$$

The components of the strain tensor ε_{ij}, can be written as:

$$\begin{aligned} \varepsilon_{11} = u_{1,1} &= \frac{\partial u_1}{\partial x_1} \\ \varepsilon_{22} = u_{2,2} &= \frac{\partial u_2}{\partial x_2} \\ \varepsilon_{33} = u_{3,3} &= \frac{\partial u_3}{\partial x_3} \\ \varepsilon_{12} = \frac{1}{2}(u_{1,2} + u_{2,1}) &= \frac{1}{2}\Big(\frac{\partial u_1}{\partial x_2} + \frac{\partial u_2}{\partial x_1}\Big) \\ \varepsilon_{23} = \frac{1}{2}(u_{2,3} + u_{3,2}) &= \frac{1}{2}\Big(\frac{\partial u_2}{\partial x_3} + \frac{\partial u_3}{\partial x_2}\Big) \\ \varepsilon_{31} = \frac{1}{2}(u_{3,1} + u_{1,3}) &= \frac{1}{2}\Big(\frac{\partial u_3}{\partial x_1} + \frac{\partial u_1}{\partial x_3}\Big) \end{aligned} \tag{2.6}$$

The stress vector

Consider a homogeneous body and an interior point $A(x_i)$. Cut through at that point with a plane with exterior normal $\mathbf{n}$. The stress vector at A for direction $\mathbf{n}$ can be defined as

$$\mathbf{t}_n = \lim_{\Delta A \to 0} \frac{\Delta \mathbf{t}}{\Delta A}$$

where ΔA is a differential area surrounding A on the cutting plane.

The stress tensor

Consider the equilibrium of an elemental tetrahedron at some point whose faces are normal to x_1, x_2, x_3 and $\mathbf{n}$ leads to the expression

$$t_i = \tau_{ij} n_j \tag{2.7}$$

where t_i is the component of t in the x_i direction, and n_j are the components of $\mathbf{n}$. The nine values τ_{ij} are the components of the stress tensor

$$\tau_{ij} = \begin{bmatrix} \tau_{11} & \tau_{12} & \tau_{13} \\ \tau_{21} & \tau_{22} & \tau_{23} \\ \tau_{31} & \tau_{32} & \tau_{33} \end{bmatrix} \tag{2.8}$$

Conservation of mass

Consider a material of volume V of surface S. The total mass is given by

$$m = \int_V \rho dV \tag{2.9}$$

As a material volume contains the same material at any instance, the total mass of the material in a material volume is constant:

$$\frac{d}{dt} \int_V \rho dV = 0 \tag{2.10}$$

Taking the derivative inside the integral returns

$$\int_V \frac{d\rho}{dt} dV = \int_V \Big[\frac{\partial \rho}{\partial t} + \frac{\partial}{\partial x_i} (\rho v_i) \Big] dV = 0 \tag{2.11}$$

For arbitrary V,

$$\frac{\partial \rho}{\partial t} + \rho v_{i,i} = 0 \tag{2.12}$$

Conservation of momentum

Consider the volume V of surface S. Associated with every point of V will be a acceleration a_i (acceleration field $\mathbf{a} = \ddot{u}$), while acting on the body will be surface traditions t_i and body forces h_i. According to the Newton's second law of motion, the force acting on a particle is equal to the rate of change of linear momentum:

$$F = \frac{d}{dt}(m\mathbf{v}) \tag{2.13}$$

The equation of conservation of momentum for a material is obtained by by postulating that the rate of change of linear momentum of the material contained in a material volume is equal to the total force acting on the material volume:

$$\int_S t_i dS + \int_V h_i \rho dV = \int_V \rho a_i dV \tag{2.14}$$

where ρ is the body density. Substitute $t_i = \tau_{ij} n_j$ in the surface integral:

$$\int_S \tau_{ij} n_j dS + \int_V h_i \rho dV = \int_V \rho a_i dV \tag{2.15}$$

To transform the surface integral to a volume integral we can use Gauss' divergence theorem. For any vector field $\mathbf{v}$:

$$\int_S \mathbf{a.n} dS = \int_V \mathbf{div.a} dV \tag{2.16}$$

or in component form

$$\int_S a_j n_j dS = \int_V \frac{\partial a_j}{\partial x_j} dV \tag{2.17}$$

Consequently the equilibrium integral can be reduced to

$$\int_V [\tau_{ij,j} + h_i - \rho a_i] dV = 0 \tag{2.18}$$

for an arbitrary volume, we must have

$$\tau_{ij,j} + h_i - \rho a_i = 0 \tag{2.19}$$

If we ignore the body force, the equilibrium equation becomes

$$\rho \ddot{u}_i = \tau_{ij,j} \tag{2.20}$$

Conservation of moment of momentum

This principle holds that the time rate change of moment of momentum is equal to the sum of the moments on the body.

$$\frac{d}{dt}\int_V \mathbf{r} \times \mathbf{v}\rho dV = \int_S \mathbf{r} \times \mathbf{t} dS + \int_V \mathbf{r} \times \mathbf{h}\rho dV \tag{2.21}$$

In tensor form

$$\int_V e_{ijk}\ddot{u}_k x_j \rho dV = \int_S e_{ijk} t_k x_j dS + \int_V e_{ijk} h_k x_j \rho dV \tag{2.22}$$

In differential form, applying Gauss's theorem returns

$$\int_S e_{ijk} t_k x_j dS = \int_S e_{ijk} x_j (\tau_{lk} n_l) dS = \int_V e_{ijk} x_j \tau_{lk,l} dV \tag{2.23}$$

Carrying out the differentiation gives

$$\int_S e_{ijk} t_k x_j dS = \int_V (e_{ijk}\tau_{jk} + e_{ijk} x_j \tau_{lk,l}) dV \tag{2.24}$$

Inserting (2.24) in (2.22), and using the results of conservation of momentum, gives

$$\int_V (e_{ijk}\tau_{jk}) dV = 0 \tag{2.25}$$

or

$$e_{ijk}\tau_{jk} = 0 \tag{2.26}$$

This returns to

$$\tau_{ij} = \tau_{ji} \qquad i \neq j \tag{2.27}$$

Equation (2.27) implies that the stress tensor is symmetric.

Constitutive equations

Constitutive equation provides the relation between states of deformation with states of traction. From the assumption of a direct functional relationship between stress and strain of the form

$$\tau_{ij} = \tau_{ij}(\varepsilon_{ij}) \tag{2.28}$$

Consider zero initial stress, expanding $\tau_{ij} = \tau_{ij}(\varepsilon_{ij})$ in a power series returns (discarding the constant term and higher order terms)

$$\tau_{ij} = C_{ijkl}\varepsilon_{kl} \tag{2.29}$$

Here, C_{ijkl} is the fourth order ($3 \times 3 \times 3 \times 3 = 81$ independent components) stiffness tensor responsible for the material properties (directional dependency of velocity). Symmetrical characteristics of stress and strain reduces the number to 36 (discussed in next chapter) and can be written with the following notation as:

$$\mathbb{C} = \begin{bmatrix} C_{1111} & C_{1122} & C_{1133} & C_{1123} & C_{1113} & C_{1112} \\ C_{2211} & C_{2222} & C_{2233} & C_{2223} & C_{2213} & C_{2212} \\ C_{3311} & C_{3322} & C_{3333} & C_{3323} & C_{3313} & C_{3312} \\ C_{2311} & C_{2322} & C_{2333} & C_{2323} & C_{2313} & C_{2312} \\ C_{1311} & C_{1322} & C_{1333} & C_{1323} & C_{1313} & C_{1312} \\ C_{1211} & C_{1222} & C_{1233} & C_{1223} & C_{1213} & C_{1212} \end{bmatrix}$$

The medium is elastically homogeneous if the components of C_{ijkl} are constants. Applying of Voigt notation (replacement of the four-subscript notation

with two-subscript form as: $11 \rightarrow 1$; $22 \rightarrow 2$; $33 \rightarrow 3$; $23,32 \rightarrow 4$; $31,13 \rightarrow 5$; $21,12 \rightarrow 6$) into the above equation leaves a more simpler form of $\mathbb{C}$ as:

$$\mathbb{C} = \begin{bmatrix} C_{11} & C_{12} & C_{13} & C_{14} & C_{15} & C_{16} \\ C_{21} & C_{22} & C_{23} & C_{24} & C_{25} & C_{26} \\ C_{31} & C_{32} & C_{33} & C_{34} & C_{35} & C_{36} \\ C_{41} & C_{42} & C_{43} & C_{44} & C_{45} & C_{46} \\ C_{51} & C_{52} & C_{53} & C_{54} & C_{55} & C_{56} \\ C_{61} & C_{62} & C_{63} & C_{64} & C_{65} & C_{66} \end{bmatrix}$$

The material is *isotropic* when there are no preferred directions in the material, and the elastic constants must be the same whatever the orientation of the Cartesian coordinate system in which the components of the stress tensor (τ_{ij}) and strain tensor (ε_{ij}) are evaluated. For such material, the stiffness matrix contains only 2 independent component and hence can be expressed as

$$C_{ISO} = \begin{bmatrix} C_{11} & C_{12} & C_{12} & 0 & 0 & 0 \\ & C_{11} & C_{12} & 0 & 0 & 0 \\ & & C_{11} & 0 & 0 & 0 \\ & & & \frac{C_{11}-C_{12}}{2} & 0 & 0 \\ & & & & \frac{C_{11}-C_{12}}{2} & 0 \\ & & \text{symmetric} & & & \frac{C_{11}-C_{12}}{2} \end{bmatrix} \tag{2.30}$$

Introducing *Lamé*'s parameters as

$$\begin{aligned} \lambda &= C_{12} \\ \mu &= \frac{1}{2}(C_{11} - C_{12}) \end{aligned} \tag{2.31}$$

Where λ is the combination of Young's modulus E, the bulk modulus K, and Poisson's ratio ν, μ describes the rigidity of the medium. Using this parameters, (2.30) can be shown as

$$C_{LAME} = \begin{bmatrix} \lambda+2\mu & \lambda & \lambda & 0 & 0 & 0 \\ & \lambda+2\mu & \lambda & 0 & 0 & 0 \\ & & \lambda+2\mu & 0 & 0 & 0 \\ & & & \mu & 0 & 0 \\ & & & & \mu & 0 \\ & \text{symmetric} & & & & \mu \end{bmatrix} \tag{2.32}$$

By using the *Lamé*'s constants, C_{ijkl} can be expressed as

$$C_{ijkl} = \lambda\delta_{ij}\delta_{kl} + \mu(\delta_{ik}\delta_{jl} + \delta_{il}\delta_{jk}) \tag{2.33}$$

Substituting (2.33) in (2.29) resulting as

$$\tau_{ij} = \lambda\varepsilon_{kk}\delta_{ij} + 2\mu\varepsilon_{ij} \tag{2.34}$$

where δ_{ij} is the *Kronecker delta*, defined as

$$\delta_{ij} = \begin{cases} 1 & \text{if } i = j \\ 0 & \text{if } i \neq j \end{cases}$$

Equation (2.34) can be resolved as following:

$$\begin{aligned} \tau_{11} &= \lambda\Big(\frac{\partial u_1}{\partial x_1} + \frac{\partial u_2}{\partial x_2} + \frac{\partial u_3}{\partial x_3}\Big) + 2\mu\frac{\partial u_1}{\partial x_1} \\ \tau_{22} &= \lambda\Big(\frac{\partial u_1}{\partial x_1} + \frac{\partial u_2}{\partial x_2} + \frac{\partial u_3}{\partial x_3}\Big) + 2\mu\frac{\partial u_2}{\partial x_2} \\ \tau_{33} &= \lambda\Big(\frac{\partial u_1}{\partial x_1} + \frac{\partial u_2}{\partial x_2} + \frac{\partial u_3}{\partial x_3}\Big) + 2\mu\frac{\partial u_3}{\partial x_3} \\ \tau_{12} &= \tau_{21} = \mu\Big(\frac{\partial u_1}{\partial x_2} + \frac{\partial u_2}{\partial x_1}\Big) \\ \tau_{23} &= \tau_{32} = \mu\Big(\frac{\partial u_2}{\partial x_3} + \frac{\partial u_3}{\partial x_2}\Big) \\ \tau_{13} &= \tau_{31} = \mu\Big(\frac{\partial u_3}{\partial x_1} + \frac{\partial u_1}{\partial x_3}\Big) \end{aligned} \tag{2.35}$$

If the strain-displacement relations are substituted into Hooke's law, and the expressions for the stresses are subsequently substituted in the stress-equations of motion, we obtain the displacement equations of motion.

$$(\lambda + \mu)u_{j,ji} + \mu u_{i,jj} + \rho h_i = \rho \ddot{u}_i \tag{2.36}$$

In the absence of body force

$$(\lambda + \mu)u_{j,ji} + \mu u_{i,jj} = \rho \ddot{u}_i \tag{2.37}$$

The vector equivalent notation of the displacement-equation of motion (2.37) is:

$$(\lambda + \mu)\nabla\nabla.\mathbf{u} + \mu\nabla^2\mathbf{u} = \rho\ddot{\mathbf{u}} \tag{2.38}$$

This system of equations represents three equation, as

$$\begin{aligned}
(\lambda + \mu)\Big(\frac{\partial^2 u_1}{\partial x_1^2} + \frac{\partial^2 u_2}{\partial x_1 \partial x_2} + \frac{\partial^2 u_3}{\partial x_1 \partial x_3}\Big) + \mu\nabla^2 u_1 &= \rho\frac{\partial^2 u_1}{\partial t^2} \\
(\lambda + \mu)\Big(\frac{\partial^2 u_1}{\partial x_2 \partial x_1} + \frac{\partial^2 u_2}{\partial x_2^2} + \frac{\partial^2 u_3}{\partial x_2 \partial x_3}\Big) + \mu\nabla^2 u_2 &= \rho\frac{\partial^2 u_2}{\partial t^2} \\
(\lambda + \mu)\Big(\frac{\partial^2 u_1}{\partial x_3 \partial x_1} + \frac{\partial^2 u_2}{\partial x_3 \partial x_2} + \frac{\partial^2 u_3}{\partial x_3^2}\Big) + \mu\nabla^2 u_3 &= \rho\frac{\partial^2 u_3}{\partial t^2}
\end{aligned}$$

Equation (2.37) can be easily uncoupled by eliminating two of the three displacement components which results in fourth order partial differential equations. A convenient way to express the elements of the displacement vector regarding derivative of the potentials as the potentials satisfy uncoupled wave equations.

Helmholtz decomposition

Helmholtz decomposition states that the displacement field of a material can be expressed as the sum of the gradient of a scalar potential ϕ and the curl of a vector potential Ψ, as

$$\mathbf{u} = \nabla\phi + \nabla \times \Psi \tag{2.39}$$

Substitution of the displacement representation (2.39) into (2.38) yields

$$(\lambda+\mu)\nabla\nabla.[\nabla\phi+\nabla\times\Psi]+\mu\nabla^2[\nabla\phi+\nabla\times\Psi]=\rho\frac{\partial^2}{\partial t^2}[\nabla\phi+\nabla\times\Psi]$$

Since $\nabla.\nabla\phi=\nabla^2\phi$ and $\nabla.\nabla\times\Psi=0$, upon rearranging, we obtain

$$\nabla[(\lambda+2\mu)\nabla^2\phi-\rho\ddot{\phi}]+\nabla\times[\mu\nabla^2\Psi-\rho\ddot{\Psi}]=0 \tag{2.40}$$

Clearly, the displacement representation (2.39) satisfies the equation of motion if

$$\begin{aligned}\nabla^2\phi&=\frac{1}{\alpha^2}\ddot{\phi}\\ \nabla^2\Psi&=\frac{1}{\beta^2}\ddot{\Psi}\end{aligned} \tag{2.41}$$

where α and β are the longitudinal (dilatational) and transverse (distorsional) velocity of component

$$\begin{aligned}\alpha&=\sqrt{\frac{(\lambda+2\mu)}{\rho}}\\ \beta&=\sqrt{\frac{\mu}{\rho}}\end{aligned} \tag{2.42}$$

Equation (2.41) is uncoupled wave equation. Though the scalar potential ϕ and components of the vector potential Ψ are coupled through the boundary conditions, the use of the displacement decomposition simplifies the analysis. By selecting the particular appropriate solutions of (2.41) regarding arbitrary functions or integrals over arbitrary functions, a boundary-initial value problem can be solved.

It should be noted that (2.39) relates the three components of the displacement vector to four other functions: the scalar potential and the three components of the vector potential, as follows:

$$\begin{aligned}u_1&=\frac{\partial\phi}{\partial x_1}+\frac{\partial\psi_3}{\partial x_2}-\frac{\partial\psi_2}{\partial x_3}\\ u_2&=\frac{\partial\phi}{\partial x_2}-\frac{\partial\psi_3}{\partial x_1}+\frac{\partial\psi_1}{\partial x_3}\\ u_3&=\frac{\partial\phi}{\partial x_3}+\frac{\partial\psi_2}{\partial x_1}-\frac{\partial\psi_1}{\partial x_2}\end{aligned} \tag{2.43}$$

The components ψ_1, ψ_2, ψ_3 of the vector potential Ψ satisfy the equations

$$\begin{aligned}\nabla^2\psi_1 &= \frac{1}{\beta^2}\ddot{\psi}_1\\ \nabla^2\psi_2 &= \frac{1}{\beta^2}\ddot{\psi}_2\\ \nabla^2\psi_3 &= \frac{1}{\beta^2}\ddot{\psi}_3\end{aligned} \tag{2.44}$$

So, following (2.35), stresses can be written in terms of the displacement potentials as

$$\begin{aligned}\tau_{11} &= \lambda\nabla^2\phi + 2\mu\Big[\frac{\partial^2\phi}{\partial x_1^2} + \frac{\partial}{\partial x_1}\Big(\frac{\partial\psi_3}{\partial x_2} - \frac{\partial\psi_2}{\partial x_3}\Big)\Big]\\ \tau_{22} &= \lambda\nabla^2\phi + 2\mu\Big[\frac{\partial^2\phi}{\partial x_2^2} - \frac{\partial}{\partial x_2}\Big(\frac{\partial\psi_3}{\partial x_1} - \frac{\partial\psi_1}{\partial x_3}\Big)\Big]\\ \tau_{33} &= \lambda\nabla^2\phi + 2\mu\Big[\frac{\partial^2\phi}{\partial x_3^2} + \frac{\partial}{\partial x_3}\Big(\frac{\partial\psi_2}{\partial x_1} - \frac{\partial\psi_1}{\partial x_2}\Big)\Big]\\ \tau_{12} = \tau_{21} &= \mu\Big[2\frac{\partial^2\phi}{\partial x_1\partial x_2} + \frac{\partial}{\partial x_2}\Big(\frac{\partial\psi_3}{\partial x_2} - \frac{\partial\psi_2}{\partial x_3}\Big) - \frac{\partial}{\partial x_1}\Big(\frac{\partial\psi_3}{\partial x_1} - \frac{\partial\psi_1}{\partial x_3}\Big)\Big]\\ \tau_{23} = \tau_{32} &= \mu\Big[2\frac{\partial^2\phi}{\partial x_2\partial x_3} - \frac{\partial}{\partial x_3}\Big(\frac{\partial\psi_3}{\partial x_1} - \frac{\partial\psi_1}{\partial x_3}\Big) + \frac{\partial}{\partial x_2}\Big(\frac{\partial\psi_2}{\partial x_1} - \frac{\partial\psi_1}{\partial x_2}\Big)\Big]\\ \tau_{31} = \tau_{13} &= \mu\Big[2\frac{\partial^2\phi}{\partial x_1\partial x_3} + \frac{\partial}{\partial x_3}\Big(\frac{\partial\psi_3}{\partial x_2} - \frac{\partial\psi_2}{\partial x_3}\Big) + \frac{\partial}{\partial x_1}\Big(\frac{\partial\psi_2}{\partial x_1} - \frac{\partial\psi_1}{\partial x_2}\Big)\Big]\end{aligned}$$

2.2 STEADY-STATE TWO-DIMENSIONAL WAVE

Consider the elastic half-space depicted in Fig.2.3. The material is assumed

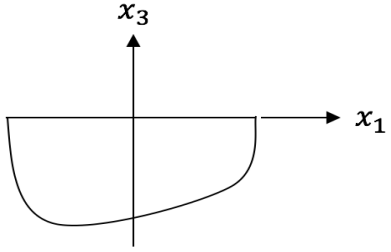

Fig. 2.3: An elastic half space

to be unbounded to the bottom of the infinite plane boundary. A Cartesian coordinate system is oriented with the negative x_3 direction pointing into the material and the $x_1 - x_2$ plane coincident with the perimeter of the half space. Assume that the motion of the material is described by the displacement field as:

$$\begin{aligned} u_1 &= u_1(x_1, x_3, t), \\ u_2 &= 0, \\ u_3 &= u_3(x_1, x_3, t) \end{aligned} \tag{2.45}$$

Thus the motion is two-dimensional: it is independent of the coordinate normal to the plane $(x_1 - x_3)$, and the component of the displacement normal to the plane is zero. This type of motion is called plane strain. Applying this condition in (2.43) gives,

$$\begin{aligned} u_1 &= \frac{\partial \phi}{\partial x_1} - \frac{\partial \psi_2}{\partial x_3}, \\ u_3 &= \frac{\partial \phi}{\partial x_3} + \frac{\partial \psi_2}{\partial x_1} \end{aligned} \tag{2.46}$$

Where $\phi = \phi(x_1, x_3, t)$ and $\psi_2 = \psi_2(x_1, x_3, t)$. The potentials ϕ and ψ_2 are governed by the following wave equations

$$\begin{aligned} \frac{\partial^2 \phi}{\partial t^2} &= \alpha^2 \Big(\frac{\partial^2 \phi}{\partial x_1^2} + \frac{\partial^2 \phi}{\partial x_3^2} \Big), \\ \frac{\partial^2 \psi_2}{\partial t^2} &= \beta^2 \Big(\frac{\partial^2 \psi_2}{\partial x_1^2} + \frac{\partial^2 \psi_2}{\partial x_3^2} \Big) \end{aligned} \tag{2.47}$$

Let us assume a solution of the equation of potential ϕ that is harmonic, or oscillatory function of time:

$$\phi = f(x_3) e^{i(k_1 x_1 - \omega t)} \tag{2.48}$$

Where the wave number is k_1, the frequency ω is prescribed and the arbitrary function $f(x_3)$ must be determined. Assume that the solution for the potential ϕ has the form of a steady state wave propagating in the positive

x_1 direction. Substituting this expression into (2.47) returns that the function $f(x_3)$ must satisfy the ordinary differential equation

$$\frac{d^2 f(x_3)}{dx_3^2} + \Big(\frac{\omega^2}{\alpha^2} - k_1^2\Big) f(x_3) = 0 \tag{2.49}$$

The solution of this equation result in solutions for ϕ that have very different characters depending on whether $\omega^2/\alpha^2 > k_1^2$ or $\omega^2/\alpha^2 < k_1^2$. Consider only the first case where the plane waves propagating in the $x_1 - x_3$ plane. It is convenient to use the complex exponential function to write the solution of (2.49):

$$f(x_3) = Ae^{ik_3 x_3} + Be^{-ik_3 x_3}$$

where A and B are constants and

$$k_3 = \sqrt{\frac{\omega^2}{\alpha^2} - k_1^2}$$

Substituting this form of the solution for $f(x_3)$ into (2.48), the solution becomes

$$\phi = Ae^{i(k_1 x_1 + k_3 x_3 - \omega t)} + Be^{i(k_1 x_1 - k_3 x_3 - \omega t)} \tag{2.50}$$

The first term of (2.50) describes a plane wave equation. At any time t the value of ϕ is constant on planes defined by the equation

$$k_1 x_1 + k_3 x_3 = \text{constant}$$

Consider two successive peaks of a plane wave having wavelength λ, propagating in $x_1 - x_3$ plane at an angle of θ to the horizontal direction with wave speed α. The wavelength is related to the wave number k by $\lambda = 2\pi/k$. Using Fig. (2.4), the wave number k_1 and k_3 can be written as:

$$k_1 = \frac{2\pi}{\lambda_1} = \frac{2\pi}{\lambda}\cos\theta = k\cos\theta,$$
$$k_3 = \frac{2\pi}{\lambda_3} = \frac{2\pi}{\lambda}\sin\theta = k\sin\theta$$

where the wave number $k = \omega/\alpha$. With this result, first part of (2.50) can be

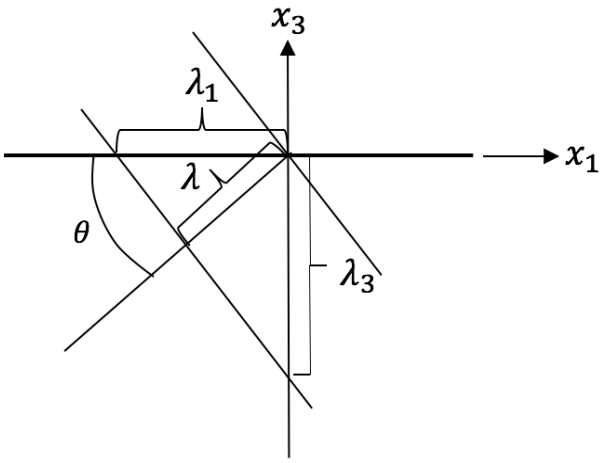

Fig. 2.4: Lines along two succeeding peaks of the plane wave

expressed in terms of the propagation direction θ as:

$$\phi = Ae^{i(kx_1\cos\theta + kx_3\sin\theta - \omega t)} \tag{2.51}$$

From (2.46), the components of the displacement field of the steady state compressional wave illustrated as

$$u_1 = \frac{\partial\phi}{\partial x_1} = ikA\cos\theta e^{i(kx_1\cos\theta + kx_3\sin\theta - \omega t)},$$
$$u_3 = \frac{\partial\phi}{\partial x_3} = ikA\sin\theta e^{i(kx_1\cos\theta + kx_3\sin\theta - \omega t)}$$

From these expressions, it is found that the displacements of the points of the material are parallel to the propagation direction of the compressional wave. Equation (2.51) is a convenient expression for a plane compressional wave with propagation direction θ relative to the x_1 axis.
An expression of solution for a plane shear wave with propagation direction θ with x_1 axis can be assumed in the same fashion for the potential ψ_2, as:

$$\psi_2 = Ce^{i(k_S x_1\cos\theta + k_S x_3\sin\theta - \omega t)} \tag{2.52}$$

where C is a constant and the wave number $k_S = \omega/\beta$. From (2.46), the components of the displacement field of the steady state compressional wave illustrated as

$$u_1 = -\frac{\partial \psi_2}{\partial x_3} = -ik_S C \sin\theta e^{i(k_S x_1 \cos\theta + k_S x_3 \sin\theta - \omega t)},$$
$$u_3 = \frac{\partial \psi_2}{\partial x_1} = ik_S C \cos\theta e^{i(k_S x_1 \cos\theta + k_S x_3 \sin\theta - \omega t)}$$

These expressions show the displacements of the points of the material are parallel to the propagation direction of the shear wave.

2.2.1 *Reflection of compressional wave*

Consider the elastic half space, and take the assumption that a plane compressional wave with known frequency and known complex amplitude propagates toward the free boundary of the half space shown in Fig.2.5. The

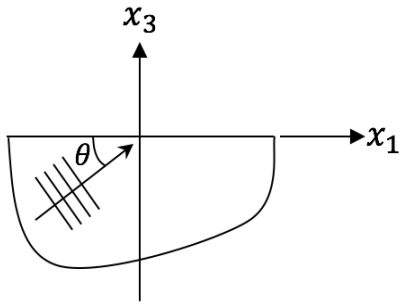

Fig. 2.5: Elastic half space with a plane compressional wave incident on the boundary

equation of such propagating waves can be expressed with a potential as:

$$\phi = Ie^{i(kx_1 \cos\theta + kx_3 \sin\theta - \omega t)} \tag{2.53}$$

where I is the complex amplitude an the wave number $k = \omega/\alpha$. The wave propagates in the positive x_1 and positive x_3 direction. The boundary of the geometry is stress free:

$$[\tau_{ij} n_i]_{x_3=0} = 0$$

The unit vector normal to the boundary has components $n_1 = 0, n_2 = 0, n_3 = 1$, so from this condition stress boundary conditions become

$$\begin{aligned} [\tau_{13}]_{x_3=0} &= 0, \\ [\tau_{23}]_{x_3=0} &= 0, \\ [\tau_{33}]_{x_3=0} &= 0 \end{aligned}$$

That is, the normal stress and the two components of shear stress on the boundary is zero. For the two dimensional motion consideration, the stress component τ_{23} is identically zero. The displacement field must satisfy the other two boundary condition, returns as:

$$\begin{aligned} [\tau_{13}]_{x_3=0} &= \Big[\mu\Big(\frac{\partial u_1}{\partial x_3} + \frac{\partial u_3}{\partial x_1}\Big)\Big]_{x_3=0} = 0, \\ [\tau_{33}]_{x_3=0} &= \Big[\lambda \frac{\partial u_1}{\partial x_1} + (\lambda + 2\mu)\frac{\partial u_3}{\partial x_3}\Big]_{x_3=0} = 0 \end{aligned} \tag{2.54}$$

The boundary conditions can be satisfied by taking the assumptions that the incident compressional wave causes a reflected compressional and a reflected shear wave, and therefore the compressional potential ϕ and the shear potential ψ_2 becomes:

$$\begin{aligned} \phi &= Ie^{i(kx_1\cos\theta + kx_3\sin\theta - \omega t)} + Pe^{i(kx_1\cos\theta_P - kx_3\sin\theta_P - \omega t)}, \\ \psi_2 &= Se^{i(k_S x_1\cos\theta_S - k_S x_3\sin\theta_S - \omega t)} \end{aligned} \tag{2.55}$$

where P and S are the complex amplitude of the reflected compressional and shear waves. The propagation direction is θ_P and θ_S respectively. The wave number of reflected shear wave k_S can be defined by $k_S = \omega/\beta$. Reflected waves propagate in the positive x_1 and positive x_3 direction. Substituting

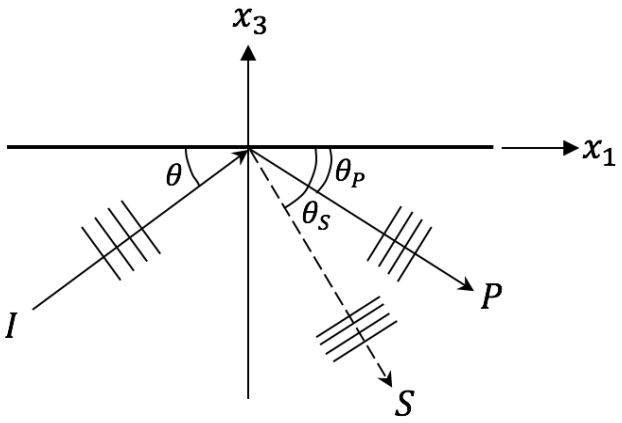

Fig. 2.6: The reflected compressional and shear wave

(2.55) into (2.46), the displacement field can be written as

$$\begin{aligned}
u_1 &= (u_1)_I + (u_1)_P + (u_1)_S \\
&= iIk\cos\theta e^{i(kx_1\cos\theta + kx_3\sin\theta - \omega t)} + iPk\cos\theta_P e^{i(kx_1\cos\theta_P - kx_3\sin\theta_P - \omega t)} \\
&\quad + iSk_S\sin\theta_S e^{i(k_S x_1\cos\theta_S - k_S x_3\sin\theta_S - \omega t)}, \\
u_3 &= (u_3)_I + (u_3)_P + (u_3)_S \\
&= iIk\sin\theta e^{i(kx_1\cos\theta + kx_3\sin\theta - \omega t)} - iPk\sin\theta_P e^{i(kx_1\cos\theta_P - kx_3\sin\theta_P - \omega t)} \\
&\quad + iSk_S\cos\theta_S e^{i(k_S x_1\cos\theta_S - k_S x_3\sin\theta_S - \omega t)}
\end{aligned} \tag{2.56}$$

where the subscripts I, P, and S refer to the incident, compressional, and shear waves.

2.2.2 *Reflection of shear wave*

Assume that a plane shear wave with known frequency and known complex amplitude is incident on the free boundary of an elastic half-space at an angle of θ with x_1 axis. For a particular range of value of the propagation direction, assuming that, the incident wave causes a reflected shear wave with propagation direction θ_S and a reflected compressional wave with propagation direction θ_P, as shown in Fig.2.7. The compressional and the shear potential

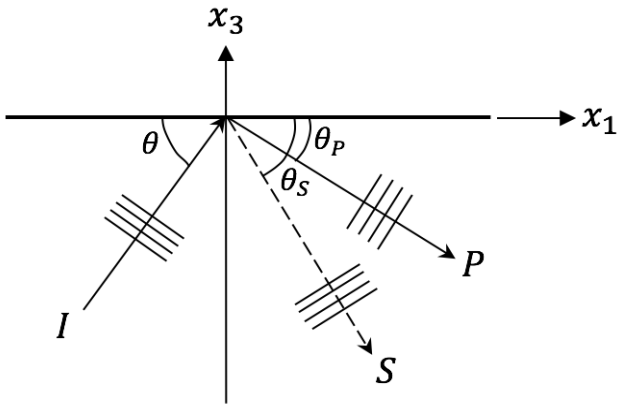

Fig. 2.7: Elastic half space with a plane shear wave incident on the boundary

can be written as:

$$\begin{aligned}\phi &= Pe^{i(k_P x_1 \cos\theta_P - k_P x_3 \sin\theta_P - \omega t)},\\ \psi_2 &= Ie^{i(kx_1\cos\theta + kx_3\sin\theta - \omega t)} + Se^{i(kx_1\cos\theta_S - kx_3\sin\theta_S - \omega t)}\end{aligned} \tag{2.57}$$

where I, P, and S are the complex amplitude of the incident, reflected compressional and shear waves. The wave numbers $k = \omega/\beta$ and $k_P = \omega/\alpha$. From these potentials, displacement field can be obtained as

$$\begin{aligned}u_1 &= (u_1)_P + (u_1)_I + (u_1)_S\\ &= iPk_P\cos\theta_P e^{i(k_P x_1\cos\theta_P - k_P x_3\sin\theta_P - \omega t)} - iIk\sin\theta e^{i(kx_1\cos\theta + kx_3\sin\theta - \omega t)}\\ &\quad + iSk\sin\theta_S e^{i(kx_1\cos\theta_S - kx_3\sin\theta_S - \omega t)},\\ u_3 &= (u_3)_P + (u_3)_I + (u_3)_S\\ &= -iPk_P\sin\theta_P e^{i(k_P x_1\cos\theta_P - k_P x_3\sin\theta_P - \omega t)} + iIk\cos\theta e^{i(kx_1\cos\theta + kx_3\sin\theta - \omega t)}\\ &\quad + iSk\cos\theta_S e^{i(kx_1\cos\theta_S - kx_3\sin\theta_S - \omega t)}\end{aligned} \tag{2.58}$$

where the subscripts I, P, and S refer to the incident, compressional, and shear waves.

Consider the propagation of two-dimensional (2D) steady state waves along a plate of elastic material with stress-free surfaces (Fig.2.8). The displacement

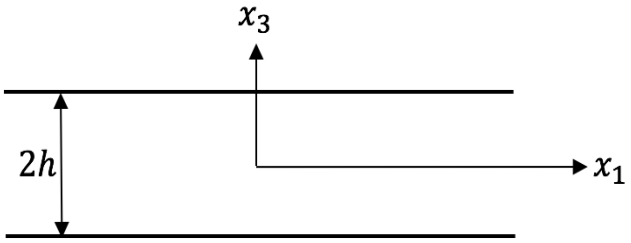

Fig. 2.8: A plate of elastic material with free surfaces

field of two dimensional motion in terms of scalar potential ϕ and ψ_2 is quite similar stated in (2.45) and (2.46). Assume solutions for ϕ and ψ_2 that describe a steady state wave propagating along a plate:

$$\begin{aligned} \phi &= f(x_3)e^{i(k_1x_1-\omega t)}, \\ \psi_2 &= g(x_3)e^{i(k_1x_1-\omega t)} \end{aligned} \tag{2.59}$$

Substituting these equations into (2.47), the functions $f(x_3)$ and $g(x_3)$ can be written as follows

$$\begin{aligned} f(x_3) &= A\sin k_P x_3 + B\cos k_P x_3, \\ g(x_3) &= C\sin k_S x_3 + D\cos k_S x_3 \end{aligned} \tag{2.60}$$

where

$$\begin{aligned} k_P &= \sqrt{\frac{\omega^2}{\alpha^2} - k_1^2}, \\ k_S &= \sqrt{\frac{\omega^2}{\beta^2} - k_1^2} \end{aligned}$$

The resulting solutions for ϕ and ψ_2 are

$$\begin{aligned}\phi &= (A\sin k_P x_3 + B\cos k_P x_3)e^{i(k_1 x_1 - \omega t)},\\ \psi_2 &= (C\sin k_S x_3 + D\cos k_S x_3)e^{i(k_1 x_1 - \omega t)}\end{aligned} \tag{2.61}$$

where A, B, C, D are four constants determined by the boundary conditions. α and β are the velocities of compressional and shear modes, respectively, defined in (2.42). It can be seen that Lamb waves are the superposition of compressional and shear waves. An infinite number of modes exist simultaneously, superimposing on each other between the upper and lower surfaces of the plate, finally leading to well-behaved guided waves (Fig.2.9).

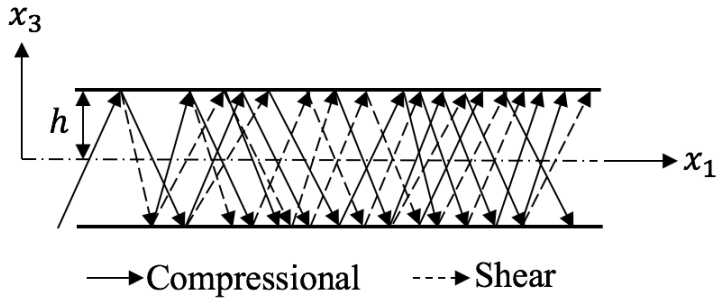

Fig. 2.9: Wave propagation in a thin plate as a result of superimposing of compressional and shear waves

Let use the solutions (2.61) to determine the displacement components:

$$\begin{aligned}u_1 &= [ik_1(A\sin k_P x_3 + B\cos k_P x_3) - k_S(C\cos k_S x_3 - D\sin k_S x_3)]e^{i(k_1 x_1 - \omega t)},\\ u_3 &= [k_P(A\cos k_P x_3 - B\sin k_P x_3) + ik_1(C\sin k_S x_3 + D\cos k_S x_3)]e^{i(k_1 x_1 - \omega t)}\end{aligned} \tag{2.62}$$

The term containing A and D describe the antisymmetric distributions of u_1 with respect to the centerline of the plate. On the other hand, the term containing B and C describe the symmetric distributions (Fig.2.10). In the same way, distribution of u_3 is also follow the symmetric and antisymmetric pattern with respect to the mid plane of the plate (Fig.2.11). Consider the

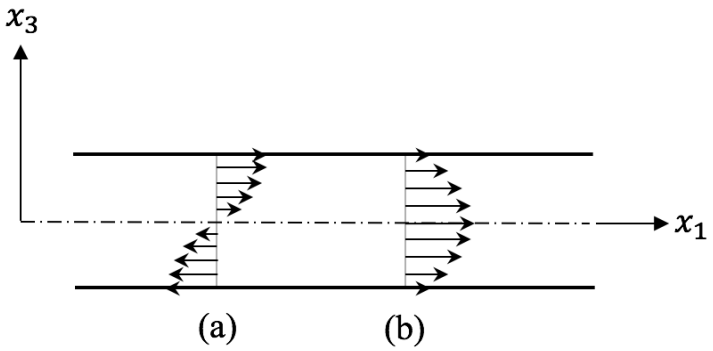

Fig. 2.10: (a) Antisymmetric and (b) symmetric distributions of u_1

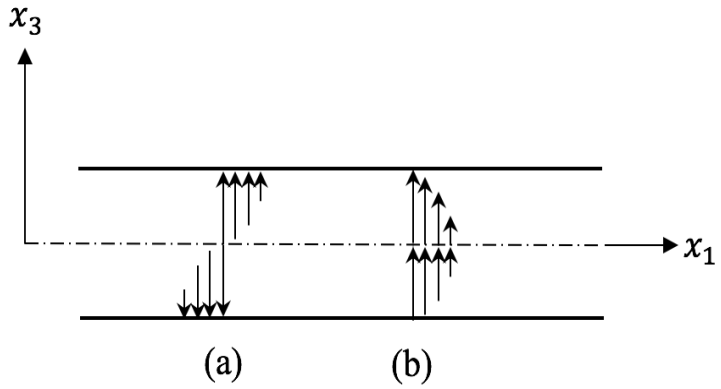

Fig. 2.11: (a) Symmetric and (b) Antisymmetric distributions of u_3

part of the solutions for ϕ and ψ_2 that result in a symmetric distribution of u_1:

$$\begin{aligned} \phi &= B\cos k_P x_3 e^{i(k_1 x_1 - \omega t)}, \\ \psi_2 &= C\sin k_S x_3 e^{i(k_1 x_1 - \omega t)} \end{aligned} \tag{2.63}$$

The resulting expressions for u_1 and u_3 are

$$\begin{aligned} u_1 &= [ik_1 B\cos k_P x_3 - k_S C\cos k_S x_3]e^{i(k_1 x_1 - \omega t)}, \\ u_3 &= [-k_P B\sin k_P x_3 + ik_1 C\sin k_S x_3]e^{i(k_1 x_1 - \omega t)} \end{aligned} \tag{2.64}$$

the boundary conditions at the free surfaces of the plate are

$$\begin{aligned} [\tau_{13}]_{x_3=\pm h} &= \Big[\mu\Big(\frac{\partial u_1}{\partial x_3} + \frac{\partial u_3}{\partial x_1}\Big)\Big]_{x_3=\pm h} = 0, \\ [\tau_{33}]_{x_3=\pm h} &= \Big[\lambda\frac{\partial u_1}{\partial x_1} + (\lambda+2\mu)\frac{\partial u_3}{\partial x_3}\Big]_{x_3=\pm h} = 0 \end{aligned} \tag{2.65}$$

With the aid of (2.64), the first condition of (2.65) can be expressed as

$$\Big[\mu\Big\{\frac{\partial}{\partial x_3}\Big((ik_1B\cos k_Px_3 - k_SC\cos k_Sx_3)e^{i(k_1x_1-\omega t)}\Big) + \frac{\partial}{\partial x_1}\Big((-k_PB\sin k_Px_3 + ik_1C\sin k_Sx_3)e^{i(k_1x_1-\omega t)}\Big)\Big\}\Big]_{x_3=\pm h} = 0$$

$$\Big[\mu\Big\{(-ik_1k_PB\sin k_px_3 + k_S^2C\sin k_sx_3)e^{i(k_1x_1-\omega t)} + (-k_PB\sin k_Px_3 + ik_1C\sin k_sx_3)ik_1e^{i(k_1x_1-\omega t)}\Big\}\Big]_{x_3=\pm h} = 0$$

which further reduces to

$$\begin{aligned} -2ik_1k_PB\sin k_Ph + (k_S^2 - k_1^2)C\sin k_Sh = 0 \\ -2ik_1k_PB\sin k_Ph + (\omega^2/\beta^2 - 2k_1^2)C\sin k_Sh = 0 \end{aligned} \tag{2.66}$$

Similarly, from (2.64) and the second condition of (2.65),

$$\Big[\lambda\Big\{\frac{\partial}{\partial x_1}\Big((ik_1B\cos k_Px_3 - k_SC\cos k_Sx_3)e^{i(k_1x_1-\omega t)}\Big)\Big\} + (\lambda+2\mu)\Big\{\frac{\partial}{\partial x_3}\Big((-k_PB\sin k_Px_3 + ik_1C\sin k_Sx_3)e^{i(k_1x_1-\omega t)}\Big)\Big\}\Big]_{x_3=\pm h} = 0$$

$$\Big[\lambda\Big\{(ik_1B\cos k_Px_3 - k_SC\cos k_Sx_3)ik_1e^{i(k_1x_1-\omega t)}\Big\} + (\lambda+2\mu)\Big\{(-k_P^2B\cos k_Px_3 + ik_1k_SC\cos k_Sx_3)e^{i(k_1x_1-\omega t)}\Big\}\Big]_{x_3=\pm h} = 0$$

inserting the condition further reduces the equation as

$$\begin{aligned} \{-\lambda k_1^2 - (\lambda+2\mu)k_P^2\}B\cos k_Ph + 2\mu ik_1k_SC\cos k_Sh = 0 \\ \{2\mu k_1^2 - (\lambda+2\mu)\omega^2/\alpha^2\}B\cos k_Ph + 2\mu ik_1k_SC\cos k_Sh = 0 \end{aligned} \tag{2.67}$$

Equation (2.66) and (2.67) leaves two homogeneous equations in terms of B and C:

$$\begin{bmatrix} \{2\mu k_1^2 - (\lambda+2\mu)\omega^2/\alpha^2\}\cos k_Ph & 2i\mu k_1k_S\cos k_Sh \\ -2ik_1k_P\sin k_Ph & (\omega^2/\beta^2 - 2k_1^2)\sin k_Sh \end{bmatrix}\begin{bmatrix} B \\ C \end{bmatrix} = 0 \tag{2.68}$$

This eigenvalue problem has a nontrivial solution for B and C only if the determinant of the coefficients is equal to zero.

$$\{2\mu k_1^2 - (\lambda + 2\mu)\omega^2/\alpha^2\}(\omega^2/\beta^2 - 2k_1^2)\cos k_P h \sin k_S h - 4\mu k_1^2 k_P k_S \cos k_S h \sin k_P h = 0 \quad (2.69)$$

The frequency equation becomes

$$\frac{\tan k_S h}{\tan k_P h} = -\frac{4k_P k_S k_1^2}{(k_1^2 - k_S^2)^2} \quad (2.70)$$

This is the Rayleigh-Lamb frequency equation for the propagation of the symmetric waves in a plate.
Now consider the part of the solutions for ϕ and ψ_2 from (2.61) that result in an antisymmetric distribution:

$$\begin{aligned} \phi &= A \sin k_P x_3 e^{i(k_1 x_1 - \omega t)}, \\ \psi_2 &= D \cos k_S x_3 e^{i(k_1 x_1 - \omega t)} \end{aligned} \quad (2.71)$$

Following (2.62), inserting the antisymmetric condition leaves the expression for u_1 and u_3 as:

$$\begin{aligned} u_1 &= [ik_1 A \sin k_P x_3 + k_S D \sin k_S x_3] e^{i(k_1 x_1 - \omega t)}, \\ u_3 &= [k_P A \cos k_P x_3 + ik_1 D \cos k_S x_3] e^{i(k_1 x_1 - \omega t)} \end{aligned} \quad (2.72)$$

Inserting the equation (2.72) in stress free boundary condition (2.65) gives two homogeneous equations in terms of A and D;

$$\begin{bmatrix} 2ik_1 k_P \cos k_P h & (\omega^2/\beta^2 - 2k_1^2)\cos k_S h \\ \{2\mu k_1^2 - (\lambda + 2\mu)\omega^2/\alpha^2\}\sin k_P h & -2i\mu k_1 k_S \sin k_S h \end{bmatrix} \begin{bmatrix} A \\ D \end{bmatrix} = 0 \quad (2.73)$$

Further reduces of this equation turn out as a frequency equation:

$$\frac{\tan k_S h}{\tan k_P h} = -\frac{(k_1^2 - k_S^2)^2}{4k_P k_S k_1^2} \quad (2.74)$$

This gives the Rayleigh-Lamb equation for antisymmetric waves in a plate. We may combine the frequency equations for symmetric and antisymmetric waves into a single equation given by

$$\frac{\tan k_S h}{\tan k_P h} + \left[\frac{4k_P k_S k_1^2}{(k_1^2 - k_S^2)^2}\right]^{\pm 1} = 0 \tag{2.75}$$

where $+1$ is for symmetric and -1 is for antisymmetric.
The frequency equations have an infinite number of roots whereas each root yields a propagation mode that satisfies the boundary conditions at the free surfaces of the plate. The symbols S_i and A_i $(i = 0, 1 \cdots)$ stand for the symmetric and antisymmetric Lamb modes, respectively, with the subscript being the order and in particular S_0 and A_0 being the lowest-order (fundamental order) symmetric and antisymmetric lamb modes, respectively.
The schematics of particle motion in the symmetric and antisymmetric Lamb wave modes are plotted in Fig.2.12, indicating the displacement direction of

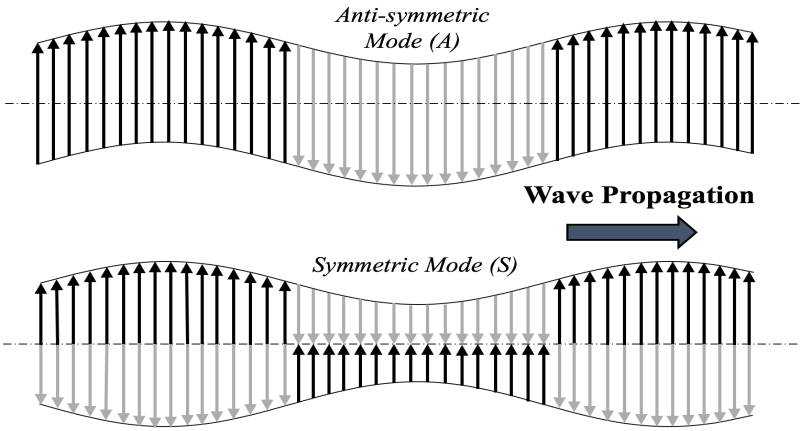

Fig. 2.12: Lamb wave

particles and resulting motion. S_i modes predominantly have radial in-plane displacement direction of particles, and in contrast, A_i modes mostly have out-of-plane displacement. Thats because a symmetric wave mode is often described as compressional, showing thickness bulging and contracting; and an antisymmetric mode is known as flexural, presenting contact thickness flexing.
The propagation of Lamb waves can be characterized by *phase* (v_p) and *group*

(v_g) velocity. The phase velocity is referred to as the propagation speed of the wave phase of a particular frequency contained in the overall wave signals, which can be linked with the wavelength. The group velocity is referred to as the velocity with which the overall shape of the amplitudes of the wave propagates through space (the velocity of wave energy transportation).

2.4 VELOCITY DISPERSION OF LAMB WAVES

As with most guided waves, Lamb waves are dispersive; that is, their velocity of propagation depends on wave frequency (or wavelength), plate thickness and as well as on the elastic constants and density of the material. This phenomenon is called dispersion. The graphic depiction of solutions of the dispersion equations is called dispersion curves. The Lamb wave dispersion equation (2.75) does not generally offer analytical solutions, rather in most cases can only be solved using graphic or numerical methods. Steps are given below, followed to numerically solve the equation to achieve the dispersion curves numerically [76].

1. an initial frequency-thickness product $(f.h)_0$ is chosen;
2. made an initial estimate of the velocity $(v_p)_0$;
3. evaluated the signs of each of the left-hand sides of equation (2.75) by assuming they are not equal to zero;
4. chosen another velocity $(v_p)_1 > (v_p)_0$ and re-evaluated the signs of equation (2.75);
5. steps 3 and 4 are repeated carefully until the sign changes. A root must exist in the interval where a sign change occurs, as the functions involved are continuous. Assumed that it occurred between velocities $(v_p)_n$ and $(v_p)_{n+1}$;
6. used bisection method to locate the root precisely in the interval $(v_p)_n < (v_p) < (v_p)_{n+1}$;
7. continued the process at the current $(f.h)$ for other roots; and
8. chosen another $(f.h)$ and repeated the steps through 2 to 7.

As an example, for the mechanical properties of steel plate ($E = 205\,\text{GPa}, \nu = 0.27$, and $\rho = 7800\,\text{kg/m}^3$), the dispersion curves of various Lamb wave in accordance with following above steps are depicted in Fig.2.13. Such

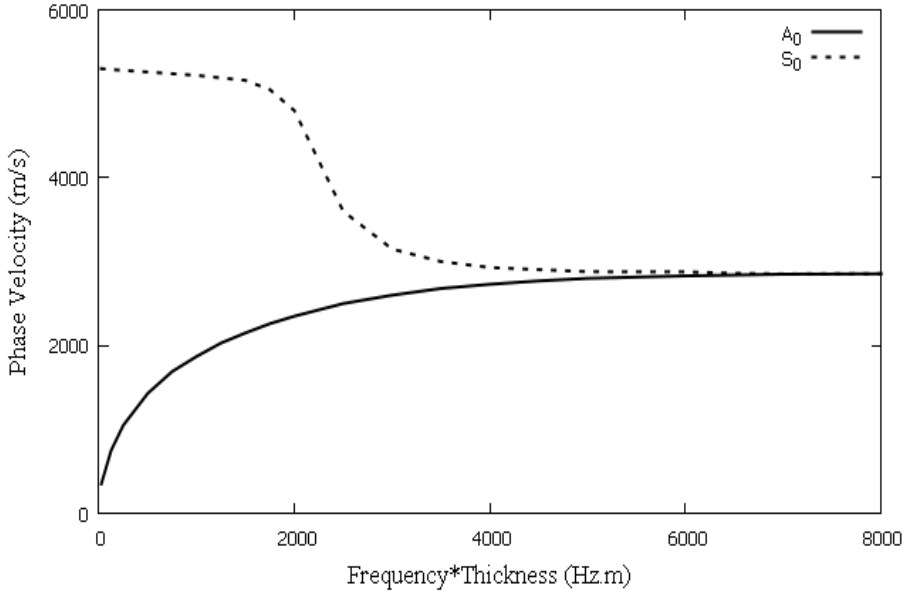

Fig. 2.13: Fundamental order Lamb wave dispersion curves in a steel plate of 1.00 mm in thickness

curves are used to describe and predict the relationship between frequency, phase/group velocity, and thickness. The fundamental mode symmetrical and anti-symmetrical modes deserve special attention as they are the only modes exist over the entire frequency spectrum. Moreover, in practical situations, they carry more energy than higher-order modes. Fig. 2.13 illustrated that the antisymmetric mode is high dispersive in the low-frequency regime.

2.5 LAMB WAVES IN MULTIPLE LAYER

Elastic waves in composite laminates is become also a matter of great interest nowadays as its applications in various engineering sectors increased exponentially. Considering a plate comprised of homogeneous layers, the propagation of Lamb waves inside the plate includes not only scattering at the up-

per and lower boundary but reflection and refraction between layers might occur. Expanding (2.38) to an N-layered laminate, the displacement field $\mathbf{u}$, within each layers much satisfy the Navier's displacement equations[77], and for n^{th} layer

$$\mu^n \nabla^2 \mathbf{u}^n + (\lambda^n + \mu^n)\nabla(\nabla.\mathbf{u}^n) = \rho^n \frac{\partial^2 \mathbf{u}^n}{\partial t^2} \qquad (n = 1, 2, \cdot N) \tag{2.76}$$

Variables in the above equation are distinguished by the superscript for each individual layer. Equation (2.39) is the most efficient way to decompose the displacement fields, and further to obtain the displacement, strain and stress in each individual layer, as detailed elsewhere [77][20].

3

ANISOTROPIC WAVE PROPAGATION

The wave propagation in anisotropic media is different to the simplest model, the isotropic case. The most significant difference between this two class holds the directional dependent velocity of wave propagation. Furthermore, unlike the isotropic case, three modes are available in wave propagation: L (longitudinal/compressional), SV (shear-vertical) and SH (shear-horizontal) waves (Fig.3.1). The particle vibration of such modes is neither parallel nor

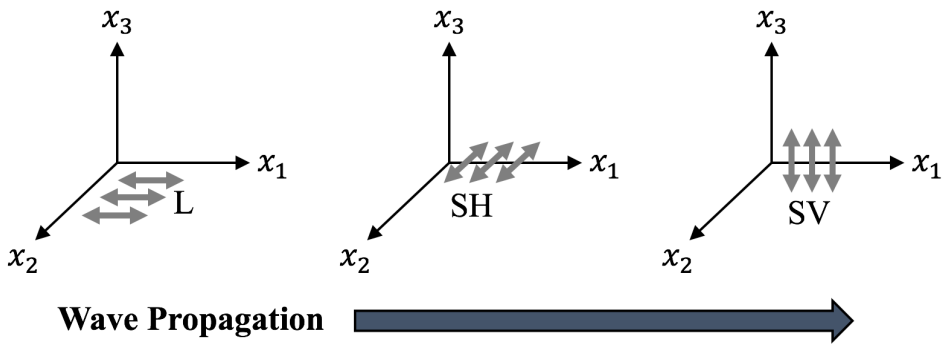

Fig. 3.1: Waves in solids

perpendicular to the propagation direction. These cases are referred to as quasi-longitudinal and quasi-shear. The wavefronts of the quasi-modes do not lie normal to the energy propagating direction, and thus the phase and group velocities do not coincide with each other. Among all of the classes in anisotropy, Transversely Isotropic (TI) medium is the most simple class. A TI medium is characterized by the existence of a single plane of isotropy and one single axis of rotational symmetry which is normal to the isotropic plane. All of the planes containing the axis of symmetry represents a plane of mirror symmetry. An example of a TI material is the on-axis unidirectional fiber composite lamina with the fibre are circular in cross section. A TI medium with

a vertical axis of symmetry leads to a horizontal plane of isotropy is called a *Vertical Transverse Isotropic* (VTI) medium. The medium with the symmetry axis tilted with respect to the earth's surface is called *Tilted Transversal Isotropic* (TTI) medium. Tilting the symmetry axis all the way up to the surface produces a *Horizontal Transversal Isotropic* (HTI) medium [93][11](Fig.3.2). Both

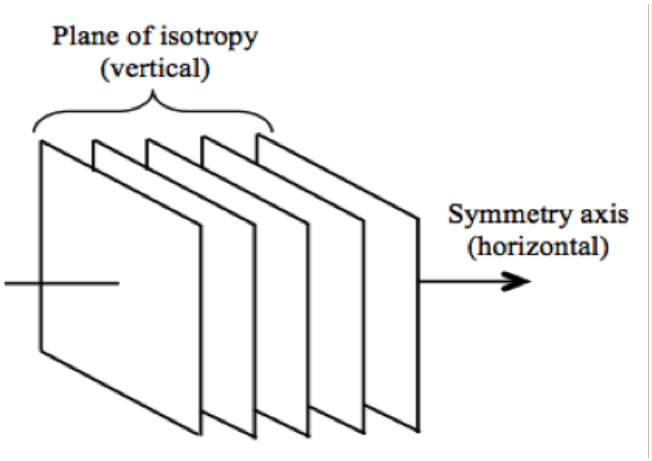

Fig. 3.2: HTI model due to a system of parallel vertical cracks

VTI and HTI media can be treated as the special cases of the orthorhombic symmetry class. The wave propagation velocity in TI media can be computed from the material density and the stiffness tensor that relates elastic stress and strain. In case of TI media (both VTI and HTI) the number of independent component in stiffness matrix is 5. The reduction process for HTI media is discussed thoroughly in the next section.

3.1 ANISOTROPIC SYMMETRY CLASSES

Recall (2.29), The generalized Hooke's law for a material is given as

$$\tau_{ij} = C_{ijkl}\varepsilon_{kl} \qquad (i,j,k,l = 1,2,3) \tag{3.1}$$

where,

- τ_{ij} is a second order tensor called stress tensor (9 components).

- ε_{kl} is second order tensor known as strain tensor (9 components).

- C_{ijkl} is a fourth order tensor known as stiffness tensor ($3^4 = 81$ independent elements). The individual elements are referred by various names as elastic constants.

To solve the above equation for strains in terms of stresses, the determinant of the stiffness matrix must be nonzero.
Stress tensor offers symmetric characteristics, that is, $\tau_{ij} = \tau_{ji}$. Thus there are six independent stress components. Hence from (3.1),

$$\tau_{ji} = C_{jikl}\varepsilon_{kl} \tag{3.2}$$

Subtracting (3.2) from (3.1) leads to the following equation

$$C_{ijkl} = C_{jikl}$$

There are six independent ways to express i and j reduces the number of independent stiffness component from 81 to 54, when l and k remain fixed.
Symmetric behavior of strain component can be expressed as $\varepsilon_{kl} = \varepsilon_{lk}$. So the Hooke's law can be written focussing on this symmetric behavior as

$$\tau_{ji} = C_{jilk}\varepsilon_{lk}$$

which returns

$$C_{ijkl} = C_{jilk}$$

Therefore six independent ways of expressing l and k leads to the reduction of independent stiffness component to 36, when i and j remain fixed. With

this reduced number of independent stress, strain and stiffness components, matrix form of the Hooke's law can be written as

$$\begin{bmatrix} \tau_{11} \\ \tau_{22} \\ \tau_{33} \\ \tau_{23} \\ \tau_{13} \\ \tau_{12} \end{bmatrix} = \begin{bmatrix} C_{1111} & C_{1122} & C_{1133} & C_{1123} & C_{1113} & C_{1112} \\ C_{2211} & C_{2222} & C_{2233} & C_{2223} & C_{2213} & C_{2212} \\ C_{3311} & C_{3322} & C_{3333} & C_{3323} & C_{3313} & C_{3312} \\ C_{2311} & C_{2322} & C_{2333} & C_{2323} & C_{2313} & C_{2312} \\ C_{1311} & C_{1322} & C_{1333} & C_{1323} & C_{1313} & C_{1312} \\ C_{1211} & C_{1222} & C_{1233} & C_{1223} & C_{1213} & C_{1212} \end{bmatrix} \begin{bmatrix} \varepsilon_{11} \\ \varepsilon_{22} \\ \varepsilon_{33} \\ 2\varepsilon_{23} \\ 2\varepsilon_{13} \\ 2\varepsilon_{12} \end{bmatrix}$$

The identical system of equations can be written in a two-subscript notation (usually called Voigt notation) as follows:

$$\tau_i = C_{ij}\varepsilon_j \tag{3.3}$$

where,

$$\begin{aligned} \tau_1 &= \tau_{11} & \varepsilon_1 &= \varepsilon_{11} \\ \tau_2 &= \tau_{22} & \varepsilon_2 &= \varepsilon_{22} \\ \tau_3 &= \tau_{33} & \varepsilon_3 &= \varepsilon_{33} \\ \tau_4 &= \tau_{23} & \varepsilon_4 &= 2\varepsilon_{23} \\ \tau_5 &= \tau_{31} & \varepsilon_5 &= 2\varepsilon_{31} \\ \tau_6 &= \tau_{12} & \varepsilon_6 &= 2\varepsilon_{12} \end{aligned}$$

Equation (3.3) can be expressed in matrix form as:

$$\begin{bmatrix} \tau_1 \\ \tau_2 \\ \tau_3 \\ \tau_4 \\ \tau_5 \\ \tau_6 \end{bmatrix} = \begin{bmatrix} C_{11} & C_{12} & C_{13} & C_{14} & C_{15} & C_{16} \\ C_{21} & C_{22} & C_{23} & C_{24} & C_{25} & C_{26} \\ C_{31} & C_{32} & C_{33} & C_{34} & C_{35} & C_{36} \\ C_{41} & C_{42} & C_{43} & C_{44} & C_{45} & C_{46} \\ C_{51} & C_{52} & C_{53} & C_{54} & C_{55} & C_{56} \\ C_{61} & C_{62} & C_{63} & C_{64} & C_{65} & C_{66} \end{bmatrix} \begin{bmatrix} \varepsilon_1 \\ \varepsilon_2 \\ \varepsilon_3 \\ \varepsilon_4 \\ \varepsilon_5 \\ \varepsilon_6 \end{bmatrix} \tag{3.4}$$

Equation (3.4) can be inverted so that the strains are given in terms of the stresses:

$$\begin{bmatrix} \varepsilon_1 \\ \varepsilon_2 \\ \varepsilon_3 \\ \varepsilon_4 \\ \varepsilon_5 \\ \varepsilon_6 \end{bmatrix} = \begin{bmatrix} S_{11} & S_{12} & S_{13} & S_{14} & S_{15} & S_{16} \\ S_{21} & S_{22} & S_{23} & S_{24} & S_{25} & S_{26} \\ S_{31} & S_{32} & S_{33} & S_{34} & S_{35} & S_{36} \\ S_{41} & S_{42} & S_{43} & S_{44} & S_{45} & S_{46} \\ S_{51} & S_{52} & S_{53} & S_{54} & S_{55} & S_{56} \\ S_{61} & S_{62} & S_{63} & S_{64} & S_{65} & S_{66} \end{bmatrix} \begin{bmatrix} \tau_1 \\ \tau_2 \\ \tau_3 \\ \tau_4 \\ \tau_5 \\ \tau_6 \end{bmatrix} \tag{3.5}$$

Where S_{ij}'s are called the compliances and the matrix of compliances is called the compliance matrix. The number of independent elastic constants can be reduced further, if there exists a *strain energy density function* W.
The Strain Energy Density Function W is given as

$$W = \frac{1}{2} C_{ij} \varepsilon_i \varepsilon_j$$

with the property

$$\tau_i = \frac{\partial W}{\partial \varepsilon_i}$$

A material with existence of W with the above property is called as *Hyperelastic Material*. For this kind of material, we can write,

$$W = \frac{1}{2} C_{ji} \varepsilon_j \varepsilon_i$$

which leads to the identity $C_{ij} = C_{ji}$. Thus, the stiffness matrix is symmetric. This symmetric matrix has 21 independent elastic constants. The material with 21 independent elastic constants is called as *Anisotropic Material*, and this is the most general case, called by *Triclinic* media. The stiffness matrix is given as follows:

$$C_{TRI} = \begin{bmatrix} C_{11} & C_{12} & C_{13} & C_{14} & C_{15} & C_{16} \\ & C_{22} & C_{23} & C_{24} & C_{25} & C_{26} \\ & & C_{33} & C_{34} & C_{35} & C_{36} \\ & & & C_{44} & C_{45} & C_{46} \\ & & & & C_{55} & C_{56} \\ & \text{symmetric} & & & & C_{66} \end{bmatrix} \tag{3.6}$$

Material symmetry

It should be recalled that both the stress and strain tensor follow transformation rule and so is the stiffness tensor.

$$\begin{aligned} \tau'_{ij} &= a_{ki}a_{lj}\tau_{kl} \\ \varepsilon'_{ij} &= a_{ki}a_{lj}\varepsilon_{kl} \\ C'_{ijkl} &= a_{mi}a_{nj}a_{rk}a_{sl}C_{mnrs} \end{aligned} \tag{3.7}$$

where a_{ij} are the direction cosines from i to j coordinate system. The prime indicates the quantity in new coordinate system.
When the function W is expanded using the contracted notations for strains and elastic constants, W has the following form:

$$\begin{aligned} W = \frac{1}{2}[&C_{11}\varepsilon_1^2 + 2C_{12}\varepsilon_1\varepsilon_2 + 2C_{13}\varepsilon_1\varepsilon_3 + 2C_{14}\varepsilon_1\varepsilon_4 + 2C_{15}\varepsilon_1\varepsilon_5 + 2C_{16}\varepsilon_1\varepsilon_6 \\ &+ C_{22}\varepsilon_2^2 + 2C_{23}\varepsilon_2\varepsilon_2 + 2C_{24}\varepsilon_2\varepsilon_4 + 2C_{25}\varepsilon_2\varepsilon_5 + 2C_{26}\varepsilon_2\varepsilon_6 \\ &+ C_{33}\varepsilon_3^2 + 2C_{34}\varepsilon_3\varepsilon_4 + 2C_{35}\varepsilon_3\varepsilon_5 + 2C_{36}\varepsilon_3\varepsilon_6 + C_{44}\varepsilon_4^2 \\ &+ 2C_{45}\varepsilon_4\varepsilon_5 + 2C_{46}\varepsilon_4\varepsilon_6 + C_{55}\varepsilon_5^2 + 2C_{56}\varepsilon_5\varepsilon_6 + C_{66}\varepsilon_6^2] \end{aligned} \tag{3.8}$$

The function W has the following form in terms of strain components:

$$\begin{aligned} W = W[&\varepsilon_1^2,\varepsilon_1\varepsilon_2,\varepsilon_1\varepsilon_3,\varepsilon_1\varepsilon_4,\varepsilon_1\varepsilon_5,\varepsilon_1\varepsilon_6,\varepsilon_2^2,\varepsilon_2\varepsilon_2,\varepsilon_2\varepsilon_4,\varepsilon_2\varepsilon_5,\varepsilon_2\varepsilon_6, \\ &\varepsilon_3^2,\varepsilon_3\varepsilon_4,\varepsilon_3\varepsilon_5,\varepsilon_3\varepsilon_6,\varepsilon_4^2,\varepsilon_4\varepsilon_5,\varepsilon_4\varepsilon_6,\varepsilon_5^2,\varepsilon_5\varepsilon_6,\varepsilon_6^2] \end{aligned} \tag{3.9}$$

With the above mentioned concept, consider some special cases of material symmetry.

Symmetry with respect to a plane

Let assume that the anisotropic material has only one plane of material symmetry. A material with one plane of material symmetry is called as *Monoclinic* material. Monoclinic symmetry has been identified from seismic measurement[101]. An exciting example of monoclinic medium with a vertical symmetry plane is that of a single vertical system of rotationally

non-invariant fractures with micro-corrugated faces in isotropic host rock [11]. Consider the $x_1 - x_2(x_3 = 0)$ plane as the plane of material symme-

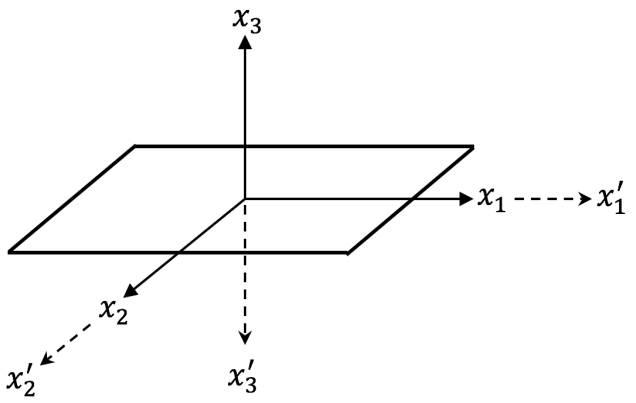

Fig. 3.3: Material behavior symmetric with a plane

try (Fig.3.3). This symmetry can be formulated with the change of axes as follows:

$$\begin{bmatrix} x_1' \\ x_2' \\ x_3' \end{bmatrix} = \begin{bmatrix} 1 & 0 & 0 \\ 0 & 1 & 0 \\ 0 & 0 & -1 \end{bmatrix} \begin{bmatrix} x_1 \\ x_2 \\ x_3 \end{bmatrix}$$

With this change of axes,

$$\frac{\partial x_i'}{\partial x_j} = \delta_{ij} \qquad j = 1,2$$
$$\frac{\partial x_i'}{\partial x_3} = -\delta_{i3}$$

So, the transformed strain tensor can be written as

$$\varepsilon_{11}' = \varepsilon_{11},$$
$$\varepsilon_{22}' = \varepsilon_{22},$$
$$\varepsilon_{33}' = \varepsilon_{33},$$
$$\varepsilon_{23}' = -\varepsilon_{23},$$
$$\varepsilon_{13}' = -\varepsilon_{13},$$
$$\varepsilon_{12}' = \varepsilon_{12}$$

Now, the function W can be expressed in terms of the strain components ε'_{ij}. If W is to be invariant, then it must be of the form

$$W = W[\varepsilon_1^2, \varepsilon_2^2, \varepsilon_3^2, \varepsilon_4^2, \varepsilon_5^2, \varepsilon_6^2, \varepsilon_1\varepsilon_2, \varepsilon_1\varepsilon_3, \varepsilon_1\varepsilon_6, \varepsilon_2\varepsilon_3, \varepsilon_2\varepsilon_6, \varepsilon_3\varepsilon_6, \varepsilon_4\varepsilon_5]$$

Comparing this with equation (3.9), it can be concluded that

$$C_{14} = C_{15} = C_{24} = C_{25} = C_{34} = C_{35} = C_{46} = C_{56} = 0$$

Thus, a monoclinic material can be characterized by 13 independent elastic components. With this reduced number of independent elastic components, stiffness matrix becomes

$$C_{MONO} = \begin{bmatrix} C_{11} & C_{12} & C_{13} & 0 & 0 & C_{16} \\ & C_{22} & C_{23} & 0 & 0 & C_{26} \\ & & C_{33} & 0 & 0 & C_{36} \\ & & & C_{44} & C_{45} & 0 \\ & & & & C_{55} & 0 \\ & \text{symmetric} & & & & C_{66} \end{bmatrix} \tag{3.10}$$

The number of independent stiffness can be reduced from 13 to 12 by aligning the horizontal coordinate axes with the polarization vectors of the vertically propagating shear waves, which eliminates the element C_{45} [40].

Symmetry with respect to two orthogonal plane

Assume that the material under consideration has one more plane, say $x_2 - x_3$ is plane of material symmetry along with $x_1 - x_2$ as in previous one (Fig.3.4). These two planes are orthogonal to each other. This can be mathematically formulated by the change of axes as

$$\begin{bmatrix} x'_1 \\ x'_2 \\ x'_3 \end{bmatrix} = \begin{bmatrix} -1 & 0 & 0 \\ 0 & 1 & 0 \\ 0 & 0 & -1 \end{bmatrix} \begin{bmatrix} x_1 \\ x_2 \\ x_3 \end{bmatrix}$$

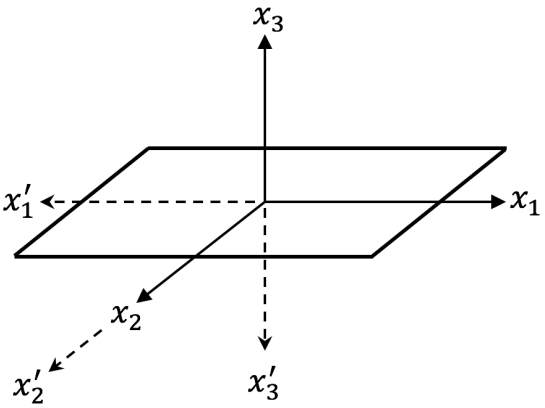

Fig. 3.4: Material behavior symmetric with two orthogonal plane

This change of axis causes

$$\frac{\partial x_i'}{\partial x_j} = -\delta_{ij} \qquad j = 1,3$$
$$\frac{\partial x_i'}{\partial x_2} = \delta_{i2}$$

This gives us the required strain relations as

$$\begin{aligned}
\varepsilon_{11}' &= \varepsilon_{11}, \\
\varepsilon_{22}' &= \varepsilon_{22}, \\
\varepsilon_{33}' &= \varepsilon_{33}, \\
\varepsilon_{23}' &= -\varepsilon_{23}, \\
\varepsilon_{13}' &= \varepsilon_{13}, \\
\varepsilon_{12}' &= -\varepsilon_{12}
\end{aligned}$$

We can get the function W simply by substituting ε_{ij}' in place of ε_{ij} and using contracted notations for the strains

$$W = W[\varepsilon_1^2, \varepsilon_2^2, \varepsilon_3^2, \varepsilon_4^2, \varepsilon_5^2, \varepsilon_6^2, \varepsilon_1\varepsilon_2, \varepsilon_1\varepsilon_3, \varepsilon_2\varepsilon_3]$$

From this, it is easy to see that

$$C_{16} = C_{26} = C_{36} = C_{45} = 0$$

Thus, the number of independent constants reduces to 9. The resulting stiffness matrix is given as

$$C_{ORTHO} = \begin{bmatrix} C_{11} & C_{12} & C_{13} & 0 & 0 & 0 \\ & C_{22} & C_{23} & 0 & 0 & 0 \\ & & C_{33} & 0 & 0 & 0 \\ & & & C_{44} & 0 & 0 \\ & & & & C_{55} & 0 \\ & \text{symmetric} & & & & C_{66} \end{bmatrix} \tag{3.11}$$

An *Orthotropic* material has two orthogonal planes as plane of symmetry. Usually, when two orthogonal planes are planes of material symmetry, the third mutually orthogonal plane is also plane of material symmetry. This type of medium can be caused by two or three mutually orthogonal fracture systems or two identical system of fractures making an arbitrary angle with each other. For such material, equation (3.5) can be re-write in terms of E, ν, and G as:

$$\begin{bmatrix} \varepsilon_1 \\ \varepsilon_2 \\ \varepsilon_3 \\ \varepsilon_4 \\ \varepsilon_5 \\ \varepsilon_6 \end{bmatrix} = \begin{bmatrix} \frac{1}{E_1} & -\frac{\nu_{21}}{E_2} & -\frac{\nu_{31}}{E_3} & 0 & 0 & 0 \\ -\frac{\nu_{12}}{E_1} & \frac{1}{E_2} & -\frac{\nu_{32}}{E_3} & 0 & 0 & 0 \\ -\frac{\nu_{13}}{E_1} & -\frac{\nu_{23}}{E_3} & \frac{1}{E_3} & 0 & 0 & 0 \\ 0 & 0 & 0 & \frac{1}{2G_{23}} & 0 & 0 \\ 0 & 0 & 0 & 0 & \frac{1}{2G_{13}} & 0 \\ 0 & 0 & 0 & 0 & 0 & \frac{1}{2G_{12}} \end{bmatrix} \begin{bmatrix} \tau_1 \\ \tau_2 \\ \tau_3 \\ \tau_4 \\ \tau_5 \\ \tau_6 \end{bmatrix} \tag{3.12}$$

The nine independent constants of (3.12) have the following meanings:

- E_i is the Young's modulus of the material in direction $i = 1,2,3$; for example, $\tau_1 = E_1\varepsilon_1$ for uniaxial tension in the direction 1.
- ν_{ij} is the Poisson's ratio representing the ratio of a transverse strain to the applied strain in uniaxial tension; for example, $\nu_{12} = -\varepsilon_2/\varepsilon_1$ for uniaxial tension in the direction 1.
- G_{ij} is the shear moduli representing the shear stiffness in the corresponding plane; for example, G_{12} is the shear stiffness for shearing in the $1-2$ plane.

From symmetry of the stiffness matrix,

$$\nu_{23}E_3 = \nu_{32}E_2$$
$$\nu_{13}E_3 = \nu_{31}E_1$$
$$\nu_{12}E_2 = \nu_{21}E_1$$

HTI media

This is obtained from an orthotropic material. We develop the constitutive relation for a material with transverse isotropy in $x_2 - x_3$ plane. This is obtained with the following form of the change of axes:

$$\begin{bmatrix} x_1' \\ x_2' \\ x_3' \end{bmatrix} = \begin{bmatrix} 1 & 0 & 0 \\ 0 & \cos\Theta & \sin\Theta \\ 0 & -\sin\Theta & \cos\Theta \end{bmatrix} \begin{bmatrix} x_1 \\ x_2 \\ x_3 \end{bmatrix}$$

Now, we have

$$\frac{\partial x_1'}{\partial x_1} = 1$$
$$\frac{\partial x_2'}{\partial x_2} = \frac{\partial x_3'}{\partial x_3} = \cos\Theta$$
$$\frac{\partial x_2'}{\partial x_3} = -\frac{\partial x_3'}{\partial x_2} = \sin\Theta$$
$$\frac{\partial x_1'}{\partial x_2} = -\frac{\partial x_1'}{\partial x_3} = \frac{\partial x_2'}{\partial x_1} = -\frac{\partial x_3'}{\partial x_1} = 0$$

From this, the strains in transformed coordinate system are given as:

$$\varepsilon_{11}' = \varepsilon_{11}$$
$$\varepsilon_{22}' = \varepsilon_{22}\cos^2\Theta + 2\varepsilon_{23}\cos\Theta\sin\Theta + \varepsilon_{33}\sin^2\Theta$$
$$\varepsilon_{33}' = \varepsilon_{22}\sin^2\Theta - 2\varepsilon_{23}\cos\Theta\sin\Theta + \varepsilon_{33}\cos^2\Theta$$
$$\varepsilon_{23}' = (\varepsilon_{33} - \varepsilon_{22})\cos\Theta\sin\Theta + \varepsilon_{23}(\cos^2\Theta - \sin^2\Theta)$$
$$\varepsilon_{13}' = (-\varepsilon_{12}\sin\Theta + \varepsilon_{13})\cos\Theta$$
$$\varepsilon_{12}' = (-\varepsilon_{12}\cos\Theta + \varepsilon_{13})\sin\Theta$$

Here, it is to be noted that the shear strains are the tensorial shear strain terms. For any angle of θ

$$\begin{aligned}\varepsilon'_{22} + \varepsilon'_{33} &= \varepsilon_{22} + \varepsilon_{33} \\ \varepsilon'_{22}\varepsilon'_{33} - (\varepsilon'_{23})^2 &= \varepsilon_{22}\varepsilon_{33} - (\varepsilon_{23})^2 \\ (\varepsilon'_{12})^2 + (\varepsilon'_{13})^2 &= (\varepsilon_{12})^2 + (\varepsilon_{13})^2\end{aligned}$$

and therefore, W must reduce to the form

$$W = W(\varepsilon_{22} + \varepsilon_{33}, \varepsilon_{22}\varepsilon_{33} - \varepsilon_{23}^2, \varepsilon_{33}, \varepsilon_{12}^2 + \varepsilon_{13}^2, |\varepsilon_{ij}|)$$

Now, substitute above equations in the function W using the C_{ij} matrix as given in equation (3.11) and express in terms ε'_{ij}. Then, for W to be invariant follow the following:

- If we observe the term containing $(\varepsilon_{11})^2$ and $(\varepsilon'_{11})^2$ then we conclude that C_{11} is unchanged.
- Now compare the terms containing $\varepsilon_{12}, \varepsilon_{13}$ and $\varepsilon'_{12}, \varepsilon'_{13}$. From this comparison we see that $C_{55} = C_{66}$.
- Now compare the terms containing $\varepsilon_{22}, \varepsilon_{33}, \varepsilon_{23}$ and $\varepsilon'_{22}, \varepsilon'_{33}, \varepsilon'_{23}$. This comparison leads to $C_{12} = C_{13}$, $C_{22} = C_{33}$ and $C_{44} = \frac{1}{2}(C_{22} - C_{23})$ and C_{23} is unchanged. We can write, $C_{23} = C_{33} - 2C_{44}$.

Thus, for transversely isotropic material with x_1 as plane of symmetry (in plane $x_2 - x_3$) the stiffness matrix becomes as:

$$C_{HTI} = \begin{bmatrix} C_{11} & C_{12} & C_{12} & 0 & 0 & 0 \\ & C_{22} & C_{23} & 0 & 0 & 0 \\ & & C_{22} & 0 & 0 & 0 \\ & & & \frac{C_{22}-C_{23}}{2} & 0 & 0 \\ & & & & C_{55} & 0 \\ & & \text{symmetric} & & & C_{55} \end{bmatrix} \tag{3.13}$$

Thus there are only 5 independent elastic constants for a HTI medium. Equation (3.12) can be written with a horizontal axis of symmetry:

$$\begin{bmatrix} \varepsilon_1 \\ \varepsilon_2 \\ \varepsilon_3 \\ \varepsilon_4 \\ \varepsilon_5 \\ \varepsilon_6 \end{bmatrix} = \begin{bmatrix} \frac{1}{E_1} & -\frac{\nu_{12}}{E_2} & -\frac{\nu_{31}}{E_2} & 0 & 0 & 0 \\ -\frac{\nu_{12}}{E_2} & \frac{1}{E_2} & -\frac{\nu_{32}}{E_2} & 0 & 0 & 0 \\ -\frac{\nu_{13}}{E_2} & -\frac{\nu_{23}}{E_2} & \frac{1}{E_2} & 0 & 0 & 0 \\ 0 & 0 & 0 & \frac{1}{2G_{23}} & 0 & 0 \\ 0 & 0 & 0 & 0 & \frac{1}{2G_{13}} & 0 \\ 0 & 0 & 0 & 0 & 0 & \frac{1}{2G_{13}} \end{bmatrix} \begin{bmatrix} \tau_1 \\ \tau_2 \\ \tau_3 \\ \tau_4 \\ \tau_5 \\ \tau_6 \end{bmatrix} \tag{3.14}$$

3.2 PLANE WAVES IN HTI MEDIA

Phase velocity

Analytical description of plane waves in HTI started with considering the equation of motion by dropping the body force. Expressing the tractions acting across the surface of that volume in terms of the stress tensor τ_{ij} yields

$$\rho \ddot{u}_i = \tau_{ij,j}$$

Generalized Hooke's law can be termed as:

$$\tau_{ij} = C_{ijkl}\varepsilon_{kl}$$

Here, C_{ijkl} is the fourth order stiffness tensor responsible for the material properties, and ε_{kl} is the strain tensor and can be defined as

$$\varepsilon_{kl} = \frac{1}{2}(u_{k,l} + u_{l,k})$$

Restricting the wave propagation theory to linearly elastic media by adopting Hooke's law is the most crucial simplifying assumption in both isotropic and anisotropic wave propagation. Substituting Hooke's law and the definition of

strain tensor into the general wave equation, and assuming that the stiffness coefficients are either constant or vary slowly in space, we find:

$$\begin{aligned}\rho\ddot{u}_i &= C_{ijkl}\frac{\partial \varepsilon_{kl}}{\partial x_j} \\ &= \frac{1}{2}C_{ijkl}\frac{\partial}{\partial x_j}(u_{k,l} + u_{l,k}) \\ &= \frac{1}{2}C_{ijkl}(u_{k,jl}) + \frac{1}{2}C_{ijkl}(u_{l,jk})\end{aligned}$$

Since the tensor C_{ijkl} is symmetrical with respect to the suffixes k and l, we can interchange these in the first term, which then becomes identical with the second term. Thus the equation of motion becomes

$$\rho\ddot{u}_i = C_{ijkl}u_{k,jl}$$

The above-mentioned equation is valid for elastic, arbitrary anisotropic, and homogeneous media. A solution to this equation can be assumed to take the form of a plane wave. This assumption is useful because any wave field can be described as a superposition of plane waves. The displacement of a particle at time t and distance x_1 due to a one-dimensional plane wave can be described using:

$$u_1(x_1, t) = A\cos(k_1x_1 - \omega t) \tag{3.15}$$

where A is the wave amplitude, ω is the angular frequency, and k is the wave number vector, related with the *phase* velocity (v) by $\omega = kv$. This is often expressed in exponential form using Euler's formula ($e^{ix} = \cos(x) + i\sin(x)$) as:

$$u_1(x_1, t) = Ae^{i(k_1x_1 - \omega t)} \tag{3.16}$$

A three-dimensional plane wave in a tensor notation is therefore given by

$$u_i = AU_ie^{i(k_ix_i - \omega t)} \tag{3.17}$$

where U_i represents the polarization vector $\mathbf{U}$. Differentiating the plane wave twice with respect to time yields:

$$\ddot{u}_i = \omega^2 AU_ie^{i(k_ix_i - \omega t)} = \omega^2 u_i \tag{3.18}$$

In a similar way, differentiating the wave equation twice with respect to distance yields:

$$u_{k,jl} = k_j k_l u_k \tag{3.19}$$

Combining (3.19) and (3.18) gives:

$$\rho\omega^2 u_i = C_{ijkl} k_j k_l u_k \tag{3.20}$$

The wave vector k_i is related to the wavenumber k through:

$$k_i = k n_i \tag{3.21}$$

where n_i represents the wavefront propagation direction. Using the definition of phase velocity ($k = \omega/v$) and equation (3.20) yields:

$$C_{ijkl} n_j n_l u_k = \rho v^2 u_i \tag{3.22}$$

Introducing Christoffel symbol, $G_{ik} = C_{ijkl} n_j n_l$, which depends on the medium properties (stifness) and the direction of wave propagation, (3.22) can be written in the following form:

$$G_{ik} u_k = \rho v^2 u_i \tag{3.23}$$

Following the properties of the stiffness tensor ($C_{ijkl} = C_{klij}$), the Christoffel matrix is symmetric ($G_{ik} = G_{ki}$). By considering 3D space as the space of all vectors, equation (3.23) can be considered as the eigenvalue problem, where ρv^2 is a constant called the eigenvalue and $\mathbf{U}$ is the associated eigenvector [63]. Thus, we can write:

$$[G_{ik} - \rho v^2 \mathbf{I}_M] \begin{bmatrix} U_1 \\ U_2 \\ U_3 \end{bmatrix} = 0_M \tag{3.24}$$

where, 0_M is an $M \times 1$ vectors of zeroes. Equation (3.24) is called a homogeneous equation because the right-hand side consists of zeros. It has a nontrivial solution ($\mathbf{U} \neq [0, 0, ..., 0]^T$) if and only if the determinant of $[G_{ik} - \rho v^2 \mathbf{I}_M]$ is zero, or

$$|G_{ik} - \rho v^2 \mathbf{I}_M| = 0 \tag{3.25}$$

where

$$|G_{ik} - \rho v^2 \mathbf{I}_M| = \begin{vmatrix} G_{11} - \rho v^2 & G_{12} & G_{13} \\ G_{21} & G_{22} - \rho v^2 & G_{23} \\ G_{31} & G_{32} & G_{33} - \rho v^2 \end{vmatrix} \tag{3.26}$$

Equation (3.26), also called the characteristics equation, is the polynomial of order 3 in ρv^2. As G_{ik} is symmetric, then all of the roots are real. They may, however, have repeated values, be negative, or zero. For any given phase direction $\mathbf{n}$ in anisotropic media, (3.26) yields three possible solutions; each solution represents one wave-type [8] of the phase velocity v, which corresponds to the longitudinal (P) wave, the fastest mode, and two shear (S) waves. Therefore, an anisotropic media (all other classes than isotropic) splits the shear wave into two modes with different velocities and polarization. The velocities of the split S-waves coincide with each other in specific directions leads to the shear wave singularities [22][40].

Phase velocities in HTI media can be calculated by proper handling of (3.26), focusing on the Christoffel matrix.

$$\begin{gathered} \mathbb{G} = \mathbb{D}\mathbb{C}\mathbb{D}^{\mathrm{T}} \\ \text{where}, \mathbb{D} = \begin{bmatrix} k_1 & 0 & 0 & 0 & k_3 & k_2 \\ 0 & k_2 & 0 & k_3 & 0 & k_1 \\ 0 & 0 & k_3 & k_2 & k_1 & 0 \end{bmatrix} \end{gathered} \tag{3.27}$$

$\mathbb{C}$ defines the stiffness matrix. The 3 by 6 derivative matrix $\mathbb{D}$, a function of the wavenumber vector (k_1,k_2,k_3), defines the plane wave propagation direction under consideration. For any wavenumber vector $\boldsymbol{k}$, the symmetry of the matrix $\mathbb{D}\mathbb{C}\mathbb{D}^{\mathrm{T}}$ assures that, we can always find three distinct modes associated with three orthogonal particle-motion directions.

The Christoffel matrix for HTI (symmetry about x_1 axis) media becomes:

$$\begin{bmatrix} k_1 & 0 & 0 & 0 & k_3 & k_2 \\ 0 & k_2 & 0 & k_3 & 0 & k_1 \\ 0 & 0 & k_3 & k_2 & k_1 & 0 \end{bmatrix} \begin{bmatrix} C_{11} & C_{12} & C_{12} & 0 & 0 & 0 \\ & C_{22} & C_{22} - 2C_{44} & 0 & 0 & 0 \\ & & C_{22} & 0 & 0 & 0 \\ & & & C_{44} & 0 & 0 \\ & & & & C_{55} & 0 \\ & & \text{symmetric} & & & C_{55} \end{bmatrix} \begin{bmatrix} k_1 & 0 & 0 \\ 0 & k_2 & 0 \\ 0 & 0 & k_3 \\ 0 & k_3 & k_2 \\ k_3 & 0 & k_1 \\ k_2 & k_1 & 0 \end{bmatrix}$$

which reduces to

$$\begin{bmatrix} C_{11}k_1^2 + C_{55}k_2^2 + C_{55}k_3^2 & (C_{12} + C_{55})k_1k_2 & (C_{12} + C_{55})k_1k_3 \\ (C_{12} + C_{55})k_1k_2 & C_{55}k_1^2 + C_{22}k_2^2 + C_{44}k_3^2 & (C_{22} - C_{44})k_2k_3 \\ (C_{12} + C_{55})k_1k_3 & (C_{22} - C_{44})k_2k_3 & C_{55}k_1^2 + C_{44}k_2^2 + C_{22}k_3^2 \end{bmatrix} \tag{3.28}$$

Inserting the concept of wave number vector from (3.21), components of the christoffel matrix can be written as

$$\begin{aligned} G_{11} &= C_{11}n_1^2 + C_{55}n_2^2 + C_{55}n_3^2 \\ G_{22} &= C_{55}n_1^2 + C_{22}n_2^2 + C_{44}n_3^2 \\ G_{33} &= C_{55}n_1^2 + C_{44}n_2^2 + C_{22}n_3^2 \\ G_{12} &= G_{21} = (C_{12} + C_{55})n_1n_2 \\ G_{23} &= G_{32} = (C_{22} - C_{44})n_2n_3 \\ G_{13} &= G_{31} = (C_{12} + C_{55})n_1n_3 \end{aligned} \tag{3.29}$$

In TI media all planes containing the symmetry axis are equivalent, wave propagation can be studies in single vertical plane. For this study, considering $[x_1 - x_3]$-plane ($n_2 = 0$) gives the following equation from (3.24)

$$\begin{bmatrix} C_{11}n_1^2 + C_{55}n_3^2 - \rho v^2 & 0 & (C_{12} + C_{55})n_1n_3 \\ 0 & C_{55}n_1^2 + C_{44}n_3^2 - \rho v^2 & 0 \\ (C_{12} + C_{55})n_1n_3 & 0 & C_{55}n_1^2 + C_{22}n_3^2 - \rho v^2 \end{bmatrix} \begin{bmatrix} U_1 \\ U_2 \\ U_3 \end{bmatrix} = 0 \tag{3.30}$$

Because in the $[x_1 - x_3]$-plane $G_{12} = G_{21} = G_{23} = G_{32} = 0$, (3.30) splits into independent equations for the pure transverse ($U_1 = U_3 = 0$) and in-plane ($U_2 = 0$) particle motion. Expressing the unit vector $\mathbf{n}$ in equation (3.30) in terms of the phase angle θ with the symmetry (x_1) axis, i.e. $n_1 = \cos\theta, n_3 = \sin\theta$

$$\begin{bmatrix} C_{11}\cos^2\theta + C_{55}\sin^2\theta - \rho v^2 & 0 & (C_{12} + C_{55})\cos\theta\sin\theta \\ 0 & C_{55}\cos^2\theta + C_{44}\sin^2\theta - \rho v^2 & 0 \\ (C_{12} + C_{55})\cos\theta\sin\theta & 0 & C_{55}\cos^2\theta + C_{22}\sin^2\theta - \rho v^2 \end{bmatrix} \begin{bmatrix} U_1 \\ U_2 \\ U_3 \end{bmatrix} = 0 \tag{3.31}$$

Setting ($U_1 = U_3 = 0$) resulting the phase velocity of the transversely polarized mode

$$v_{SH}(\theta) = \sqrt{\frac{C_{55}\cos^2\theta + C_{44}\sin^2\theta}{\rho}} \tag{3.32}$$

Equation (3.32) describes the SH-wave with the polarization vector confined to the horizontal plane. The another two eigensolutions must be orthogonal to each other, first and third equation of (3.31) gives the following set:

$$\begin{bmatrix} C_{11}\cos^2\theta + C_{55}\sin^2\theta - \rho v^2 & (C_{12}+C_{55})\sin\theta\cos\theta \\ (C_{12}+C_{55})\sin\theta\cos\theta & C_{55}\cos^2\theta + C_{22}\sin^2\theta - \rho v^2 \end{bmatrix} \begin{bmatrix} U_1 \\ U_3 \end{bmatrix} = 0 \quad (3.33)$$

Equation (3.33) depicts that, phase velocity and polarization of P- and SV-waves depend on four stiffness coefficients (C_{11}, C_{22}, C_{55}, and C_{12}).
The phase velocity thus can be derived by inserting the condition stated in equation (3.25) into equation (3.33):

$$\begin{aligned} 2\rho v^2(\theta) &= (C_{11}+C_{66})\cos^2\theta + (C_{33}+C_{66})\sin^2\theta \\ &\pm \sqrt{[(C_{11}-C_{66})\cos^2\theta - (C_{33}-C_{66})\sin^2\theta]^2 + 4(C_{13}+C_{66})^2\sin^2\theta\cos^2\theta} \end{aligned} \quad (3.34)$$

where the plus sign in front of the radical corresponds to the P-wave, and the minus sign to the SV-wave. If the waves travel along the symmetry (x_1) axis ($\theta = 0$), equation (3.33) further simplifies to

$$\begin{bmatrix} C_{11} - \rho v^2 & 0 \\ 0 & C_{55} - \rho v^2 \end{bmatrix} \begin{bmatrix} U_1 \\ U_3 \end{bmatrix} = 0 \quad (3.35)$$

One of the solutions of (3.35) corresponds to a pure P-wave polarized in the direction of propagation:

$$v_{P(\theta=0)} = \sqrt{\frac{C_{11}}{\rho}}; \qquad U_1 = 1, U_3 = 0 \quad (3.36)$$

The other solution is a shear (SV) wave with a horizontal in-plane polarization

$$v_{SV(\theta=0)} = \sqrt{\frac{C_{55}}{\rho}}; \qquad U_1 = 0, U_3 = 1 \quad (3.37)$$

and from equation(3.32)

$$v_{SH(\theta=0)} = \sqrt{\frac{C_{55}}{\rho}} \quad (3.38)$$

Let consider the wave propagating in the x_3 direction, that means $\theta = \pi/2$, equation (3.35) and (3.32) gives:

$$\begin{aligned} v_{P(\theta=\pi/2)} &= \sqrt{\frac{C_{22}}{\rho}} \qquad U_1 = 0, U_3 = 1 \\ v_{SV(\theta=\pi/2)} &= \sqrt{\frac{C_{55}}{\rho}} \qquad U_1 = 1, U_3 = 0 \\ v_{SH(\theta=\pi/2)} &= \sqrt{\frac{C_{44}}{\rho}} \end{aligned} \tag{3.39}$$

Due to the transversal isotropic condition in $x_2 - x_3$ plane, wave propagating in the x_2 direction follows the same equation as (3.39).
So, in an orthogonal coordinate system, for HTI media with x_1 axis as the symmetrical axis, phase velocities can be observed as

$$\begin{pmatrix} v_{11} & v_{12} & v_{13} \\ v_{21} & v_{22} & v_{23} \\ v_{31} & v_{32} & v_{33} \end{pmatrix} = \begin{pmatrix} \sqrt{\frac{C_{11}}{\rho}} & \sqrt{\frac{C_{55}}{\rho}} & \sqrt{\frac{C_{55}}{\rho}} \\ \sqrt{\frac{C_{55}}{\rho}} & \sqrt{\frac{C_{22}}{\rho}} & \sqrt{\frac{C_{44}}{\rho}} \\ \sqrt{\frac{C_{55}}{\rho}} & \sqrt{\frac{C_{44}}{\rho}} & \sqrt{\frac{C_{22}}{\rho}} \end{pmatrix}$$

Although (3.34) is not complicated and can be efficiently used for numerical computations, it provides the little insight into the dependence of phase velocity on the elastic properties of the medium. A much more convenient way to simplify the phase-velocity function in HTI media is to replace the standard notation by Thomsen parameters [91].

3.3 CONCEPT OF GROUP VELOCITY

The group velocity (v_g) of a wave is the velocity with which the overall shape of the wave's amplitudes propagates through space. It determines the direction and speed of energy propagation. The difference between the group velocity and phase velocity vectors caused by velocity variations with either frequency or angle. Figure 3.5 shows the group velocity vector in a homogeneous medium is aligned with the source receiver direction, in contrast with that, the phase velocity vector is orthogonal to the wavefront. Because of the

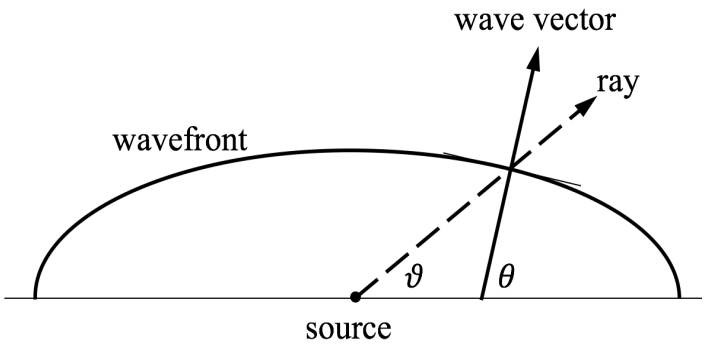

Fig. 3.5: In a homogeneous anisotropic medium, the group-velocity (ray) vector points from the source to the receiver (angle ϑ). The corresponding phase-velocity (wave) vector is orthogonal to the wavefront (angle θ)

presence of anisotropy in the medium, the wavefront is not spherical. Figure 3.6 illustrates that the envelope of a wave packet is propagating with a group velocity. Auld explains the concept of phase and group velocity by considering a modulated wave constructed of two waves of slightly different wave number (k) and angular frequency (ω) [8].
Consider two plane wave propagating in x_1 direction with nearly close k and ω as:

$$u_3^1 = Ae^{i(k_1x_1-\omega_1t)}$$
$$u_3^2 = Ae^{i(k_2x_1-\omega_2t)}$$

Resultant wave composed of superposition of u_3^1 and u_3^2:

$$\begin{aligned}
u_3 &= u_3^1 + u_3^2 \\
&= A\sin(k_1x_1-\omega_1t) + A\sin(k_2x_1-\omega_2t) \\
&= 2A\Big[\sin\frac{(k_1+k_2)x_1-(\omega_1+\omega_2)t}{2}\cos\frac{(k_1-k_2)x_1-(\omega_1-\omega_2)t}{2}\Big] \\
&= 2A\Big[\sin\Big\{\Big(\frac{k_1+k_2}{2}\Big)x_1-\Big(\frac{\omega_1+\omega_2}{2}\Big)t\Big\}\cos\Big\{\Big(\frac{k_1-k_2}{2}\Big)x_1-\Big(\frac{\omega_1-\omega_2}{2}\Big)t\Big\}\Big] \\
&= 2A\sin(\overline{k}x_1-\overline{\omega}t)\cos\Big(\frac{\Delta k}{2}x_1-\frac{\Delta\omega}{2}t\Big)
\end{aligned}$$

The first term in this equation is the high frequency carrier wave. The velocity of the carrier wave can be seen to tend to the phase velocity as the small

differences in k and ω tend to zero. The second term is the lower frequency modulation envelope and the group velocity of this envelope is given by:

$$v_g = \frac{\Delta\omega}{\Delta k} \rightarrow \frac{\partial\omega}{\partial k} \tag{3.40}$$

So the resultant equation can be expressed as

$$u_3 = 2A \sin\bar{k}(x_1 - v_p t) \cos\frac{\Delta k}{2}(x_1 - v_g t) \tag{3.41}$$

Rearranging as:

$$u_3 = Z \sin(\bar{k}x_1 - \overline{\omega}t) \tag{3.42}$$

where Z denotes the envelope function of the wave packet and it follows the characteristics of steady state wave equation.

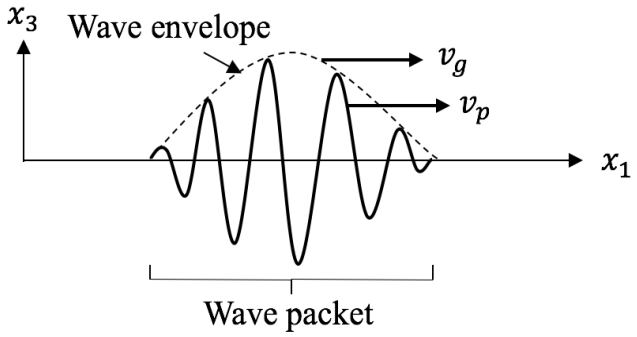

Fig. 3.6: Wave packet advancing forward in isotropic media, i.e. envelope and carrier wave forwarding in the same direction

The envelope function carries the information of energy propagation. In case of the isotropic continuum, the envelope function and the carrier wave propagating in the same direction (Fig.3.6), whereas in anisotropic media, they follow the different path.

4

MATERIAL PROPERTIES AND MECHANICS OF COMPOSITE LAMINATES

To make calculations and communication about the laminate easier, choosing a coordinate system is important. Furthermore, the coordinate system used for the laminate usually determine its stacking sequence. In this study, the x-axis is chosen for all 0° plies and consequently y-axis for all 90° plies. The angle starts from the x-axis and rotate to the fiber direction of the ply being defined. Clockwise rotations are positive angles, and counterclockwise rotations are negative angles. The symmetric laminate started with the angle of outermost ply and written up the ply angles sequentially until the mid-plane, separated by a comma, subscripted the brackets with an "s". Further simplification is made with two or more plies of the same orientation are grouped together. As example: $[\theta]_n$ means the laminate made-up with n-plies where each ply having fibre direction of θ°.

According to the deduced stiffness matrix in equation (3.13) for HTI elastic media, the following elastic properties of carbon-epoxy considered in this study (values are in GPa):

$$C_{HTI} = \begin{bmatrix} 96.0 & 3.60 & 3.60 & 0 & 0 & 0 \\ & 9.60 & 7.01 & 0 & 0 & 0 \\ & & 9.60 & 0 & 0 & 0 \\ & & & 1.23 & 0 & 0 \\ & & & & 3.30 & 0 \\ & \text{symmetric} & & & & 3.30 \end{bmatrix} \tag{4.1}$$

Where, the components are related by

$$\begin{aligned} C_{11} &= \frac{E_t(1-\nu_p^2)}{1-\nu_p^2-2\nu_p\nu_{pt}-\nu_p\nu_{pt}\nu_{tp}} \\ C_{22} &= \frac{E_p(1-\nu_{pt}\nu_{tp})}{1-\nu_p^2-2\nu_p\nu_{pt}-\nu_p\nu_{pt}\nu_{tp}} \\ C_{23} &= \frac{E_p(\nu_p+\nu_{pt}\nu_{tp})}{1-\nu_p^2-2\nu_p\nu_{pt}-\nu_p\nu_{pt}\nu_{tp}} \\ C_{12} &= \frac{E_p(\nu_p+\nu_p\nu_{tp})}{1-\nu_p^2-2\nu_p\nu_{pt}-\nu_p\nu_{pt}\nu_{tp}} \\ C_{55} &= \mu_t \\ \frac{\nu_{tp}}{E_t} &= \frac{\nu_{pt}}{E_p} \end{aligned}$$

Mass density of the material is taken as 1500 $\mathrm{kg/m^3}$. Based on these parameters, the calculated fundamental antisymmetric mode phase velocity dispersion curve in the fiber direction and perpendicular to the fiber direction for such material depicted in Fig.4.1. In this study, the frequency of 30 kHz is considered for analysis. Directional dependence of the phase velocity is a key property of an anisotropic material. To investigate this criteria for unidirectional ply laminates, the fiber orientation must be transformed to the new coordinate system. Any cartesian coordinate system (xyz), suppose we transform to a new coordinate system ($x'y'z'$) (consider both coordinate system

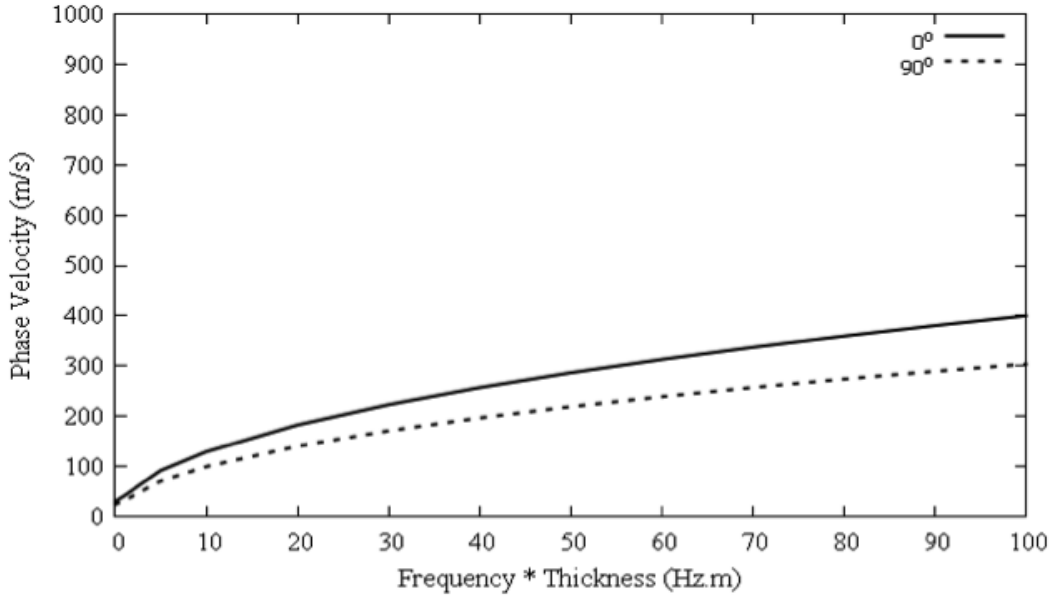

Fig. 4.1: Calculated A_0-mode phase velocity dispersion curves for HTI material

share same origin), is obtained by rotating the coordinate axes through an angle θ about the vertical (z) axis and the direction cosines of such transformation matrix can be written as:

$$\begin{bmatrix} \cos\theta & \sin\theta & 0 \\ -\sin\theta & \cos\theta & 0 \\ 0 & 0 & 1 \end{bmatrix}$$

For a 4^{th} order matrix, the transformation matrix becomes [12]

$$\mathbb{T} = \begin{bmatrix} \cos^2\theta & \sin^2\theta & 0 & 0 & 0 & 2\sin\theta\cos\theta \\ \sin^2\theta & \cos^2\theta & 0 & 0 & 0 & -2\sin\theta\cos\theta \\ 0 & 0 & 1 & 0 & 0 & 0 \\ 0 & 0 & 0 & \cos\theta & -\sin\theta & 0 \\ 0 & 0 & 0 & \sin\theta & \cos\theta & 0 \\ -\sin\theta\cos\theta & \sin\theta\cos\theta & 0 & 0 & 0 & -\sin^2\theta + \cos^2\theta \end{bmatrix}$$

Based on above discussion, for a given stiffness matrix $\mathbb{C}$ (3.13), transformed components of new stiffness matrix can be shown as:

$$\mathbb{C}' = \begin{bmatrix} C'_{11} & C'_{12} & C'_{13} & 0 & 0 & 0 \\ & C'_{22} & C'_{23} & 0 & 0 & 0 \\ & & C'_{33} & 0 & 0 & 0 \\ & & & C'_{44} & 0 & 0 \\ & & & & C'_{55} & 0 \\ & \text{symmetric} & & & & C'_{66} \end{bmatrix}$$

and formulated by:

$$[\mathbb{C}'] = [\mathbb{T}][\mathbb{C}][\mathbb{T}^{-1}]$$

The transformed components are evaluated as:

$$\begin{aligned}
C'_{11} &= C_{11}\cos^4\theta + 2C_{12}\sin^2\theta\cos^2\theta + C_{22}\sin^4\theta + 4C_{55}\sin^2\theta\cos^2\theta \\
C'_{12} &= (C_{11} + C_{22} - 4C_{55})\sin^2\theta\cos^2\theta + C_{12}(\sin^4\theta + \cos^4\theta) \\
C'_{13} &= C_{12}\cos^2\theta + C_{23}\sin^2\theta \\
C'_{22} &= C_{11}\sin^4\theta + C_{22}\cos^4\theta + 2(C_{12} + 2C_{55})\sin^2\theta\cos^2\theta \\
C'_{23} &= C_{12}\sin^2\theta + C_{23}\cos^2\theta \\
C'_{33} &= C_{33} \\
C'_{44} &= \left(\frac{C_{22} - C_{23}}{2}\right)\cos^2\theta + C_{55}\sin^2\theta \\
C'_{55} &= \left(\frac{C_{22} - C_{23}}{2}\right)\sin^2\theta + C_{55}\cos^2\theta \\
C'_{66} &= (C_{11} + C_{22} - 2C_{12} - 2C_{55})\sin^2\theta\cos^2\theta + C_{55}(\cos^4\theta + \sin^4\theta)
\end{aligned}$$

Polar diagram in Fig. 4.2 depicts the angular dependency of phase velocity of the A_0-mode Lamb wave for $f = 30$ kHz, evidencing the maximum velocity along 0° direction and it illustrates that the phase velocity direction is differ from the group velocity direction at almost every angle. The figure shows that the phase velocity of the first antisymmetric Lamb mode at 30 kHz varies between 221 m/s in the fiber direction and 170 m/s in the direction perpendicular to the fibers. Polar plot shown in Fig. 4.3 highlights the radial trend, where the origin of polar reference is shifted by 150 m/s.

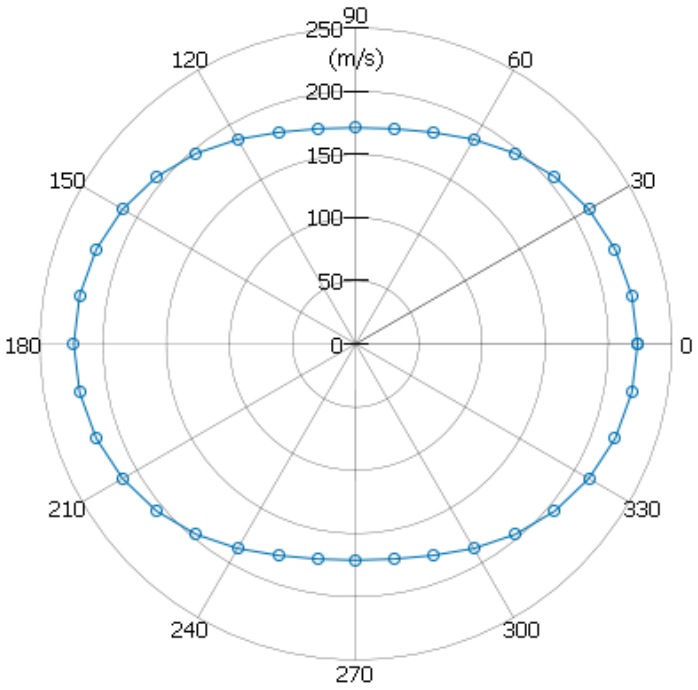

Fig. 4.2: Theoretically calculated angular dependency of phase velocity of the A_0-mode Lamb wave for $f = 30$ kHz

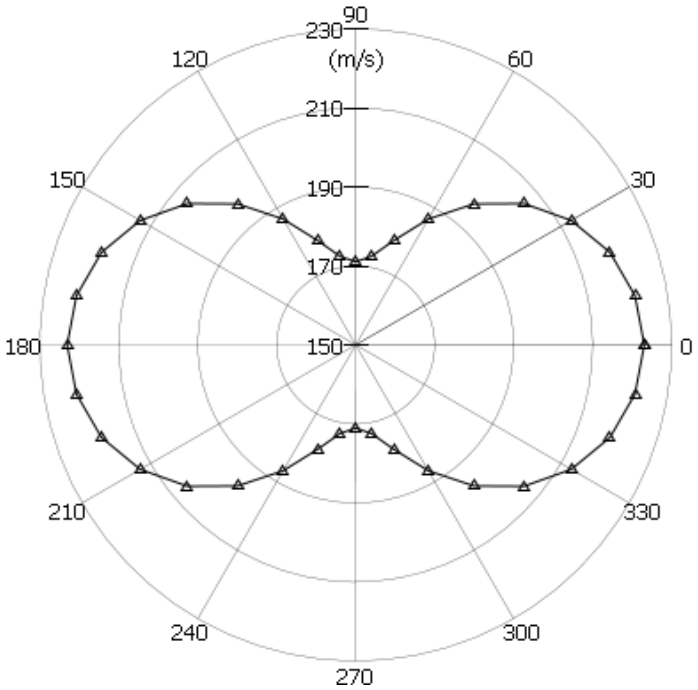

Fig. 4.3: Polar variation of phase velocity of the A_0-mode Lamb wave for $f = 30$ kHz

According to the new coordinate system and based on the material properties, for fiber direction 30°, stiffness matrix of an orthotropic materials becomes, and its corresponding dispersion curve is shown in Fig.4.4.

$$\mathbb{C}'_{30^\circ} = \begin{bmatrix} 55.60 & 19.56 & 4.45 & 0 & 0 & 0 \\ & 15.22 & 6.15 & 0 & 0 & 0 \\ & & 9.60 & 0 & 0 & 0 \\ & & & 1.80 & 0 & 0 \\ & & & & 2.80 & 0 \\ & \text{symmetric} & & & & 19.27 \end{bmatrix}$$

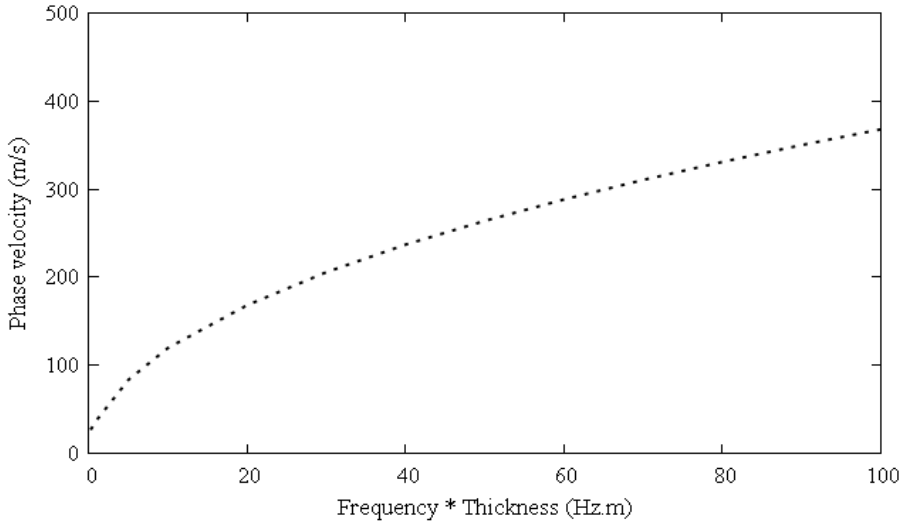

Fig. 4.4: Theoretically calculated A_0-mode dispersion curve for 30° fiber direction

For 60° fiber direction , dispersion curve is in Fig.4.5.

$$\mathbb{C}'_{60^\circ} = \begin{bmatrix} 15.23 & 19.56 & 6.16 & 0 & 0 & 0 \\ & 58.38 & 4.45 & 0 & 0 & 0 \\ & & 9.60 & 0 & 0 & 0 \\ & & & 2.80 & 0 & 0 \\ & & & & 1.80 & 0 \\ & \text{symmetric} & & & & 19.27 \end{bmatrix}$$

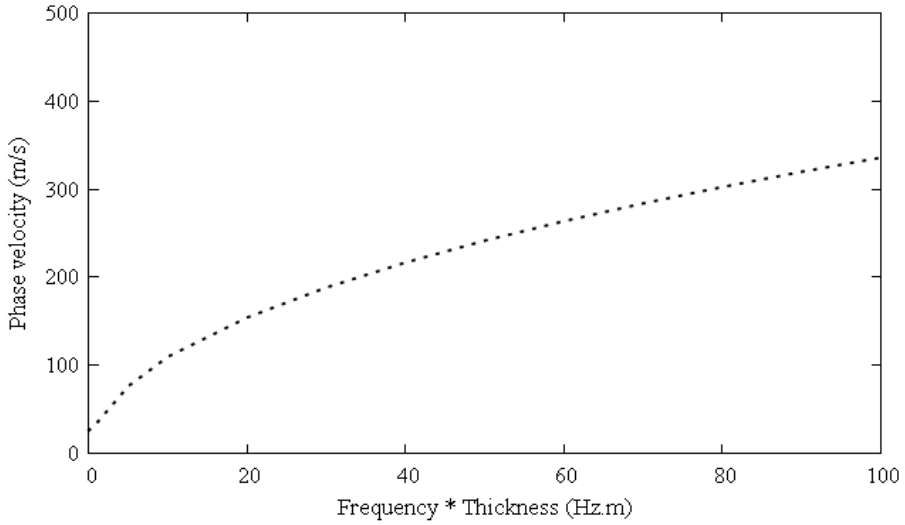

Fig. 4.5: Theoretically calculated A_0-mode dispersion curve for 60° fiber direction

4.2 MECHANICS OF COMPOSITE LAMINATES

The following assumptions are taken to analysis the composite laminates [64]:

1. Thickness of the laminate is very small compared to its other dimensions.
2. The entire plies are perfectly bonded.
3. The laminae and laminate are linear elastic.
4. The through thickness stresses and strains are negligible.

Consider a HTI material, the in-plane stress-strain relations can be written as:

$$\begin{Bmatrix} \sigma_1 \\ \sigma_2 \\ \tau_6 \end{Bmatrix} = \begin{bmatrix} Q_{11} & Q_{12} & 0 \\ & Q_{22} & 0 \\ \text{symmetric} & & Q_{55} \end{bmatrix} \begin{Bmatrix} \varepsilon_1 \\ \varepsilon_2 \\ \gamma_6 \end{Bmatrix}$$

This reduced stiffness matrix $\mathbb{Q}$ have the same subscript notation like $\mathbb{C}$ and follows the engineering constant likely, describes the elastic behavior of the ply in-plane loading. As the stress in each ply varies through the thickness

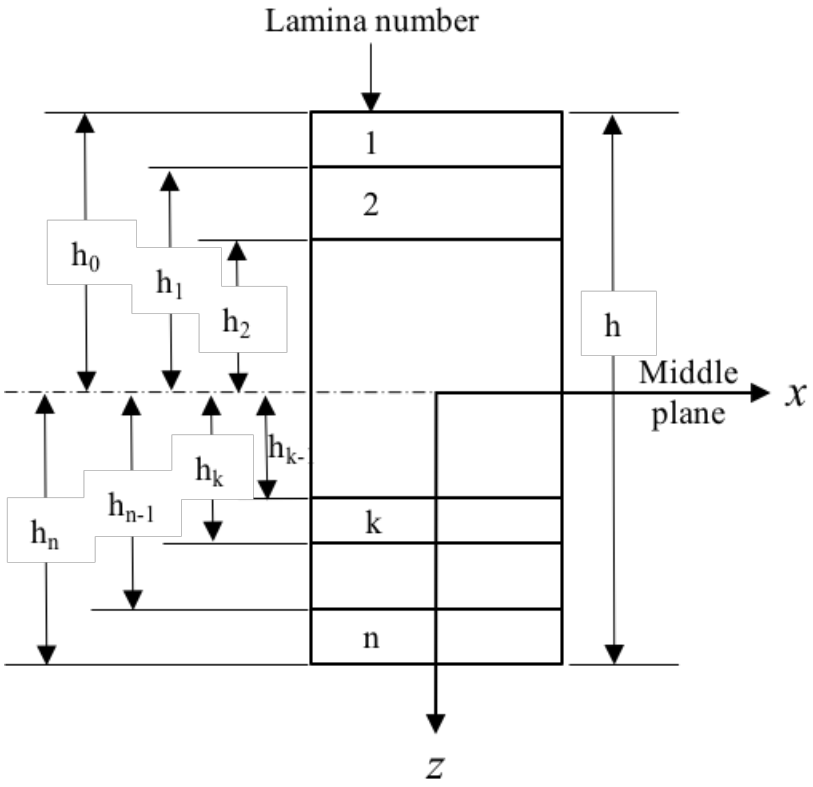

Fig. 4.6: Procedure of distance measurement from the middle plane to the layer of CL to calculate ABD matrix

of the laminate, constitutive equation for such laminate can be expressed in terms of resultant forces (N) and moments (M) and formulated in a matrix form as:

$$\begin{Bmatrix} N_1 \\ N_2 \\ N_6 \\ M_1 \\ M_2 \\ M_6 \end{Bmatrix} = \begin{bmatrix} A_{11} & A_{12} & A_{16} & B_{11} & B_{12} & B_{16} \\ A_{21} & A_{22} & A_{26} & B_{21} & B_{22} & B_{26} \\ A_{61} & A_{62} & A_{66} & B_{61} & B_{62} & B_{66} \\ B_{11} & B_{12} & B_{16} & D_{11} & D_{12} & D_{16} \\ B_{21} & B_{22} & B_{26} & D_{21} & D_{22} & D_{26} \\ B_{61} & B_{62} & B_{66} & D_{61} & D_{62} & D_{66} \end{bmatrix} \begin{Bmatrix} \varepsilon_1^0 \\ \varepsilon_2^0 \\ \gamma_6^0 \\ \kappa_1 \\ \kappa_2 \\ \kappa_6 \end{Bmatrix}$$

Where,

$$A_{ij} = \text{Extensional stiffness matrix} = \sum_{\kappa=1}^{n} (\overline{Q}_{ij})_n (h_\kappa - h_{\kappa-1})$$

$$B_{ij} = \text{Coupling stiffness matrix} = \frac{1}{2} \sum_{\kappa=1}^{n} (\overline{Q}_{ij})_n (h_\kappa^2 - h_{\kappa-1}^2)$$

$$D_{ij} = \text{Bending stiffness matrix} = \frac{1}{3} \sum_{\kappa=1}^{n} (\overline{Q}_{ij})_n (h_\kappa^3 - h_{\kappa-1}^3)$$

$$\varepsilon^0 = \text{Vector of mid-plane strain}$$

$$\kappa = \text{Vector of mid-plane curvature}$$

$$h_\kappa = \text{Vertical position in the ply from mid-plane}$$

$$\overline{Q}_{ij} = \text{Transformed reduced stiffness matrix in arbitrary direction}$$

$$= \begin{bmatrix} \overline{Q}_{11} & \overline{Q}_{12} & \overline{Q}_{16} \\ & \overline{Q}_{22} & \overline{Q}_{26} \\ \text{symmetric} & & \overline{Q}_{66} \end{bmatrix}$$

The 6×6 ABD matrix serves a connection between the applied loads and the associated strains in the laminate. Moreover, it defines the elastic properties of the entire laminate. For any arbitrary fiber direction θ, components of the reduced matrix can be calculated by:

$$\overline{Q}_{11} = Q_{11}\cos^4\theta + Q_{22}\sin^4\theta + 2(Q_{12} + 2Q_{66})\sin^2\theta\cos^2\theta$$

$$\overline{Q}_{22} = Q_{11}\sin^4\theta + Q_{22}\cos^4\theta + 2(Q_{12} + 2Q_{66})\sin^2\theta\cos^2\theta$$

$$\overline{Q}_{12} = (Q_{11} + Q_{22} - 4Q_{66})\sin^2\theta\cos^2\theta + Q_{12}(\cos^4\theta + \sin^4\theta)$$

$$\overline{Q}_{66} = (Q_{11} + Q_{22} - 2Q_{12} - 2Q_{66})\sin^2\theta\cos^2\theta + Q_{66}(\cos^4\theta + \sin^4\theta)$$

$$\overline{Q}_{16} = (Q_{11} - Q_{12} - 2Q_{66})\sin\theta\cos^3\theta - (Q_{22} - Q_{12} - 2Q_{66})(\cos\theta\sin^3\theta)$$

$$\overline{Q}_{16} = (Q_{11} - Q_{12} - 2Q_{66})\cos\theta\sin^3\theta - (Q_{22} - Q_{12} - 2Q_{66})(\sin\theta\cos^3\theta)$$

4.2.1 *Quasi-Isotropic (QI) laminate*

QI CL has commonly been popular in the industries due to their multi-axial load handling capability. As some elastic properties of QI CL approximate the equivalent isotropic properties in engineering materials, they are suitable

for traditional industrial design. Although fiber reinforced composites made up from unidirectional plies enable optimized lay-ups for specific applications, symmetric QI lay-ups are used in practice. The $\pi/4([0/\pm 45/90]_s)$ combination of balanced carbon-epoxy QI CL is considered in this study. Fibre orientation of such laminate illustrates in Fig. 4.7.

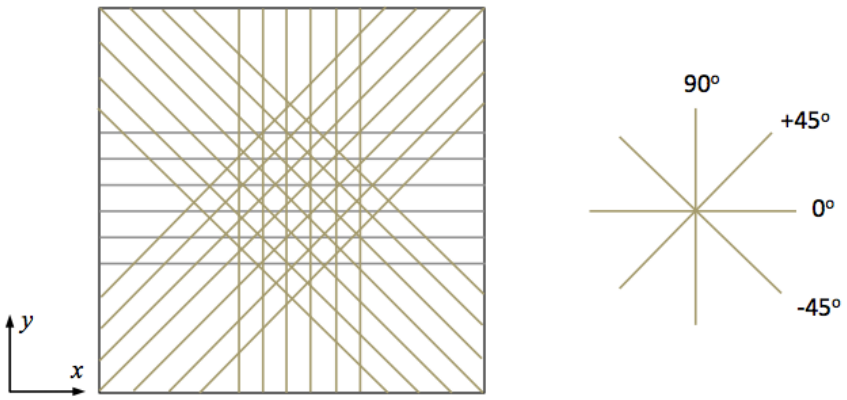

Fig. 4.7: Fibre orientation of $[0,\pm 45,90]_s$ QI laminate

Stacking sequence of such QI laminate can be shown in Fig. 4.8(Left)

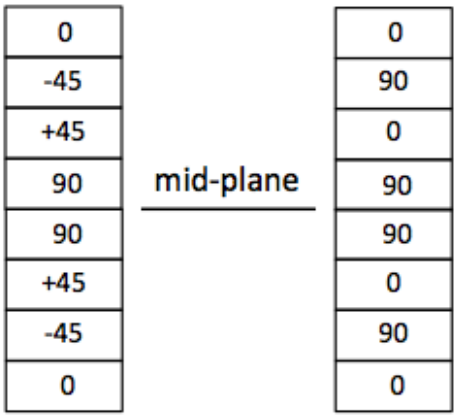

Fig. 4.8: Stacking sequence of (Left) $[0,\pm 45,90]_s$ QI laminate and (Right) $[(0,90)_2]_s$ cross-ply laminate

This sort of stacking sequence denies unexpected coupling effects in various applications, results in an in-plane stiffness that is independent of the composite's orientation.
Considering the equations and engineering constants mentioned above, ABD matrix can be calculated as:

$$\begin{Bmatrix} N_1 \\ N_2 \\ N_6 \\ M_1 \\ M_2 \\ M_6 \end{Bmatrix} = \begin{bmatrix} 42.15 & 14.25 & 0 & 0 & 0 & 0 \\ & 42.15 & 0 & 0 & 0 & 0 \\ \text{symmetric} & & 13.95 & 0 & 0 & 0 \\ 0 & 0 & 0 & 5.70 & 1.02 & -0.656 \\ 0 & 0 & 0 & & 1.65 & -0.656 \\ 0 & 0 & 0 & \text{symmetric} & & 1.00 \end{bmatrix} \begin{Bmatrix} \varepsilon_1^0 \\ \varepsilon_2^0 \\ \gamma_6^0 \\ \kappa_1 \\ \kappa_2 \\ \kappa_6 \end{Bmatrix}$$

The extensional stiffness matrix shows that the in-plane behavior of the laminate resembles the characteristic of the isotropic material, and the laminate is balanced as well ($A_{16} = A_{26} = 0$). The zero coupling stiffness matrix depicts that the considered laminate is balanced. Though the laminate is symmetric, D_{16} and D_{26} can not be zero. However, by stacking the layers alternatively at $+\theta$ and $-\theta$, it can only be minimized, especially if the layers number is large. Furthermore, despite showing the in-plane isotropic characteristics, the non-zero bending stiffness matrix confirms the QI behavior in the considered CL.

4.2.2 *Cross-ply laminate*

A laminate is called cross-ply laminate if all the plies used to fabricate the laminate are only 0° and 90°. Typical orientation of such laminate depicts in Figure 4.9.

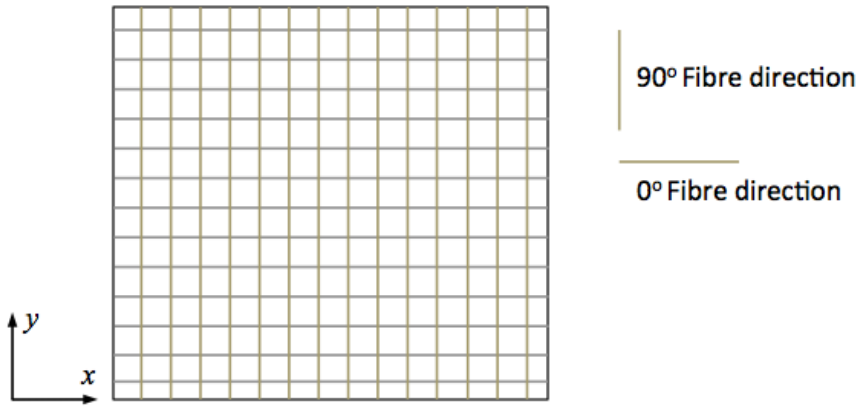

Fig. 4.9: Fibre orientation of $[(0,90)_2]_s$ cross-ply laminate

Figure 4.8 (Right) shows the stacking sequence of such laminate. For considered balanced laminate, ABD matrix can be determined as:

$$\begin{Bmatrix} N_1 \\ N_2 \\ N_6 \\ M_1 \\ M_2 \\ M_6 \end{Bmatrix} = \begin{bmatrix} 52.8 & 3.60 & 0 & 0 & 0 & 0 \\ & 52.8 & 0 & 0 & 0 & 0 \\ \text{symmetric} & & 3.30 & 0 & 0 & 0 \\ 0 & 0 & 0 & 5.75 & 0.182 & 0 \\ 0 & 0 & 0 & & 3.05 & 0 \\ 0 & 0 & 0 & \text{symmetric} & & 0.274 \end{bmatrix} \begin{Bmatrix} \varepsilon_1^0 \\ \varepsilon_2^0 \\ \gamma_6^0 \\ \kappa_1 \\ \kappa_2 \\ \kappa_6 \end{Bmatrix}$$

Among all components of $[A]$, and $[D]$, the zero value of A_{16}, A_{26}, D_{16}, and D_{26} proves that the laminate is cross-ply. $[B] = 0$ proves that the laminate is symmetric. It can also be seen that, for QI laminate, the A_{66} component has a relation with A_{11} and A_{12} component likewise the isotropic material, whereas in case of cross-ply laminate, A_{66} component does not show such characteristics.

5

DYNAMIC SHEAR STRAIN ANALYSIS

The method was so developed to detect the damage of specimens as a novel technique in the field of guided wave based NDT [90]. The potential of high frequency fundamental antisymmetric mode (A_0) of lamb wave is chosen in this evaluation. The technique considers the near-field imaging phenomena of surface displacement. Assuming that a known incident field impinges on the surface to be imaged and the scattered field is measured very close to it so that exponentially small, evanescent components of the waves are significant and can be measured. It should make sure that the measurements have to be made very close to the surface. These measurements are used in the inversion, consequently, the imaging resolution found much better than the wavelength of the incident field. The evaluation technique can be summarized in several steps: (a) After irradiating the lamb wave signal, obtained the time series data consisting vertical displacement of the surface, (b) measuring the shear strain at each point by means of filtering process from collected data (Orthogonal pair of the out-of surface shear strain exhibit linear characteristics in a flawless region, whereas at the region of defect, non-linearity arises due to the development of evanescent wave), (c) A covariance matrix is adopted composed of the vector of out-of-surface shear strains, (d) the determinant of the matrix reveal any value other than zero at all points within the region of developed evanescent waves. Thus the image of the boundary of the defect reconstructed. The analytical study of the technique for isotropic continuum discussed as follows:

The vertical displacement of the A_0 mode Lamb wave satisfies the two dimensional wave equation. Analyzing the near field of the scattering object, let consider the scattering wave field from the boundary of a cylindrical subsurface defect. The geometrical relation of the cylindrical subsurface defect and the incident plane wave is depicted in Fig. 5.1. The radius of the cylinder,

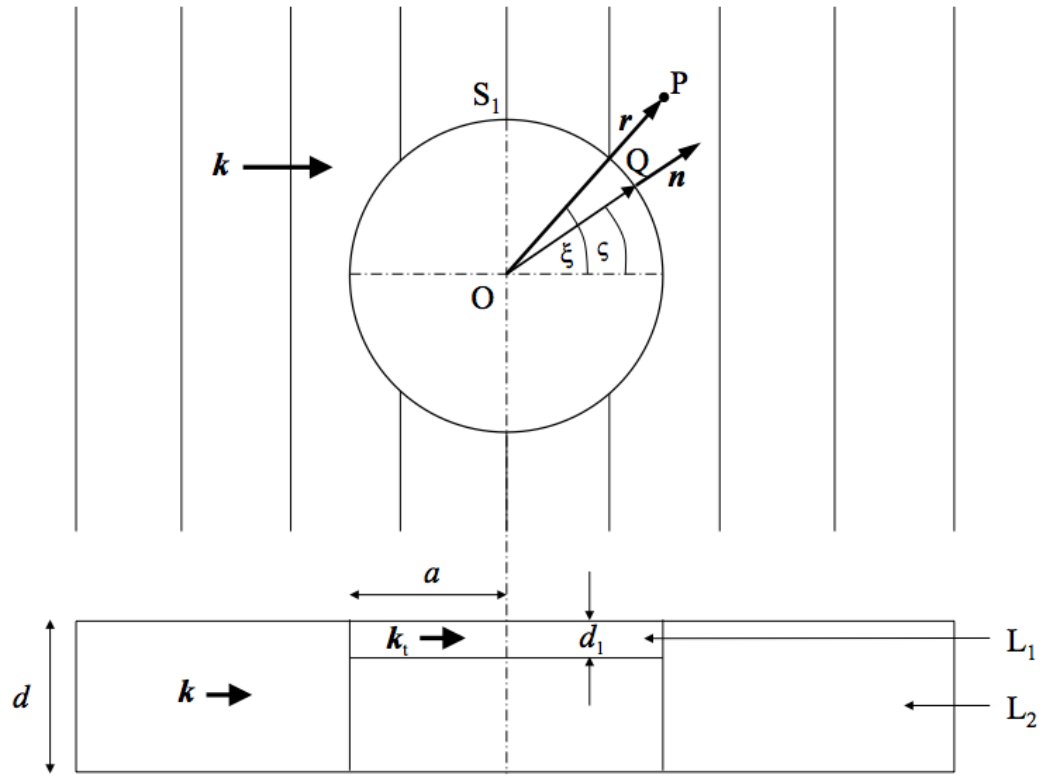

Fig. 5.1: Geometrical relation among the plane wave and the cylindrical defect

a, satisfies the following condition:

$$a \ll \frac{\lambda}{2\pi}$$

where, λ is the wavelength of the incident Lamb wave. The observation point P and the scattering point Q can be defined as

$$\overrightarrow{\mathrm{OP}} = \boldsymbol{r} = \begin{pmatrix} r\cos\xi \\ r\sin\xi \end{pmatrix},$$
$$\overrightarrow{\mathrm{OQ}} = \boldsymbol{a} = \begin{pmatrix} a\cos\zeta \\ a\sin\zeta \end{pmatrix}$$

The normal vector on Q, $\boldsymbol{n}$ and the wave vector, $\boldsymbol{k}$ can be denoted as:

$$\boldsymbol{n} = \begin{pmatrix} \cos\zeta \\ \sin\zeta \end{pmatrix},$$
$$\boldsymbol{k} = \begin{pmatrix} k \\ 0 \end{pmatrix} = \begin{pmatrix} \frac{2\pi}{\lambda} \\ 0 \end{pmatrix}$$

In the lowest frequency band, A_0-mode is the most dominant Lamb wave and its phase velocity decreases proportionally with the square root of the product of frequency and plate thickness. The dynamic out-of-plane displacement, excited by the incident plane wave, observed at P can be expressed as

$$f_i(\boldsymbol{r}, t) = \exp(i\boldsymbol{k}^{\mathrm{T}}\boldsymbol{r}) \exp(-i\omega t) \tag{5.1}$$

The steering term can be decomposed with *Neumann*'s series expansion as

$$\exp(i\boldsymbol{k}^{\mathrm{T}}\boldsymbol{r}) = J_0(kr) + 2\sum_{n=1}^{\infty} i^n J_n(kr)\cos(n\xi) \tag{5.2}$$

where $\boldsymbol{k}^{\mathrm{T}}$, J_n denote the transpose of the wave number vector, and n-th order *Bessel* function respectively. Focusing on the normal displacement of the top surface, the scattered wave field from the cylindrical boundary can be written in multiple expansion form, as:

$$f_s(\boldsymbol{r}, t) = \left(A_0 H_0^{(1)}(kr) + 2\sum_{n=1}^{\infty} A_n H_n^{(1)}(kr)\cos(n\xi)\right)\exp(-i\omega t) \tag{5.3}$$

where $H_n^{(1)}$ denotes the first kind n-th order *Hankel* function and the function is defined outside the cylinder, $r > a$. the incoming wave front on the top surface, can be denoted as

$$f_b(\boldsymbol{r}, t) = \left(B_0 J_0(k_t r) + 2\sum_{n=1}^{\infty} B_n J_n(k_t r)\cos(n\xi)\right)\exp(-i\omega t) \tag{5.4}$$

At the boundary of the defect, three A_0-mode Lamb waves satisfy the continuity of the normal displacement and derivatives across the boundary as follows:

$$f_i(\boldsymbol{a},t) + f_s(\boldsymbol{a},t) = f_b(\boldsymbol{a},t)$$
$$\nabla(f_i(\boldsymbol{a},t) + f_s(\boldsymbol{a},t))^{\mathrm{T}}\boldsymbol{n} = \nabla(f_b(\boldsymbol{a},t))^{\mathrm{T}}\boldsymbol{n}$$

Consequently, A_n and B_n can be defined as

$$A_n = -\frac{\frac{k_t}{k}-1}{\frac{k_t}{k}+1} i^n \frac{\frac{d}{da}J_n(ka)}{\frac{d}{da}H_n^{(1)}(ka)}$$
$$B_n = \frac{2}{\frac{k_t}{k}+1} i^n \frac{J_n(ka)}{J_n(k_t a)} \qquad (n = 1,2,.....)$$

Being that the circumference of the defect is much smaller than the wavelength, $2\pi a \ll \lambda$, the following approximation are satisfied [2]:

$$\begin{aligned}
J_0(ka) &\simeq 1 \\
J_0(ka) &\simeq \frac{1}{\Gamma(n+1)}\left(\frac{1}{2}ka\right)^2 \\
\frac{d}{da}H_0^{(1)}(ka) &= -kH_1^{(1)}(ka) \\
&\simeq -ik\frac{1}{\pi}\left(\frac{1}{2}ka\right)^{-1} \\
\frac{d}{da}H_n^{(1)}(ka) &= -kH_{n+1}^{(1)}(ka) + \frac{n}{a}H_n^{(1)}(ka) \\
&\simeq -i\frac{1}{a\pi}\Gamma(n+1)\left(\frac{1}{2}ka\right)^{-n} \\
\frac{d}{da}J_0(ka) &= -kJ_1(ka) \\
&\simeq -k\left(\frac{1}{2}ka\right) \\
\frac{d}{da}J_n(ka) &= kJ_{n-1}(ka) - \frac{n}{a}J_n(ka) \\
&\simeq \frac{1}{a}\frac{1}{\Gamma(n)}\left(\frac{1}{2}ka\right)^n
\end{aligned} \tag{5.5}$$

Here, Γ denotes the gamma function, if n is a positive integer: $\Gamma(n) = (n-1)!$. Based on the above limiting forms for small arguments, the outgoing scattered wave field can be approximated as [90]:

$$f_s(\boldsymbol{r},t) \simeq \frac{k_t - k}{k_t + k}\Big\{ -i\pi\Big(\frac{ka}{2}\Big)^2 H_0^{(1)}(kr) - 2\pi\Big(\frac{ka}{2}\Big)^2 H_1^{(1)}(kr)\cos\xi + 2\sum_{n=2}^{\infty} i^{n+1}\frac{\pi}{n\Gamma^2(n)}\Big(\frac{ka}{2}\Big)^{2n} H_n^{(1)}(kr)\cos(n\xi)\Big\}\exp(-i\omega t) \quad (5.6)$$

Thus an incoming wave field can be expressed as well, as [90]:

$$f_b(\boldsymbol{r},t) \simeq \frac{2k}{k_t + k}\Big(J_0(k_t r) + 2\sum_{n=1}^{\infty} i^n \frac{k^n}{k_t^n} J_n(k_t r)\cos(n\xi)\Big)\exp(-i\omega t) \quad (5.7)$$

Considering the first two dominant term of (5.6) and (5.7), the approximation of total wave field expression outside ($\|r\| > a$) and inside ($\|r\| \leq a$) the defect returns as:

$$\begin{aligned} \tilde{f}_{out}(\boldsymbol{r},t) &= f_i(\boldsymbol{r},t) + f_s(\boldsymbol{r},t) \\ &\simeq \Big[\exp(ikr\cos\xi) + \frac{k_t - k}{k_t + k}\Big\{ -i\pi\Big(\frac{ka}{2}\Big)^2 H_0^{(1)}(kr)\Big\} \\ &\quad - 2\pi\Big(\frac{ka}{2}\Big)^2 H_1^{(1)}(kr)\cos\xi\Big]\exp(-i\omega t) \end{aligned} \quad (5.8)$$

$$\begin{aligned} \tilde{f}_{in}(\boldsymbol{r},t) &= f_b(\boldsymbol{r},t) \\ &\simeq \frac{2k}{k_t + k}\Big(J_0(k_t r) + 2i\frac{k}{k_t}J_1(k_t r)\cos\xi\Big)\exp(-i\omega t) \end{aligned} \quad (5.9)$$

The orthogonal pair of the dynamic out-of-plane shear strains is given by the gradient of the total wave field outside of the defect as follows:

$$\nabla\tilde{f}_{out} = \begin{pmatrix} \frac{\partial\tilde{f}_{out}(\boldsymbol{r},t)}{\partial r} \\ \frac{1}{r}\frac{\partial\tilde{f}_{out}(\boldsymbol{r},t)}{\partial\xi} \end{pmatrix} \quad (5.10)$$

where,

$$\begin{aligned} \frac{\partial\tilde{f}_{out}(\boldsymbol{r},t)}{\partial r} &= \Big(\frac{k_t - k}{k_t + k}\Big)\Big[ik\cos\xi\exp(ikr\cos\xi) + ik\pi\Big(\frac{ka}{2}\Big)^2 H_1^{(1)}(kr) \\ &\quad + 2\pi\Big(\frac{ka}{2}\Big)^2\{-kH_2^{(1)}(kr) + \frac{1}{r}H_1^{(1)}(kr)\}\cos\xi\Big]\exp(-i\omega t) \end{aligned} \quad (5.11)$$

$$\frac{1}{r}\frac{\partial \tilde{f}_{out}(\boldsymbol{r},t)}{\partial \xi} = \Big(\frac{k_t - k}{k_t + k}\Big)\Big[\sin\xi\Big\{ - ik\exp(ikr\cos\xi) + 2\pi\Big(\frac{ka}{2}\Big)^2\frac{1}{r}H_1^{(1)}(kr)\Big\}\Big]\exp(-i\omega t) \tag{5.12}$$

Reducing the disturbance caused by the noise and fluctuations of the signal intensity, the covariance matrix of the dynamic out-of-plane shear strains is adopted as:

$$\begin{aligned}\mathbb{R} &= \begin{pmatrix} R_{rr} & R_{r\xi} \\ R^*_{r\xi} & R_{\xi\xi} \end{pmatrix} \\ &= \lim_{T\to\infty}\frac{1}{T}\int_0^T (\nabla\tilde{f}(\boldsymbol{r},t)\nabla^{\mathrm{T}}\tilde{f}^*(\boldsymbol{r},t))dt\end{aligned} \tag{5.13}$$

where $R^*_{r\xi}$ is the complex conjugate of $R_{r\xi}$. The first component of the matrix can be written as follows:

$$\begin{aligned}R_{rr} &= \lim_{T\to\infty}\frac{1}{T}\int_0^T \frac{\partial f_i(\boldsymbol{r},t)}{\partial r}\frac{\partial f_i^*(\boldsymbol{r},t)}{\partial r}dt \\ &+ \lim_{T\to\infty}\frac{1}{T}\int_0^T \frac{\partial f_s(\boldsymbol{r},t)}{\partial r}\frac{\partial f_s^*(\boldsymbol{r},t)}{\partial r}dt \\ &+ \lim_{T\to\infty}\frac{1}{T}\int_0^T \frac{\partial f_i(\boldsymbol{r},t)}{\partial r}\frac{\partial f_s^*(\boldsymbol{r},t)}{\partial r}dt \\ &+ \lim_{T\to\infty}\frac{1}{T}\int_0^T \frac{\partial f_s(\boldsymbol{r},t)}{\partial r}\frac{\partial f_i^*(\boldsymbol{r},t)}{\partial r}dt\end{aligned} \tag{5.14}$$

However, the terms of mutual correlation of the incident and scattered wave field are reduced to be zero. This is because the scattered wave field is out of phase with the incident wave field except than on the rim of the cylindrical defect. With this consideration, R_{rr} reduces to:

$$\begin{aligned}R_{rr} &= \lim_{T\to\infty}\frac{1}{T}\int_0^T \frac{\partial f_i(\boldsymbol{r},t)}{\partial r}\frac{\partial f_i^*(\boldsymbol{r},t)}{\partial r}dt \\ &+ \lim_{T\to\infty}\frac{1}{T}\int_0^T \frac{\partial f_s(\boldsymbol{r},t)}{\partial r}\frac{\partial f_s^*(\boldsymbol{r},t)}{\partial r}dt \\ &\simeq k^2\cos^2\xi + \Big(\frac{k_t - k}{k_t + k}\Big)^2\Big(\frac{2\pi}{r}\Big)^2\Big(\frac{ka}{2}\Big)^4 \\ &\cdot\Big[\Big\{\Big(\frac{ikr}{2}\Big)^2 - ikr\cos\xi + \cos^2\xi\Big\}\Big|H_1^{(1)}(kr)\Big|^2 \\ &+ ik^2r^2H_1^{(1)}(kr)\overline{H}_2^{(1)}(kr) - 2kr\cos\xi\overline{H}_1^{(1)}(kr)H_2^{(1)}(kr) + (kr)^2\Big|H_2^{(1)}(kr)\Big|^2\Big]\end{aligned} \tag{5.15}$$

Other components are given in the same way

$$
\begin{aligned}
R_{r\xi} &= \frac{1}{r}\lim_{T\to\infty}\frac{1}{T}\int_0^T \frac{\partial f_i(\boldsymbol{r},t)}{\partial r}\frac{\partial f_i^*(\boldsymbol{r},t)}{\partial \xi}dt \\
&\quad + \frac{1}{r}\lim_{T\to\infty}\frac{1}{T}\int_0^T \frac{\partial f_s(\boldsymbol{r},t)}{\partial r}\frac{\partial f_s^*(\boldsymbol{r},t)}{\partial \xi}dt \\
&\simeq -k^2\cos\xi\sin\xi + \Big(\frac{k_t-k}{k_t+k}\Big)^2\Big(\frac{2\pi}{r}\Big)^2\Big(\frac{ka}{2}\Big)^4\sin\xi \\
&\quad \cdot\Big[\Big(\frac{ikr}{2}-\cos\xi\Big)\Big|H_1^{(1)}(kr)\Big|^2 + kr\overline{H}_1^{(1)}(kr)H_2^{(1)}(kr)\Big]
\end{aligned}
\tag{5.16}
$$

$$
\begin{aligned}
R_{\xi\xi} &= \frac{1}{r^2}\lim_{T\to\infty}\frac{1}{T}\int_0^T \frac{\partial f_i(\boldsymbol{r},t)}{\partial \xi}\frac{\partial f_i^*(\boldsymbol{r},t)}{\partial \xi}dt \\
&\quad + \frac{1}{r^2}\lim_{T\to\infty}\frac{1}{T}\int_0^T \frac{\partial f_s(\boldsymbol{r},t)}{\partial \xi}\frac{\partial f_s^*(\boldsymbol{r},t)}{\partial \xi}dt \\
&\simeq k^2\sin^2\xi \\
&\quad + \Big(\frac{k_t-k}{k_t+k}\Big)^2\Big(\frac{2\pi}{r}\Big)^2\Big(\frac{ka}{2}\Big)^4\Big[\sin^2\xi\Big|H_1^{(1)}(kr)\Big|^2\Big]
\end{aligned}
\tag{5.17}
$$

Therefore, when ($\|r\| > a$), the determinant of the $\mathbb{R}$ becomes:

$$
\begin{aligned}
|\mathbb{R}| &= R_{rr}R_{\xi\xi} - R_{r\xi}R_{r\xi}^* \\
&\simeq \Big(\frac{k_t-k}{k_t+k}\Big)^2\Big(\frac{2\pi}{r}\Big)^2\Big(\frac{ka}{2}\Big)^4\sin^2\xi\Big[k^2\Big[\Big\{\Big(\frac{ikr}{2}\Big)^2 - ikr\cos\xi+\cos^2\xi\Big\}\Big|H_1^{(1)}(kr)\Big|^2 \\
&\quad + ik^2r^2H_1^{(1)}(kr)\overline{H}_2^{(1)}(kr) - 2kr\cos\xi\overline{H}_1^{(1)}(kr)H_2^{(1)}(kr) + (kr)^2\Big|H_2^{(1)}(kr)\Big|^2\Big] \\
&\quad + k^2\cos^2\xi\Big|H_1^{(1)}(kr)\Big|^2 + \Big(\frac{k_t-k}{k_t+k}\Big)^2\Big(\frac{2\pi}{r}\Big)^2\Big(\frac{ka}{2}\Big)^4\Big|H_1^{(1)}(kr)\Big|^2 \\
&\quad \cdot\Big[\Big\{\Big(\frac{ikr}{2}\Big)^2 - ikr\cos\xi+\cos^2\xi\Big\}\Big|H_1^{(1)}(kr)\Big|^2 \\
&\quad + ik^2r^2H_1^{(1)}(kr)\overline{H}_2^{(1)}(kr) - 2kr\cos\xi\overline{H}_1^{(1)}(kr)H_2^{(1)}(kr) + (kr)^2\Big|H_2^{(1)}(kr)\Big|^2\Big] \\
&\quad - 2k^2\cos\xi\Big[\Big(\frac{ikr}{2}+\cos\xi\Big)\Big|H_1^{(1)}(kr)\Big|^2\Big] \\
&\quad - k^2\cos\xi(kr)\Big\{H_1^{(1)}(kr)\overline{H}_2^{(1)}(kr) + \overline{H}_1^{(1)}(kr)H_2^{(1)}(kr)\Big\} \\
&\quad + \Big(\frac{k_t-k}{k_t+k}\Big)^2\Big(\frac{2\pi}{r}\Big)^2\Big(\frac{ka}{2}\Big)^4\Big[\Big\{\Big(\frac{ikr}{2}-\cos\xi\Big)\Big|H_1^{(1)}(kr)\Big|^2 + kr\overline{H}_1^{(1)}(kr)H_2^{(1)}(kr)\Big\} \\
&\quad \Big\{\Big(\frac{ikr}{2}-\cos\xi\Big)\Big|H_1^{(1)}(kr)\Big|^2 + krH_1^{(1)}(kr)\overline{H}_2^{(1)}(kr)\Big\}\Big]\Big]
\end{aligned}
\tag{5.18}
$$

On the basis of the above discussion, the determinant of the covariance matrix, $|\mathbb{R}|$, possesses following characteristics:

- $|\mathbb{R}| > 0$, when the scattered wave fronts propagate along the any different direction of the incident wave front.
- $|\mathbb{R}|$ concentrates its own energy within the near-field of the surrounding of the boundary of the cylindrical defect.

Therefore, the distribution of $|\mathbb{R}|$ is utilized for the near-field imaging of defects. On the contrary, inside the defected region, each component of $\mathbb{R}$ can be approximated as:

$$
\begin{aligned}
R_{rr} &= \lim_{T\to\infty}\frac{1}{T}\int_0^T \frac{\partial f_b(\boldsymbol{r},t)}{\partial r}\frac{\partial f_b^*(\boldsymbol{r},t)}{\partial r}dt \\
&\simeq \Big(\frac{2k}{k+k_t}\Big)^2.\Big[J_1(k_t r)^2 k_1^2 + \Big\{\frac{J_1(k_t r)}{k_t r} - J_2(k_t r)\Big\}^2 \cos^2\xi k^2\Big] \\
R_{r\xi} &= \frac{1}{r}\lim_{T\to\infty}\frac{1}{T}\int_0^T \frac{\partial f_b(\boldsymbol{r},t)}{\partial r}\frac{\partial f_b^*(\boldsymbol{r},t)}{\partial \xi}dt \\
&\simeq -\frac{2}{r}\Big(\frac{2k}{k+k_t}\Big)^2\Big[\Big\{\frac{2k}{k_t}\frac{J_1(k_t r)}{k_t r} - J_2(k_t r)\Big\}J_1(k_t r)k\cos\xi\sin\xi - iJ_1(k_t r)k\sin\xi\Big] \\
R_{\xi\xi} &= \frac{1}{r^2}\lim_{T\to\infty}\frac{1}{T}\int_0^T \frac{\partial f_b(\boldsymbol{r},t)}{\partial \xi}\frac{\partial f_b^*(\boldsymbol{r},t)}{\partial \xi}dt \\
&\simeq 4\Big(\frac{2k}{k+k_t}\Big)^2\Big(\frac{k}{k_t r}\Big)^2 J_1^2(k_t r)\sin^2\xi
\end{aligned}
$$

Thus in approaching to the center of the cylinder ($\|r\| \leq a$), the determinant of $\mathbb{R}$ is reduced to be negligible.

Working principle of the technique can be summarized as when a plane wave strikes at the boundary of the defect, it scattered in its way. The scattered wave overlaps with the incident wave and develop evanescent wave. Such type of wave conserved its energy at the center of the development region and attenuated accordingly. The orthogonal pair of out-of-plane shear strain at that point violate the linearity. The determinant of the adopted covariance matrix becomes more significant than zero at that point. Each location of violation of linearity thus detected which eventually forms the shape of the defect boundary and consequently, the image is reconstructed.

In this study, the well established above mentioned damage detection technique applied in CFRP material. The algorithm remains the same though the

strategy is quite different by the plane wave propagation as the phase and group velocity direction is the no longer same way. Rather than the development of an analytical model, we examine the procedure numerically to investigate its effectiveness in unidirectional, bidirectional and quasi-isotropic CL.

6

NUMERICAL EXPERIMENTS

The chapter mainly discussed computer generated investigations based on the mathematical formulation of the previous chapter. The investigation presents the application of dynamic shear strain analysis to detect finite subsurface defect in CFRP laminate, composed with HTI and orthotropic material focusing on unidirectional, cross-ply, and quasi-isotropic fibre orientation laminate. Analytical data obtained by using the multiphysics simulation software package LS-DYNA. At the beginning, we are going to discuss the FEM generation of the 3D geometry of the specimen and extracted data analysis technique toward applying the damage detection technique. To coop with the software package, in this chapter, cartesian coordinate is denoted by x, y, z instead.

6.1 FINITE ELEMENT MODEL

3D FE method is employed to simulate the Lamb wave propagation, scattering and transmitting at a subsurface cylindrical hole of composite laminates. The multiphysics software package LS-DYNA is used to generate the geometry, perform the meshing of the model and numerical simulations. CL consisting of 8-ply unidirectional carbon/epoxy laminate but with different stacking sequences are considered. Density of each lamina is $1500\,\mathrm{kg/m^3}$. The dimension of the FE models is $6\,\mathrm{mm} \times 6\,\mathrm{mm} \times 1\,\mathrm{mm}$. For a flawless laminate, each lamina is modeled using eight-noded 3D reduced integration solid brick elements and shown in Fig.6.1. Vertical (z) directional degree of freedom (DoF) allowed to the nodes. The zero-strain condition is considered in all planes for designing a flawless anisotropic (HTI to be more specific) specimen. The theoretically calculated wavelengths for 0° to 90° fiber direc-

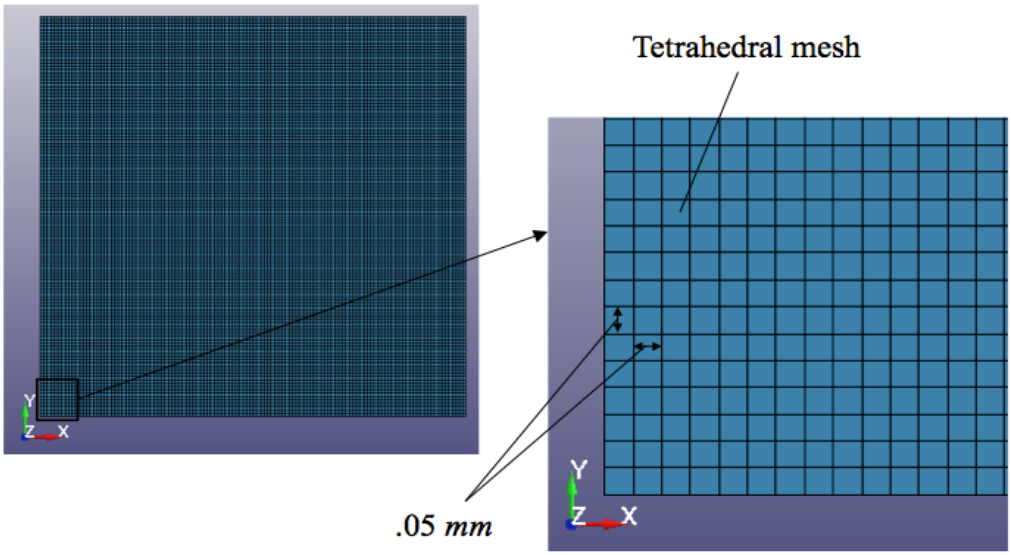

Fig. 6.1: 3D model plate meshing in flawless region

tion are between 7.36 mm to 5.66 mm. A very fine mesh of having in-plane square shape with dimensions .05 mm $\times$ .05 mm is used for the entire model, which guarantees that more than 17 nodes exist per wavelength in any propagation direction in any laminate which satisfy the literature [7, 57, 65]. The thickness of each layer is 0.125 mm and 8 layers give an overall 1 mm of thickness. The time step is automatically controlled, depending on the smallest element size, which is sufficient to capture any A_0-mode Lamb wave propagation. For each lamina, fiber direction is set carefully and the enlarged view in Fig. 6.2 shows the fiber direction for 0° lamina.

The A_0-mode Lamb wave signals are obtained by monitoring the out-of-plane nodal displacement of the nodes located at the surface of the laminate. Allowing normal directional DoF ensures that only the A_0-mode is detected as the SH_0-modes have zero out-of-plane displacements at the surface. To investigate the anisotropic behavior of the considered 3D model, a sample run is carried out in a 0° fiber directional flawless laminate ($[0]_8$) allowing the wave propagation from a point source of 0.75 mm transducer area with a frequency of 30 kHz. Contours of normal displacement of the particles taken into account and Fig.6.3 illustrates that the wave frontal profile follows the information given in stiffness matrix (equation 4.1). a cylindrical subsurface hole located at the center of the laminate is created by removing FE elements

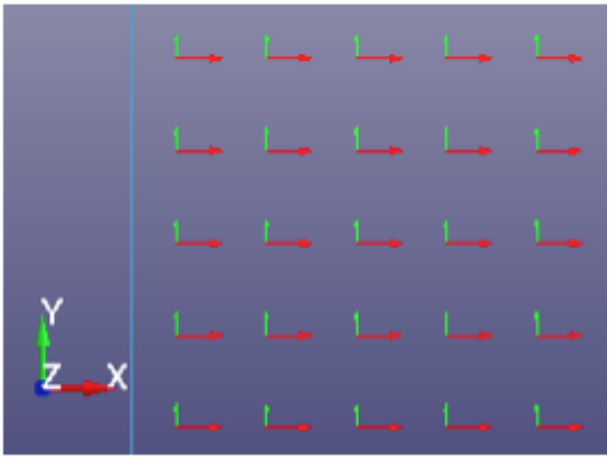

Fig. 6.2: Fiber direction (red arrow) along the horizontal axis, blue vertical line indicates the model boundary

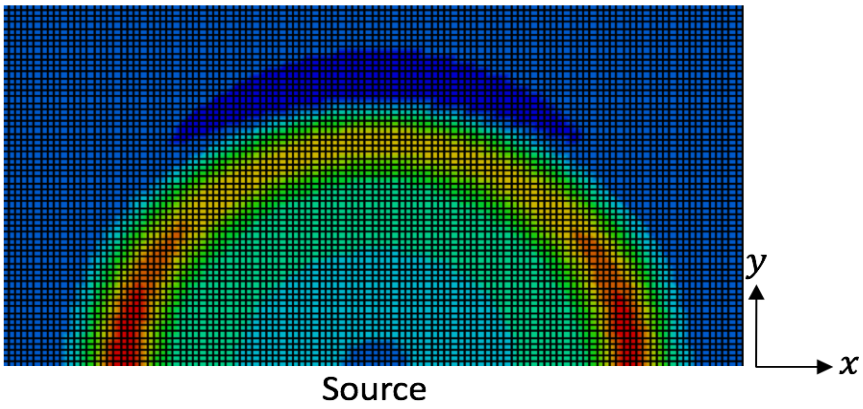

Fig. 6.3: Wave propagation in HTI model at 20 μs after irradiation (x axis indicates the fibre direction)

to generate a defected plate. Surround the flaw; the lamina is modeled using the combination of hexahedral and triangular elements and shown in Fig.6.4. Figure 6.5 shows the zoomed view of the eight-layered FE model with cylindrical defect. The A_0-mode Lamb wave is excited by applying out-of-plane nodal displacement to the surface nodes of 6 mm $\times$ 1 mm transducer area at the **L** end of the model (Fig.6.6) and the wave assumed to be propagate along x direction of the geometry.

The excitation signal is a 30 kHz mono-cycle sinusoidal tone burst. All planes of the object including the defected region satisfy the stress-free conditions except the source plane. Wave propagation at different state in $[0]_8$

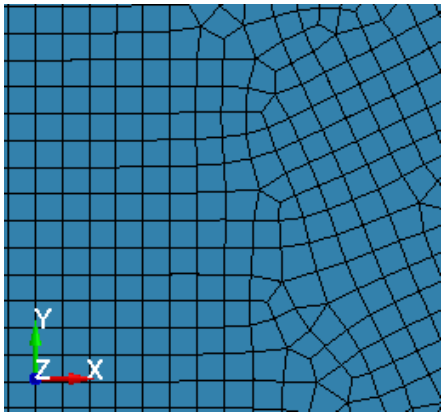

Fig. 6.4: Meshing of the 3D model surround the defect

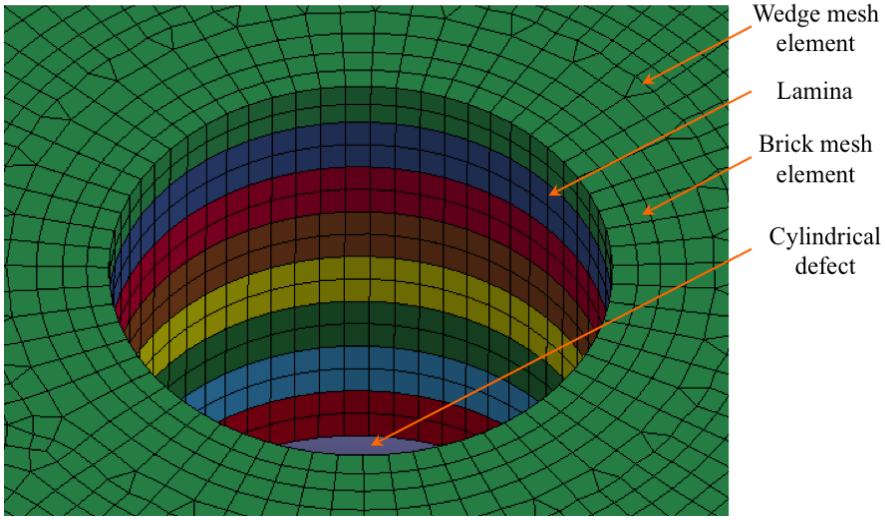

Fig. 6.5: 3D FE zoomed in model at the cylindrical hole defected region

is depicted in Fig.6.7. The normal displacement of the top surface particles continuously monitored from the very beginning of the irradiation till the end at a specified time interval.

Wave propagation along the x-coordinate in Fig.6.7 illustrates that in the flawless region, each point exhibits same out-of-plane displacement. At the boundary of the defect, the incident wave faces the obstacle and reflected back and transmitted as well over the defected region. The absorbing surface criteria is chosen at the **R** end and it takes 14 μs to reach the boundary from the source plane.

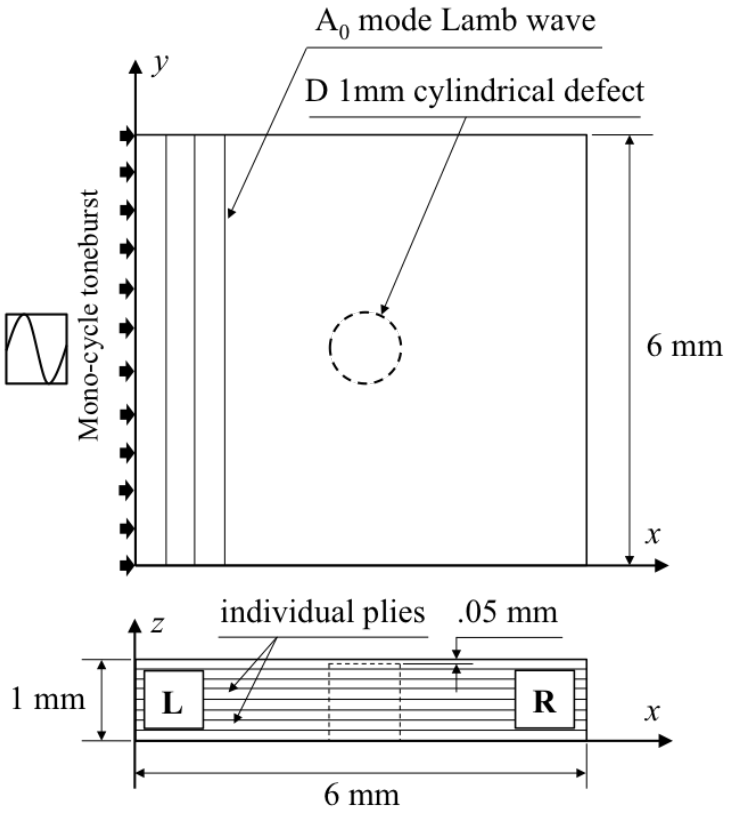

Fig. 6.6: Geometrical specifications and schematic diagram of the configuration for FE simulations

6.2 INTERACTION OF A_0-MODE LAMB WAVE WITH SUBSURFACE DEFECT

Reflection and transmission at defect

The reflection and transmission of the A_0-mode Lamb wave at the defect are studied in this section. The FE model described in the previous section was used to simulate the $[0]_8$, $[30]_8$, $[60]_8$, and $[90]_8$ laminate with a 1 mm diameter subsurface defect. As the damage detection technique stated in this thesis working with the overlapped wave in the vicinity of the damage, a number of measurements were taken at r $= 0.5$ mm and $140^\circ \leq \theta \leq 220^\circ$ with 10° interval to obtain the reflection wave from the defect. In contrast, at the r $= 0.5$ mm and $0^\circ \leq \theta \leq 30^\circ$ and $330^\circ \leq \theta \leq 350^\circ$with 10° interval, transmission wave were measured. Figure6.8 shows the maximum amplitude of the reflected and transmitted waves from the defect, respectively, where

the amplitudes of the reflected and transmitted waves are normalized by the maximum amplitude measured on the surface at that instant. As shown in the figure, $[0]_8$ laminate shows the maximum whereas $[90]_8$ laminate shows the maximum amplitude of the reflected wave and the variation is symmetric along the axis passing through the center of the defect. On the other hand, it is also depicted that $[60]_8$ and $[90]_8$laminate shows the negative amplitude in case of the transmitted wave and in both case the $[30]_8$ and $[60]_8$ laminate shows that the amplitude pattern is not symmetric.

Amplitude comparison at the defect boundary

This section employs the validated FE model to study the A_0-mode Lamb wave reflected characteristics at defect with different directional laminate using the overlapped wave amplitude. The excitation is at the left boundary of the model and $\theta = 180^\circ$ according to the coordinate system. The out-of-plane displacement of 36 nodal points located at r $= 0.5$ mm and $0^\circ \leq \theta \leq 360^\circ$ with 10° step increments were monitored. On the boundary of the defect, the scattered wave overlapped with the incident wave and the condition of linearity violated. This distance fulfills the near-field requirement thus the evanescent waves can be achieved. For each case, two simulations were carried out with the same meshing for the intact and defected plate, and the results are compared after 14 μs of the excitation. The out-of-plane displacement at the measurement points is normalized by the maximum displacement on the surface at that time. Figure 6.9 and 6.10 shows the reflected wave pattern in a defected plate and flow pattern in the flawless plate and compared utilizing the out-of-plane displacement at the measurement points. It should be stated that the out-of-plane displacement is normalized by the maximum displacement measured on the surface at that instant and the negative amplitude is considered as zero. It can be seen that the fiber direction of each laminate affect the wave propagation. The phenomena is too certain that the backward reflection is larger than the forward reflection. Starting from the 0° fiber direction, with the increase of angle, the forward reflection amplitude becomes smaller and in case of $[60]_8$ and $[90]_8$ laminate, it becomes negative (zero considered in this study). Furthermore, the flow pattern and reflected

amplitude follows the almost symmetric pattern for $[0]_8$ and $[90]_8$ laminate, based on the axis passing through the defect and differ for another couple of unidirectional fiber laminate. Moreover for $[30]_8$ and $[60]_8$ laminate, reflected amplitude of the flawless plate is always smaller than the defected plate. In contrast, for $[0]_8$ and $[90]_8$ laminate, the forward reflected amplitude of the flawless plate is larger than the defected plate. This property of $[0]_8$ and $[90]_8$ laminate dominates in the $[(0,90)_2]_s$ laminate and the Fig. 6.10(b) clearly depicts the nature of reflection for cross-ply laminate. As the QI ($[0,\pm 45,90]_s$) laminate composed on 4-layers of angular directional fiber ply, this follows the nature of $[0]_8$ and $[90]_8$ laminate (Fig. 6.10(c)). The overall reflected amplitude pattern of $[(0,90)_2]_s$ laminate is showing more symmetric behavior than $[0]_8$ and $[90]_8$ laminate. It can be concluded that, in every case, the reflected amplitude in the defected laminate is quite noticeable from the flow pattern in the flawless laminate.

Directivity Pattern of Scattered Wave

Now we are interested in quantitative analysis of the scattered normal displacement in the vicinity of the defected region for unidirectional, bi-directional and QI laminate by means of plotting the Directivity Pattern (DP). For DP studies, the additional out-of-plane displacement due to interaction between the incident wave and the defect is extracted by using the baseline subtraction technique. The subtraction can be achieved by carrying out two simulations with the same meshing for the intact and defected laminate. The out-of-plane displacement of the scattered wave $u_z^S(x,t)$ is evaluated by

$$u_z^S(x,y,t) = u_z^T(x,y,t) - u_z^I(x,y,t) \tag{6.1}$$

where $u_z^T(x,y,t)$ and $u_z^I(x,y,t)$ are the out-of-plane displacement components at measuring points of a certain time, or the defected and intact laminates, respectively. The pattern is constructed by determining the absolute normalized amplitude of the scattered wave. Figures 6.11 and 6.12 show the SDP of the 30 kHz incident wave at the 1 mm diameter circular subsurface defect. All scattering amplitudes are normalized by the maximum absolute

amplitude of the incident wave at the defect center location of the intact laminate [66].

DP for each laminate on the boundary of the defect indicates that there is a definite variation in amplitude almost in every angle. The zero value in Fig. 6.11(a) quite understandable as in those points, both of the values nullify each other which is also illustrated in Fig. 6.9(a). Another point of interest to be noted, the DP is not symmetric with respect to the 0° direction for the symmetric subsurface defect although it looked like symmetry in Fig. 6.9(a). This phenomena is another differentiable criteria of anisotropic material from the isotropic as in case of isotropic material the scattering DP is perfectly symmetric [18, 32]. This characteristic indicates that the DP of composite laminates is more complicated than that in the isotropic material. Figure 6.11, 6.12 shows that with the same geometrical configuration of the subsurface defect, the scattering characteristics are dependent on the fiber direction and the maximum amplitude is found in Fig. 6.11(b) and 6.11(c), i.e. for $[30]_8$ and $[60]_8$ laminate. These characteristics of scattering at the boundary of the defect will leave the footprints in the reconstructed image described in this thesis, discussed in the later sections.

6.3 DATA ANALYSIS

The A_0-mode Lamb wave propagation characteristics are described in the previous section. In case of every laminates, the time series based out-of-plane displacement data on the top surface is recorded for implementing the damage detection technique. The analysis is first implemented for a flawless plate. Figure (6.13) illustrates the time-dependent out-of-plane displacement distribution for $[0]_8$ flawless laminate. From this time series data, the shear strain of every point is measured against the orthogonal spatial coordinate. The orthogonal pair of out-of-plane shear strains are calculated by *Sobel* filter. The *Sobel* operator performs a 2D spatial gradient measurement on an image. The filter is well known for edge detection. This filtering technique utilizes

two 5×5 kernels: one estimates the gradient in the x-direction, while the other estimates that in the y-direction and formulated by:

$$\begin{aligned} f_x(x,y,t) &= \sum_{\varepsilon=-2}^{2} \sum_{\varrho=-2}^{2} Sobel_x^{5\times5}(\varepsilon,\varrho) \\ &\quad .f(x-\varepsilon\Delta x, y-\varrho\Delta y, t) \\ f_y(x,y,t) &= \sum_{\varepsilon=-2}^{2} \sum_{\varrho=-2}^{2} Sobel_y^{5\times5}(\varepsilon,\varrho) \\ &\quad .f(x-\varepsilon\Delta x, y-\varrho\Delta y, t) \end{aligned} \tag{6.2}$$

Schematic of *Sobel* filtering process can be shown in Fig. 6.14. The analysis concluded with the findings of each component of the covariance matrix using the following summation of the decaying series

$$\begin{aligned} R_{xx} &= \frac{1}{N\Delta t} \sum_{n=0}^{N} \kappa^n . f_x(x,y,(N-n)\Delta t) \\ &\quad .f_x(x,y,(N-n)\Delta t)\Delta t \\ R_{xy} &= \frac{1}{N\Delta t} \sum_{n=0}^{N} \kappa^n . f_x(x,y,(N-n)\Delta t) \\ &\quad .f_y(x,y,(N-n)\Delta t)\Delta t \\ R_{yy} &= \frac{1}{N\Delta t} \sum_{n=0}^{N} \kappa^n . f_y(x,y,(N-n)\Delta t) \\ &\quad .f_y(x,y,(N-n)\Delta t)\Delta t \end{aligned} \tag{6.3}$$

Where κ satisfies the following relation:

$$\kappa = \exp^{-\Delta t/\gamma}$$

The time-constant, γ, should be much longer than the period of the incident wave as this value controls the integral duration. According to the concept, for a flawless specimen, the determinant of the covariance matrix becomes zero everywhere on the top surface corresponding to its out-of-plane displacement distribution (Fig.6.15).

The fundamental antisymmetric mode lamb wave allowed to propagate from left to right of the model. The functionality of the entire damage detection technique discussed in the later sections.

6.4 EXPERIMENTAL RESULTS AND DISCUSSION

Numerical experiments conducted to assess the performance of the dynamic shear strain analysis of lamb wave field in the subsurface defected composite plate in focusing the detection of damage. Several experiments have been carried out for several cases one after another depending on the fiber direction. Figure 6.16-6.19 illustrates the overall flaw detection technique for unidirectional laminate. Though the signal with identical criteria allowed to irradiate from the left vertical surface, normal displacement distribution indicates that the wave propagation affects by the fibre direction. After impinging the incident wave field on the boundary of the defect, the scattered wave motion thus impact in the same fashion. The development of evanescent wave following the overlapping of the incident and scattered wave varies with each other. Each case the determinant of the adopted covariance matrix trace the evanescent waves quite satisfactorily. In the first case, the most perfect image reconstructed among all other cases. In other cases, the interaction between the incident wave and the defect is more substantial than the first instance and much more energy releases at the boundary of the defected region. The evanescent wave thus cover a bit more area. Nevertheless, in each case the reconstructed image reveals the shape of the subsurface defect. The zero-valued all other regions than the defect boundary indicates that, the determinant of the covariance matrix working satisfactorily in detecting the fault. Hence the dynamic shear strain analysis can trace the subsurface damage in unidirectional CFRP laminate independent of the fibre direction.

To coop with the practical applications, an experiment is carried out for cross-ply ($[(0,90)_2]_s$) laminate. The wave is assumed to propagate in the fibre direction of the top layer. Figure 6.20 illustrates the particles vertical displacement and outcome of application of dynamic shear strain analysis.

In the QI $[0,\pm 45,90]_s$ case, A_0-mode lamb wave assumed to be propagate in the fibre direction of top layer. Figure 6.21 illustrates the particles vertical

displacement and outcome of application of dynamic shear strain analysis. From the observation of the reconstructed image of the defect for cross-ply and QI laminate, it can be said that, the dynamic shear strain analysis can effectively and efficiently trace the evanescent wave field.

Thus this novel technique can detect the subsurface defect in unidirectional, cross-ply and QI CFRP laminate.

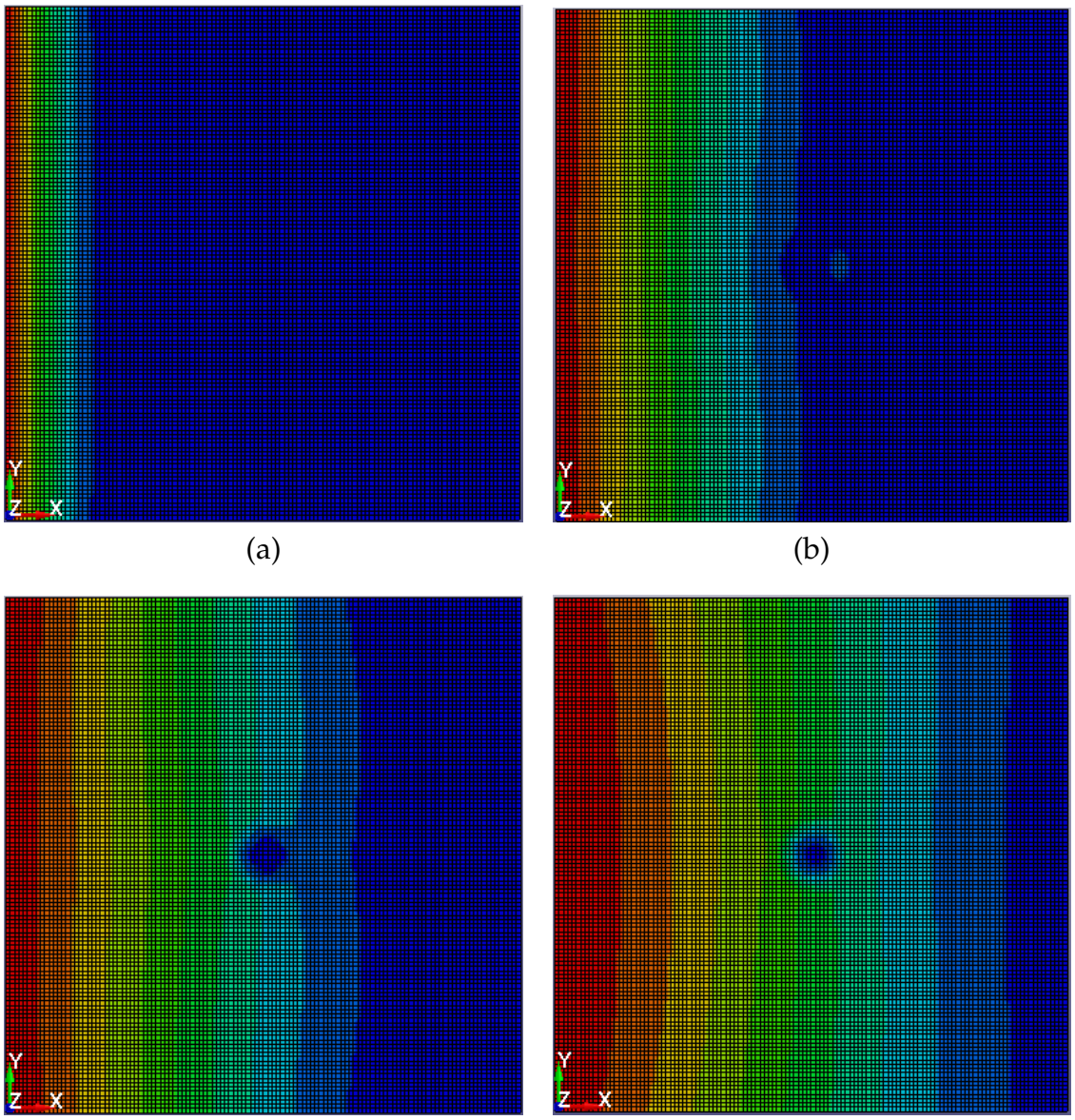

Fig. 6.7: Typical contour snapshots of FE simulated out-of-plane displacement for the $[0]_8$ laminate at different time instances, (a) soon after excitement at 3 μs, (b) just after A_0-mode Lamb wave interaction with a 1 mm diameter circular subsurface defect at 7 μs, (c) wave after leaving the defected zone at 11 μs, and (d) wavefront just before arriving on the boundary at 14 μs.

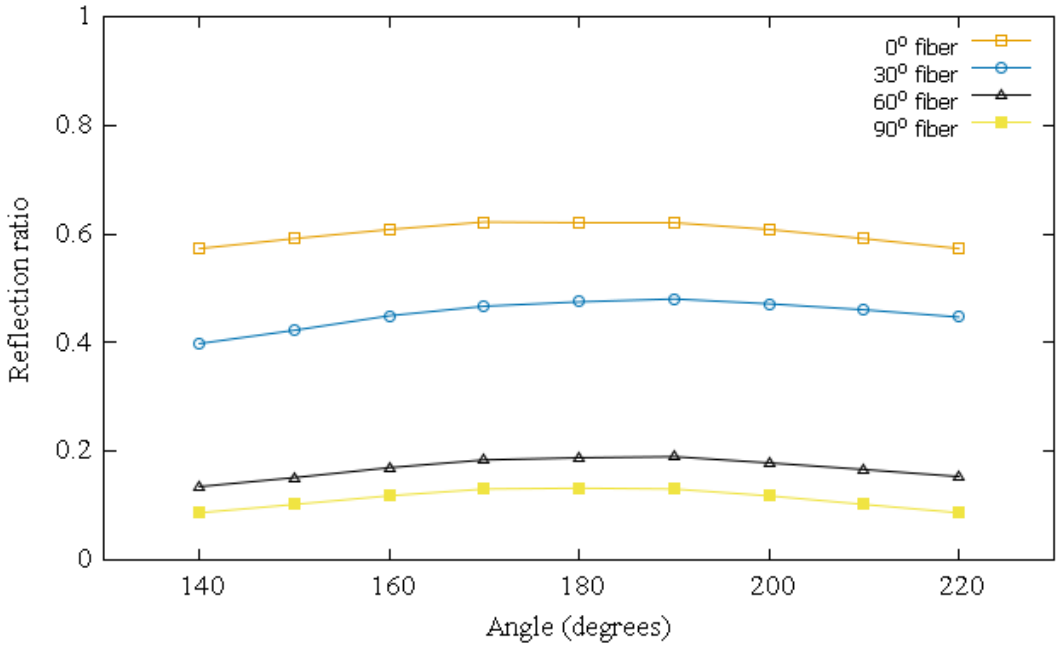

(a)

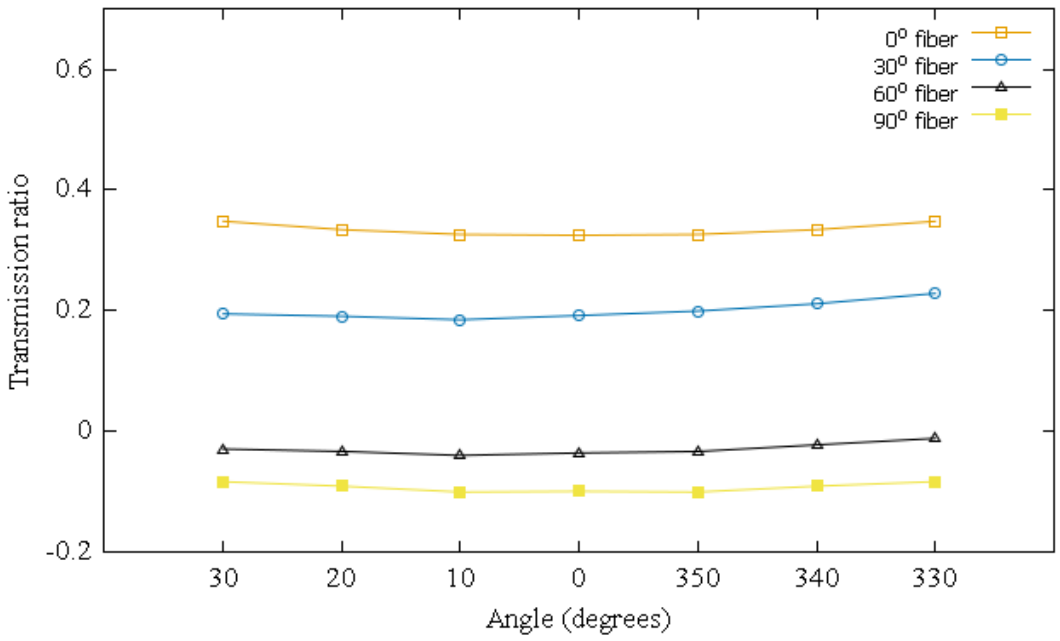

(b)

Fig. 6.8: Normalized amplitude of the (a) reflected and (b) transmitted waves from a 1 mm diameter circular subsurface defect as a function of θ by 30 kHz incident wave.

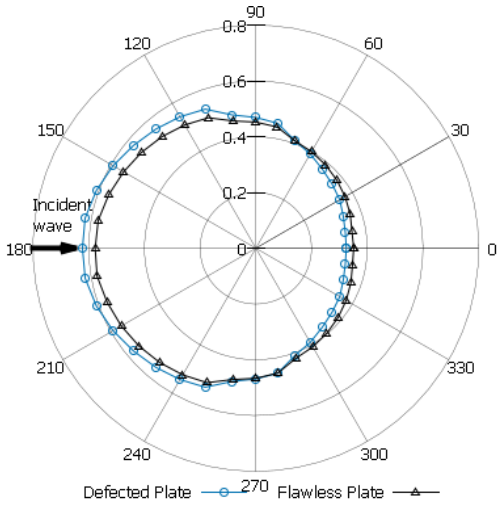

(a)

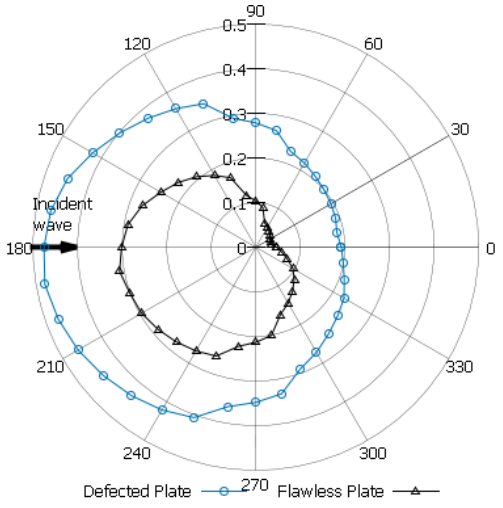

(b)

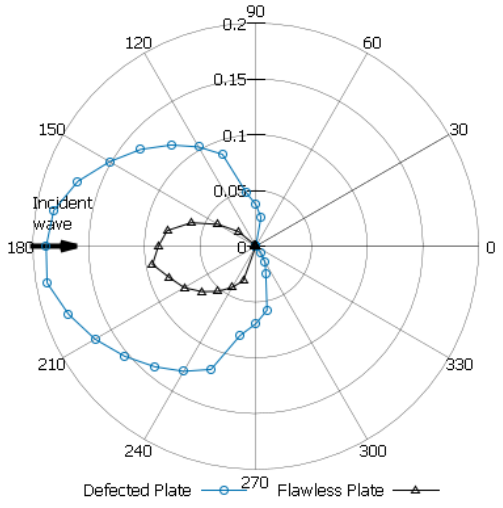

(c)

Fig. 6.9: Amplitude comparison between the flawless plate and defected plate during the interaction of 30 kHz incident A_0-mode Lamb wave and 1 mm subsurface defect after 14 μs of the excitement at the boundary of the defect for (a) $[0]_8$ laminate, (b) $[30]_8$ laminate, (c) $[60]_8$ laminate.

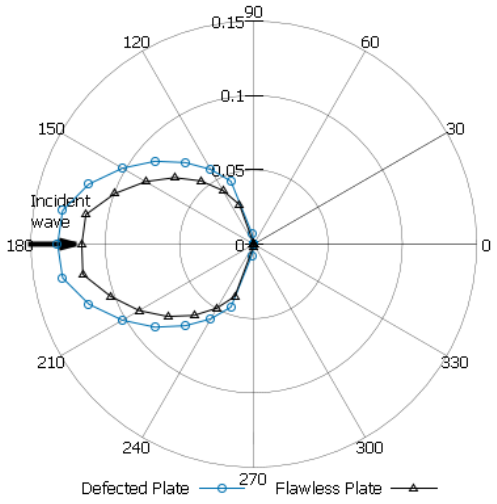

(a)

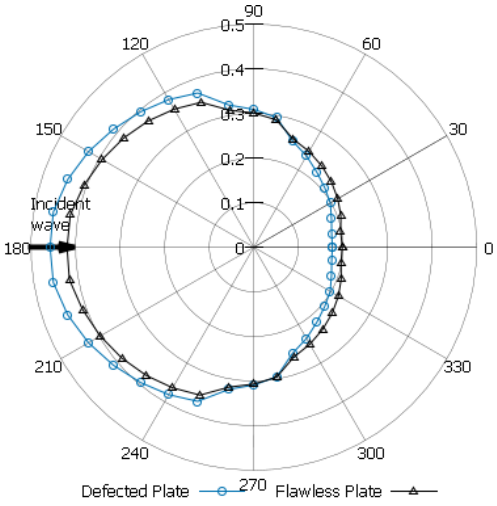

(b)

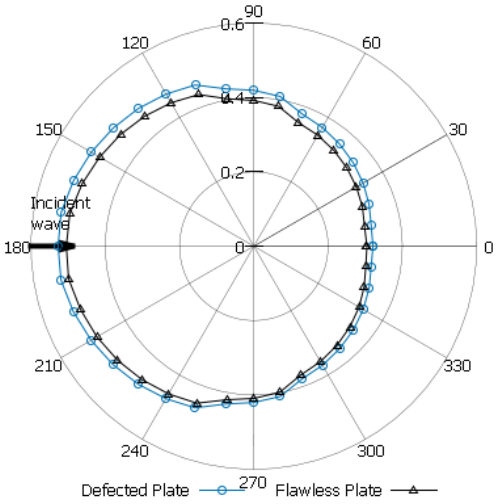

(c)

Fig. 6.10: Amplitude comparison between the flawless plate and defected plate during the interaction of 30 kHz incident A_0-mode Lamb wave and 1 mm subsurface defect after 14 μs of the excitement at the boundary of the defect for (a) $[90]_8$ laminate, (b) $[(0,90)_2]_s$ laminate, (c) $[0,\pm45,90]_s$ laminate.

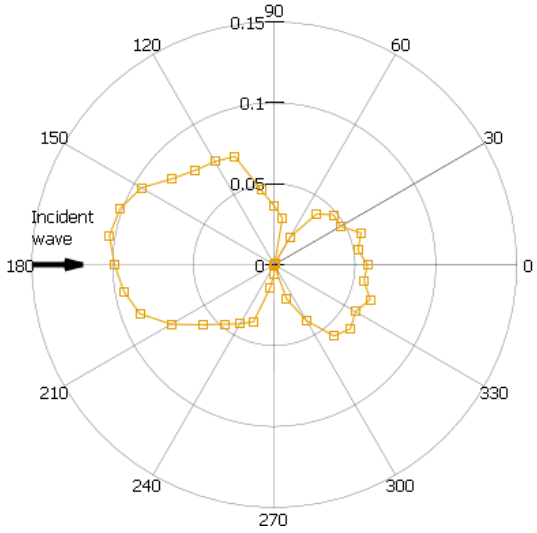

(a)

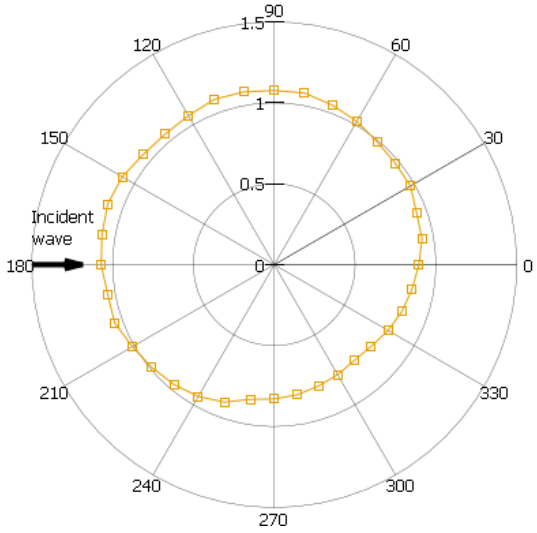

(b)

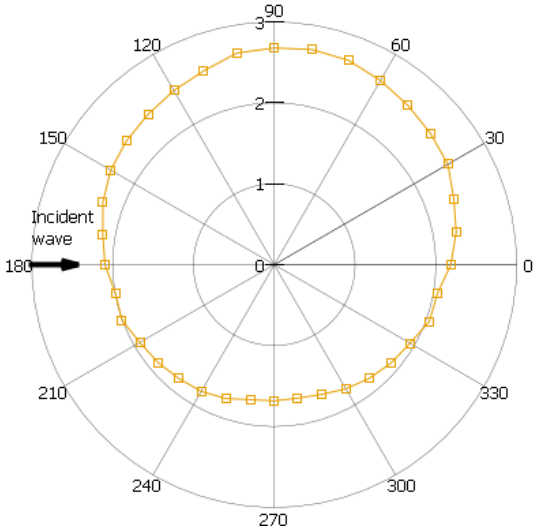

(c)

Fig. 6.11: DP for (a) $[0]_8$ laminate, (b) $[30]_8$ laminate, (c) $[60]_8$ laminate at the boundary of the subsurface defect after interaction with 30 kHz incident wave.

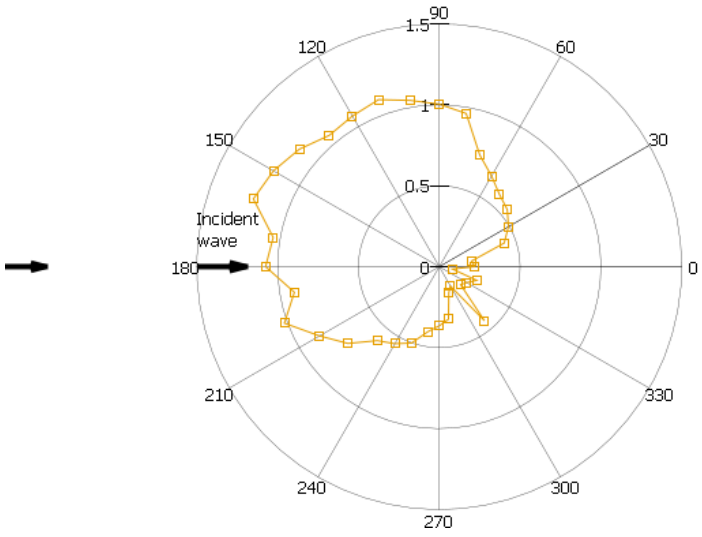

(a)

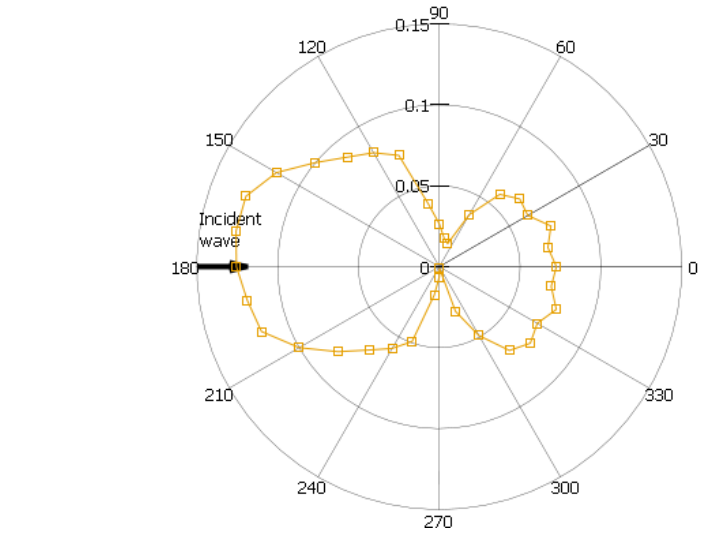

(b)

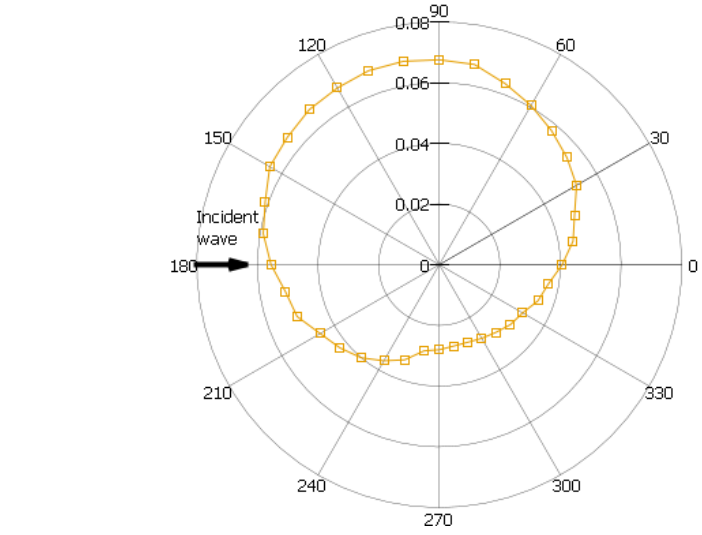

(c)

Fig. 6.12: DP for (a) $[90]_8$ laminate, (b) $[(0,90)_2]_s$ laminate, (c) $[0,\pm45,90]_s$ laminate at the boundary of the subsurface defect after interaction with 30 kHz incident wave.

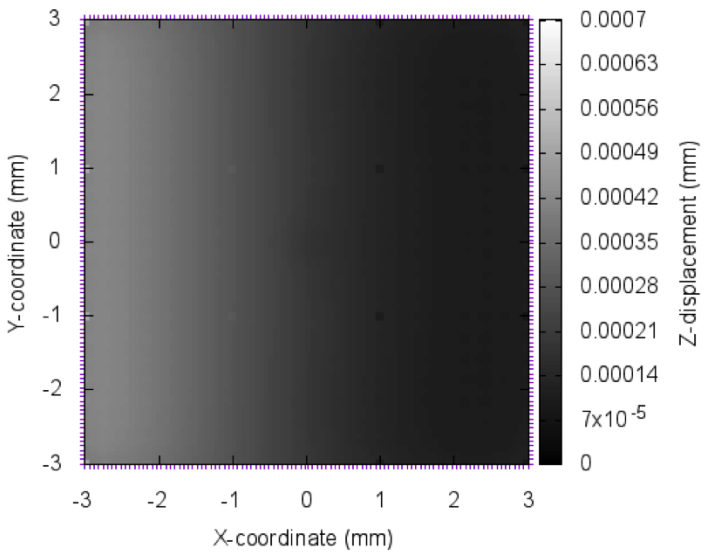

Fig. 6.13: Out-of-plane displacement distribution in a $[0]_8$ flawless laminate after 7 μs micro-s of irradiation

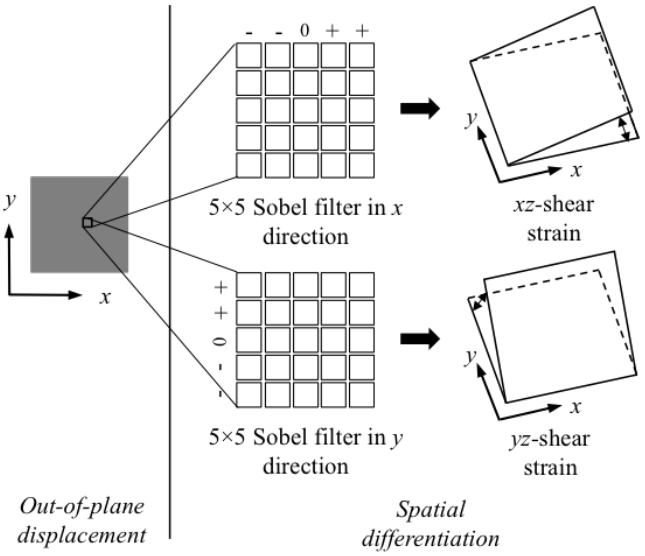

Fig. 6.14: Analysis process of orthogonal pair of shear strains by *Sobel* filtering

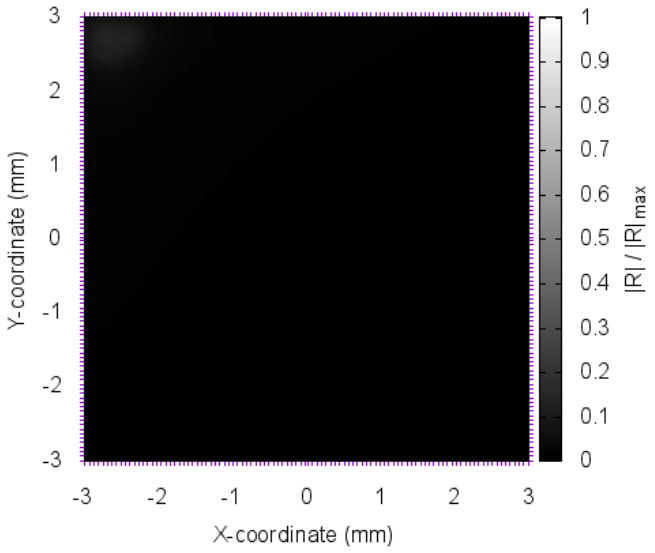

Fig. 6.15: Calculated determinant of the covariance matrix corresponding to the out-of-plane displacement in a flawless specimen, normalized by its maximum value

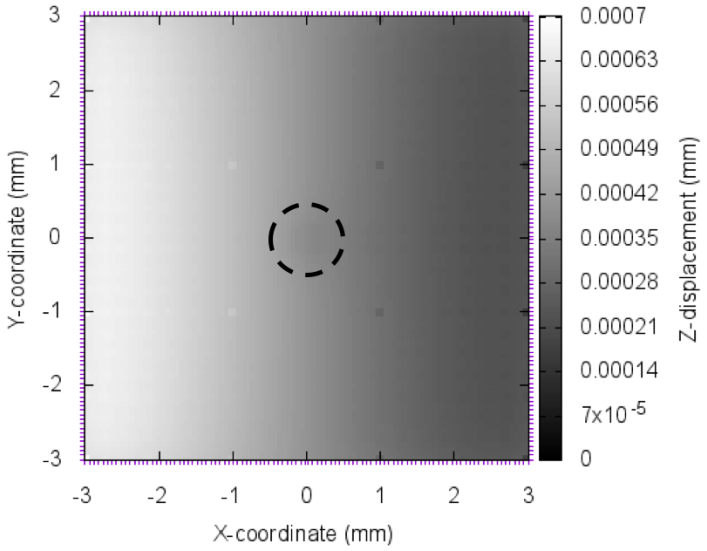

(a) Distributions of out-of-surface displacement

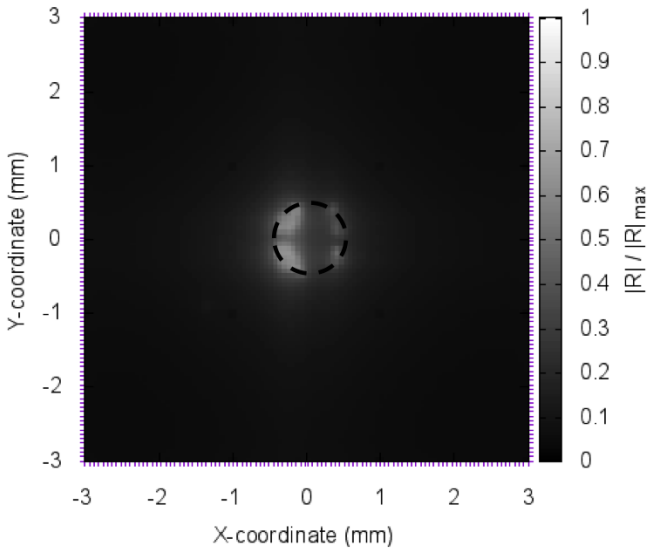

(b) Distributions of the determinant of covariance matrix normalized by the maximum value

Fig. 6.16: Snapshot of out-of-surface displacement and calculated distribution of normalized determinant after 14 μs after irradiation for $[0]_8$ laminate (dashed circle indicates the original position of artificial cylindrical defect)

.

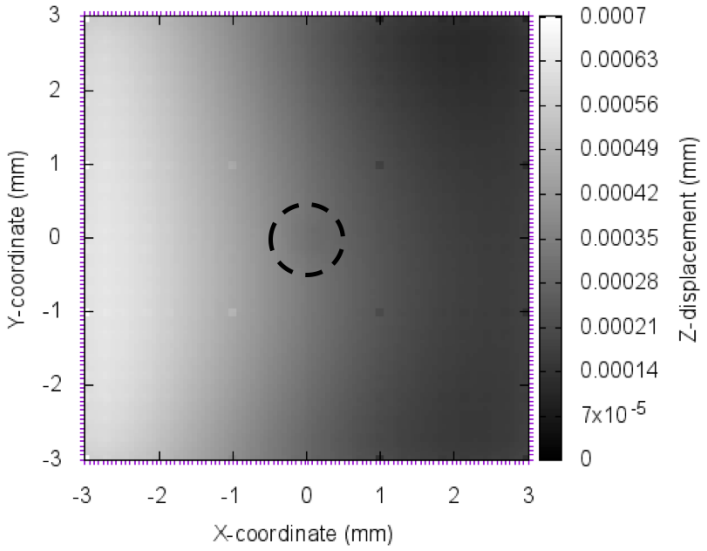

(a) Distributions of out-of-surface displacement

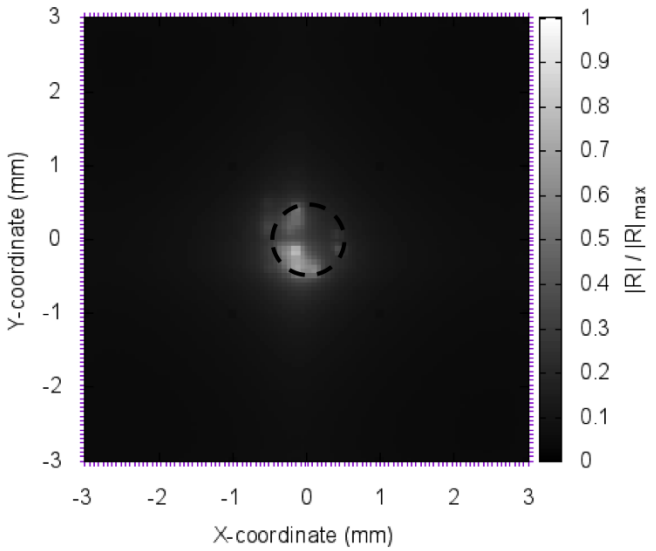

(b) Distributions of the determinant normalized by the maximum value

Fig. 6.17: Snapshot of out-of-surface displacement and calculated distribution of normalized determinant after 14 μs after irradiation for $[30]_8$ laminate (dashed circle indicates the original position of artificial cylindrical defect)

.

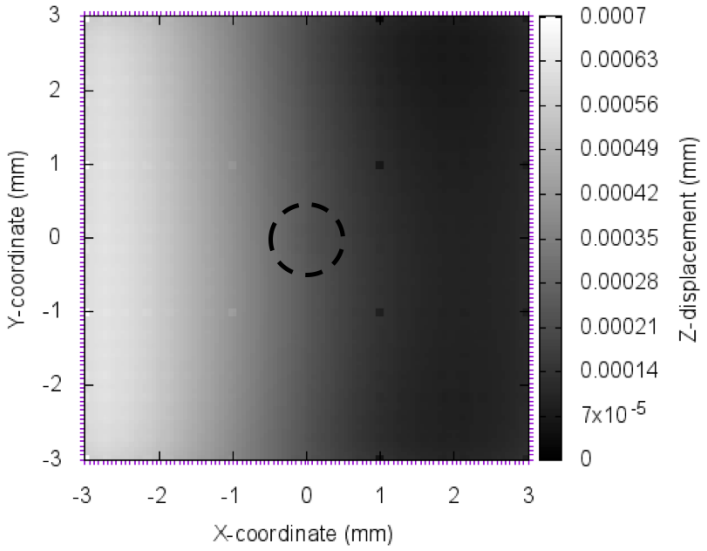

(a) Distributions of out-of-surface displacement

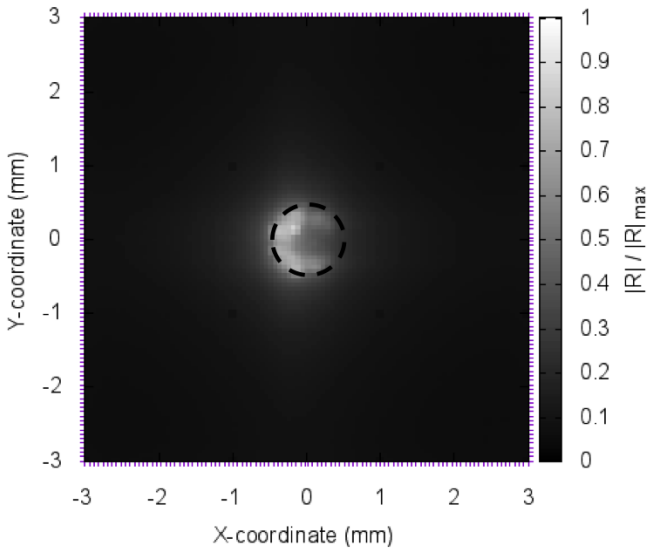

(b) Distributions of the determinant normalized by the maximum value

Fig. 6.18: Snapshot of out-of-surface displacement and calculated distribution of normalized determinant after 14 μs after irradiation for $[60]_8$ laminate (dashed circle indicates the original position of artificial cylindrical defect)

.

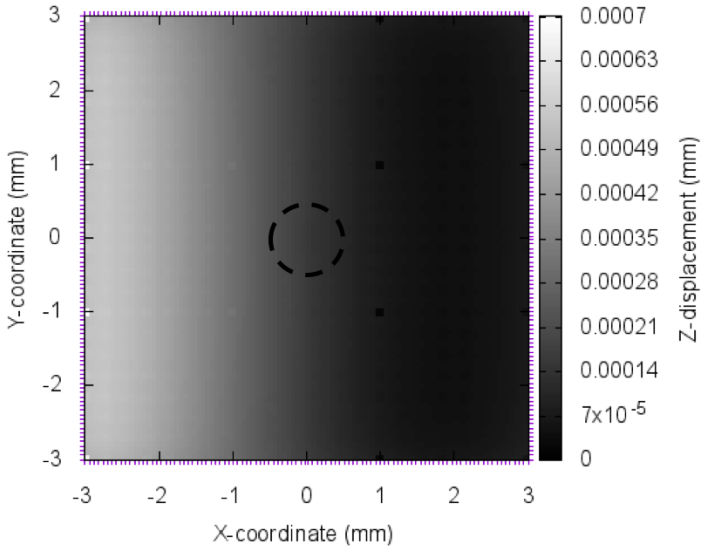

(a) Distributions of out-of-surface displacement

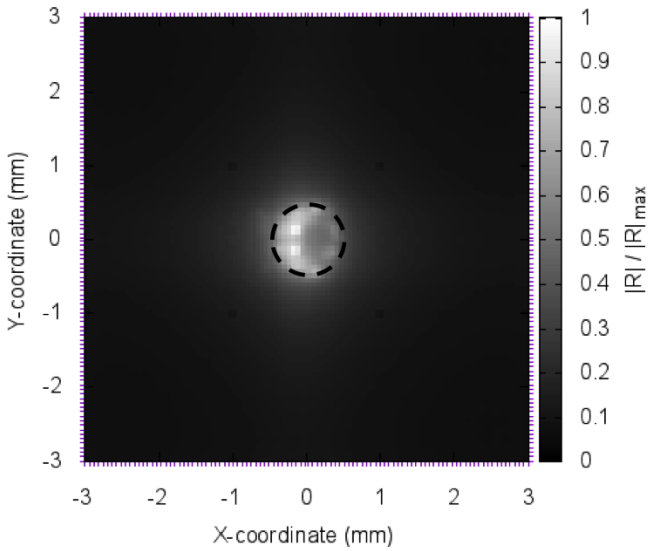

(b) Distributions of the determinant normalized by the maximum value

Fig. 6.19: Snapshot of out-of-surface displacement and calculated distribution of normalized determinant after 14 μs after irradiation for $[90]_8$ laminate (dashed circle indicates the original position of artificial cylindrical defect)

.

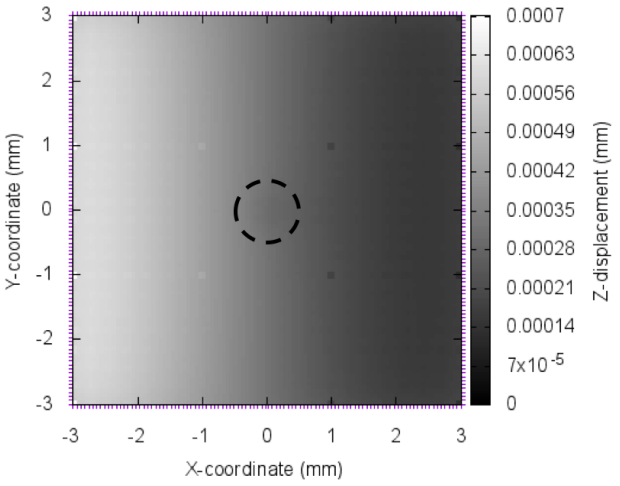

(a) Distributions of out-of-surface displacement

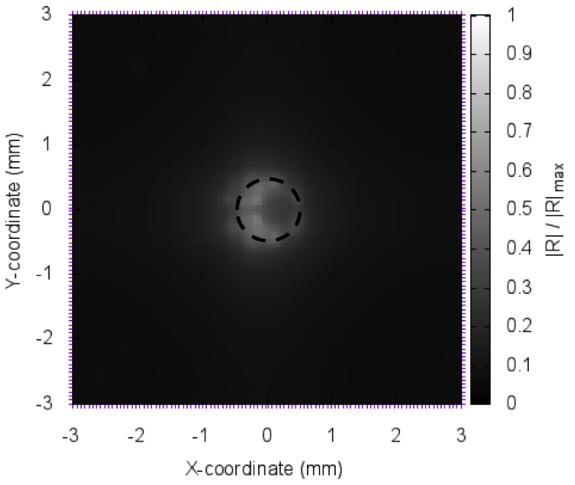

(b) Distributions of the determinant normalized by the maximum value

Fig. 6.20: Snapshot of out-of-surface displacement and calculated distribution of normalized determinant after 14 μs after irradiation for $[(0,90)_2]_s$ laminate (dashed circle indicates the original position of artificial cylindrical defect).

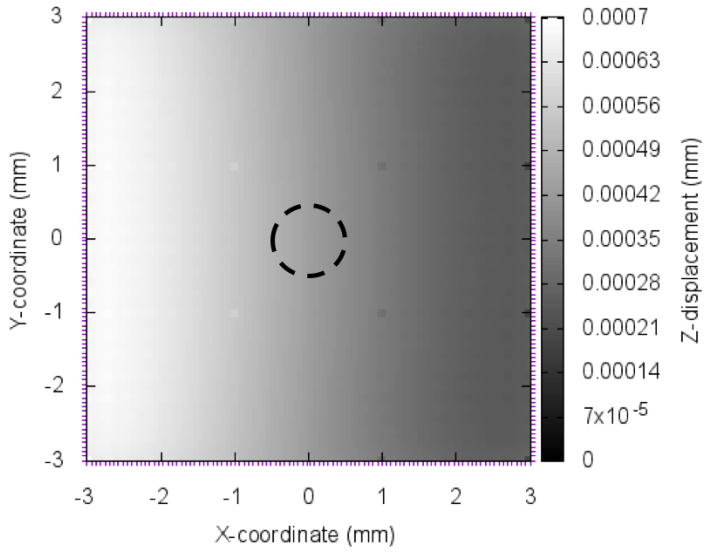

(a) Distributions of out-of-surface displacement

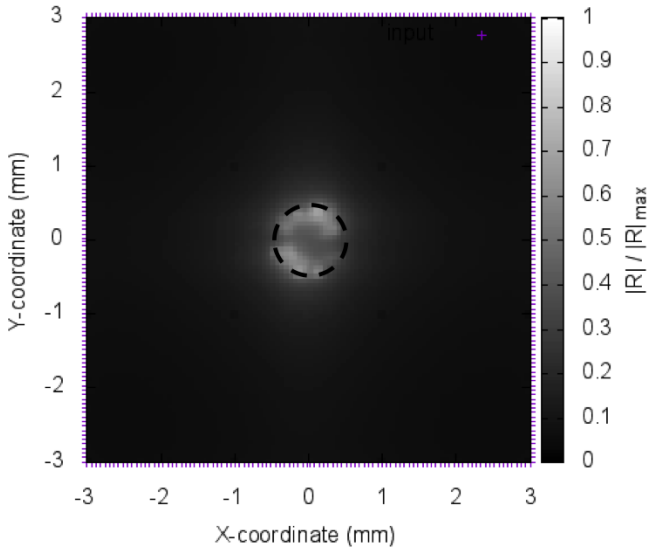

(b) Distributions of the determinant normalized by the maximum value

Fig. 6.21: Snapshot of out-of-surface displacement and calculated distribution of normalized determinant after 14 μs after irradiation for $[0, \pm 45, 90]_s$ laminate (dashed circle indicates the original position of artificial cylindrical defect).

7

CONCLUSION

Lamb waves can propagate in thin plate-like structures i.e., in metallic plates and fibre-reinforced composite laminates, including symmetric (S_i) and antisymmetric (A_i) modes. Lamb waves feature some unique and complex properties, including dispersion, mode conversion, directional dependence of wave speed, the difference in phase and group velocities. These mechanisms give Lamb waves sensitive to damage in structures. Taking advantage of recent advances and technical breakthroughs in sensor technology, manufacturing, electronic packaging, signal processing, informatics, diagnostics, applied mechanics and material sciences, damage identification and structural health monitoring (SHM) techniques using Lamb waves have been the subject of intensive research and development in the past decades. Now on the verge of maturity for diverse engineering applications, this emerging technique has exciting potential to facilitate continuous and automated surveillance of the integrity of engineering structures in a cost-effective manner.

In this research, key aspects concerning understanding, developing and implementing A_0-mode Lamb wave based subsurface damage identification and SHM are explained from theoretical fundamentals to engineering applications. Both of the fundamental modes can be used for identifying damage, though the antisymmetric mode outperforms the symmetric pair in two ways: one, it is sensitive to vertical cracks and two, it offers shorter wavelength, larger magnitude and greater ease of activation. Analytical study of the incident, scattered and transmitted A_0-mode Lamb wave field is elaborated significantly for isotropic as well as for TI material. Besides that, phase velocity equation is derived for TI material, and dispersion curves are drawn based on the properties of the carbon-epoxy combination. Unidirectional, Bidirectional and Quasi-isotropic combinations are considered to interrogate subsurface damage.

Damage identification using algorithms based on imaging approaches has in-

creasingly been adopted for practical application due to obvious advantages including the intuitive depiction of damage and potential to depict multiple damages. In particular, various signal features, such as ToFs can be used to construct an image presenting the probability of the presence of damage. But the ToF based technique face difficulty to the dispersive behavior of Lamb waves. Avoiding difficulties caused by such property, a quantitative near-field acoustical imaging technique is applied to classify the subsurface defected region within the composite laminates. This novel technique estimates elasticity characteristics of the area of interest somewhat inhomogeneity contrasted to the surrounded materials. However, an overlap of strong incident waves with the weak scattered waves is arduous to elucidate from the observed signals. The discussed imaging method utilizes the determinant of covariance matrix comprised of shear strains calculated from the out-of-plane displacements, observed on the top surface of the object. The determinant particularly denotes the distribution of correlated intensity modulation of the incident wavefronts with scattered ones and shows significant value in the overlapping region. The image reconstruction technique can be summarized in following steps:

1. gathering a time series data of out-of-plane displacement of the top surface
2. calculating the orthogonal set of out-of-plane shear strains
3. deducting the determinant of covariance matrix formulated with above vector
4. reconstructing the silhouette wave frontal image surround the defected region

The propagation characteristics of Lamb waves and the physical interpretation of the dynamic shear strain analysis are explored in terms of FEM. The subsurface defected plate is prepared by introducing an artificial cylindrical defect of 1 mm in diameter. The 3D model is created with the combination of eight-noded solid elements and six-noded wedge elements under the Multiphysics platform LS-DYNA. The zero-strain condition is considered in all surfaces except the source. A mono-cycle sinusoidal wave of 30 kHz is generated and the vertical particles out-of-plane displacement is observed

throughout the entire simulation time. The interaction between the A_0-mode Lamb wave and the subsurface defect is investigated through the directivity pattern of the scattered wave at the boundary of the defect. It is found that the fiber orientation of laminate made the significant effect on scattering. Recorded time series displacement data further analyzed through *Sobel* filter and a decaying series to reconstruct the image of the defect. The numerically simulated results depict in good agreement with the analytical assumption. In every case, it is proved that the determinant of the adopted covariance matrix based on the orthogonal pair of out-of-surface shear strain vector can detect the linearity violation points. Thus, it can be concluded that, the proposed novel method can detect subsurface damage in CFRP.

7.1 FUTURE WORK

Realistic model of defect

An only cylindrical subsurface defect in a flat plate has been studied in this thesis. But in the real world, the shape of the damage might not be perfectly cylindrical and the plate to be interrogated might have a different shape (Fig.7.1). So, models will have to be performed in two major steps. First, the variation of defect shape with the 2D model should be considered and second, one can move on to 3D plate design and study more pragmatic defects.

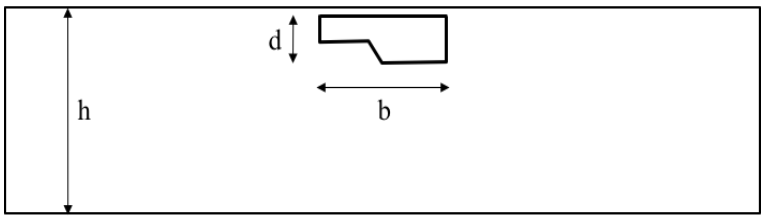

Fig. 7.1: Example of defect to be studied

Dynamic shear strain analysis developed on the incident of the plane wave at the defect and the corresponding scattering from that. In the analytical analysis, it is difficult to model the plane wave equation for calculating spatial shear strain in case of anisotropic material as the wave number does not direct to the wave propagation direction. Next step should have to taken to model the Hanning windowed wavelet and make the analysis accordingly. In such case, equation (3.42) can be considered as the equation of incident wave. Schematic of such model to be analyzed can be shown in Fig.7.2. As the technique developed to measure the points within the evanescent wave region, scattered wavefield particularly will not cause any effect in the analysis.

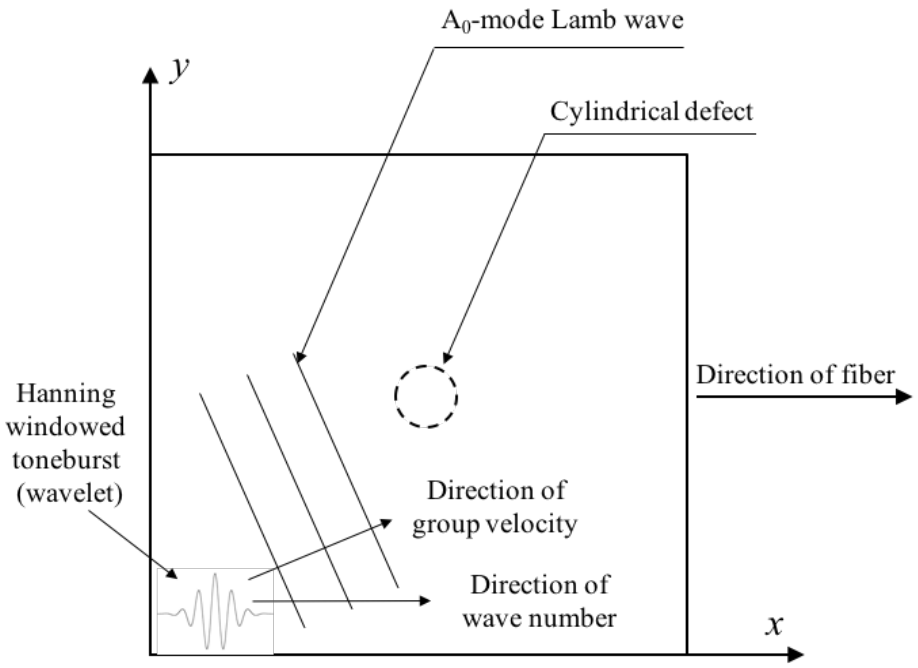

Fig. 7.2: A wavelet advancing toward the defect in anisotropic material

Using higher modes

The present study on dynamic shear strain analysis solely focuses on A_0-mode. Though, in the low-frequency region, this mode can play the significant role, a better approach may be to use a higher order mode such as A_1. The higher operating frequency is the advantage of using higher mode as a better resolution can be achieved.

In comparison with conventional NDE techniques such as ultrasonic scan and radiography which have been well developed over decades, damage identification and SHM using ultrasonic wave field imaging have been in a stage to play a vital role as an emerging tool of NDE. With authors outlook upon further development of this technique for practical applications, it is envisioned that the new research will have to address all issues discussed in this section in the coming years.

BIBLIOGRAPHY

[1] R.E. Green A.S. Birks P. McIntire. *ASNT Nondestructive Testing Handbook: Ultrasonic Testing*. Vol. 7. American Society for Nondestructive Testing, 2007.

[2] Milton Abramowitz and Irene A Stegun. *Handbook of mathematical functions: with formulas, graphs, and mathematical tables*. Vol. 55. Courier Corporation, 1964.

[3] J Achenbach. *Wave propagation in elastic solids*. Vol. 16. Elsevier, 2012.

[4] JD Achenbach. "Quantitative nondestructive evaluation". In: *International Journal of Solids and Structures* 37.1 (2000), pp. 13–27.

[5] JD Achenbach and A ZULFIQAR. "Techniques and instrumentation for structural diagnostics". In: *Structural Health Monitoring* 27.10 (1998), pp. 179–190.

[6] E Koray Akdogan, Mehdi Allahverdi, and Ahmad Safari. "Piezoelectric composites for sensor and actuator applications". In: *IEEE transactions on ultrasonics, ferroelectrics, and frequency control* 52.5 (2005), pp. 746–775.

[7] David N Alleyne and Peter Cawley. "The interaction of Lamb waves with defects". In: *IEEE transactions on ultrasonics, ferroelectrics, and frequency control* 39.3 (1992), pp. 381–397.

[8] Bertram Alexander Auld. *Acoustic fields and waves in solids*. ????? ???????, 1973.

[9] M Salim Azzouz et al. "Finite element modeling of MFC/AFC actuators and performance of MFC". In: *Journal of Intelligent Material Systems and Structures* 12.9 (2001), pp. 601–612.

[10] RA Badcock and EA Birt. "The use of 0-3 piezocomposite embedded Lamb wave sensors for detection of damage in advanced fibre composites". In: *Smart Materials and Structures* 9.3 (2000), p. 291.

[11] Andrey Bakulin, Vladimir Grechka, and Ilya Tsvankin. "Estimation of fracture parameters from reflection seismic data Part I: HTI model due to a single fracture set". In: *Geophysics* 65.6 (2000), pp. 1788–1802.

[12] Minhang Bao. *Analysis and design principles of MEMS devices*. Elsevier, 2005.

[13] Panagiotis Blanas and DK Das-Gupta. "Composite piezoelectric sensors for smart composite structures". In: *Electrets, 1999. ISE 10. Proceedings. 10th International Symposium on*. IEEE. 1999, pp. 731–734.

[14] FYC Boey and SW Lye. "Void reduction in autoclave processing of thermoset composites: Part 1: High pressure effects on void reduction". In: *Composites* 23.4 (1992), pp. 261–265.

[15] C Boller. "Ways and options for aircraft structural health management". In: *Smart materials and structures* 10.3 (2001), p. 432.

[16] M Castaings and B Hosten. "Lamb and SH waves generated and detected by air-coupled ultrasonic transducers in composite material plates". In: *Ndt & E International* 34.4 (2001), pp. 249–258.

[17] Michel Castaings and Peter Cawley. "The generation, propagation, and detection of Lamb waves in plates using air-coupled ultrasonic transducers". In: *The Journal of the Acoustical Society of America* 100.5 (1996), pp. 3070–3077.

[18] FB Cegla, A Rohde, and M Veidt. "Analytical prediction and experimental measurement for mode conversion and scattering of plate waves at non-symmetric circular blind holes in isotropic plates". In: *Wave Motion* 45.3 (2008), pp. 162–177.

[19] YT Chan. *Wavelet basics*. Springer Science & Business Media, 2012.

[20] J David N Cheeke. *Fundamentals and applications of ultrasonic waves*. CRC press, 2012.

[21] PT Cole. "Using acoustic emission (AE) to locate and identify defects in composite structures". In: *Composite structures* 3.3 (1985), pp. 259–267.

[22] Stuart Crampin. "Effects of point singularities on shear-wave propagation in sedimentary basins". In: *Geophysical Journal International* 107.3 (1991), pp. 531–543.

[23] Sujit Das et al. “Global Carbon Fiber Composites Supply Chain Competitiveness Analysis”. In: *Contract* (2016).

[24] WA De Morais and SN Monteiro. “Effect of the laminate thickness on the composite strength to repeated low energy impacts”. In: *Composite structures* 70.2 (2005), pp. 223–228.

[25] FL Degertakin and BT Khuri-Yakub. “Lamb wave excitation by Hertzian contacts with applications in NDE”. In: *ieee transactions on ultrasonics, ferroelectrics, and frequency control* 44.4 (1997), pp. 769–779.

[26] K Diamanti, JM Hodgkinson, and C Soutis. “Damage detection of composite laminates using PZT generated Lamb waves”. In: *1st European Workshop on Structural Health Monitoring*. 2002, pp. 398–405.

[27] EK Dimitriadis, CR Fuller, and CA Rogers. “Piezoelectric actuators for distributed noise and vibration excitation of thin plates”. In: *Failure prevention and reliability- 1989* (1989), pp. 223–233.

[28] JJ Ditri and K Rajana. “An experimental study of the angular dependence of Lamb wave excitation amplitudes”. In: *Journal of sound and vibration* 204.5 (1997), pp. 755–768.

[29] Weimin Gao, Christ Glorieux, and Jan Thoen. “Laser ultrasonic study of Lamb waves: determination of the thickness and velocities of a thin plate”. In: *International journal of engineering science* 41.2 (2003), pp. 219–228.

[30] DS Gardiner and LH Pearson. “Acoustic-Emission Monitoring of Composite Damage Occurring Under Static and Impact Loading”. In: *Experimental Techniques* 9.11 (1985), pp. 22–28.

[31] T Ghosh, T Kundu, and P Karpur. “Efficient use of Lamb modes for detecting defects in large plates”. In: *Ultrasonics* 36.7 (1998), pp. 791–801.

[32] Tomas Grahn. “Lamb wave scattering from a circular partly through-thickness hole in a plate”. In: *Wave Motion* 37.1 (2003), pp. 63–80.

[33] Sébastien Grondel et al. “Design of optimal configuration for generating A 0 Lamb mode in a composite plate using piezoceramic transducers”. In: *The Journal of the Acoustical Society of America* 112.1 (2002), pp. 84–90.

[34] XE Gros, K Ogi, and K Takahashi. "Eddy current, ultrasonic C-scan and scanning acoustic microscopy testing of delaminated quasi-isotropic CFRP materials: a case study". In: *Journal of reinforced plastics and composites* 17.5 (1998), pp. 389–405.

[35] XE Gros, K Takahashi, and M de Smet. "On the efficiency of current NDT methods for impact damage detection and quantification in thermoplastic toughened CFRP materials". In: *Journal of Nondestructive Testing & Ultrasonics(Germany)* 4.3 (1999).

[36] Xavier E Gros. "An eddy current approach to the detection of damage caused by low-energy impacts on carbon fibre reinforced materials". In: *Materials & Design* 16.3 (1995), pp. 167–173.

[37] Zhiqi Guo, JD Achenbach, and Sridhar Krishnaswamy. "EMAT generation and laser detection of single lamb wave modes". In: *Ultrasonics* 35.6 (1997), pp. 423–429.

[38] Ronald Halmshaw, RWK Honeycombe, and P Hancock. *Non-destructive testing*. Arnold, 1991.

[39] TR Hay et al. "A comparison of embedded sensor Lamb wave ultrasonic tomography approaches for material loss detection". In: *Smart Materials and Structures* 15.4 (2006), p. 946.

[40] Klaus Helbig. *Foundations of anisotropy for exploration seismics*. Pergamon, 1994.

[41] K Heller, LJ Jacobs, and J Qu. "Characterization of adhesive bond properties using Lamb waves". In: *NDT & E International* 33.8 (2000), pp. 555–563.

[42] Manfred P Hentschel et al. "New X. ray refractography for nondestructive investigations". In: (1994).

[43] Jidong Hou, Kevin R Leonard, and Mark K Hinders. "Automatic multimode Lamb wave arrival time extraction for improved tomographic reconstruction". In: *Inverse Problems* 20.6 (2004), p. 1873.

[44] Derek Hull and TW Clyne. *An introduction to composite materials*. Cambridge university press, 1996.

[45] Stefan Hurlebaus and Lothar Gaul. “Smart layer for damage diagnostics”. In: *Journal of intelligent material systems and structures* 15.9-10 (2004), pp. 729–736.

[46] Ros K Ing and Mathias Fink. “Time-reversed Lamb waves”. In: *IEEE transactions on ultrasonics, ferroelectrics, and frequency control* 45.4 (1998), pp. 1032–1043.

[47] Serope Kalpakjian. *Manufacturing engineering and technology*. Pearson Education India, 2001.

[48] Seth S Kessler, S Mark Spearing, and Constantinos Soutis. “Damage detection in composite materials using Lamb wave methods”. In: *Smart Materials and Structures* 11.2 (2002), p. 269.

[49] Yoon Young Kim and Eung-Hun Kim. “Effectiveness of the continuous wavelet transform in the analysis of some dispersive elastic waves”. In: *The Journal of the Acoustical Society of America* 110.1 (2001), pp. 86–94.

[50] YL Koh, WK Chiu, and N Rajic. “Effects of local stiffness changes and delamination on Lamb wave transmission using surface-mounted piezoelectric transducers”. In: *Composite Structures* 57.1 (2002), pp. 437–443.

[51] Mukunthan Krishnapillai et al. “Thermography as a tool for damage assessment”. In: *Composite structures* 67.2 (2005), pp. 149–155.

[52] Michael Kühnel and Thomas Kraus. “The global CFRP market 2016”. In: (2016).

[53] Tribikram Kundu et al. “A Lamb wave scanning approach for the mapping of defects in [0/90] titanium matrix composites”. In: *Ultrasonics* 34.1 (1996), pp. 43–49.

[54] Horace Lamb. “On waves in an elastic plate”. In: *Proceedings of the Royal Society of London A: Mathematical, Physical and Engineering Sciences*. Vol. 93. 648. The Royal Society. 1917, pp. 114–128.

[55] TH Loutas, G Sotiriades, and V Kostopoulos. “On the application of wavelet transform of AE signals from composite materials”. In: *Proc. of European WG on AE, Berlin* 42 (2004), pp. 433–445.

[56] AEH Love. *Some Problems of Geodynamics (1911)*.

[57] Mike JS Lowe et al. “The low frequency reflection characteristics of the fundamental antisymmetric Lamb wave a 0 from a rectangular notch in a plate”. In: *The Journal of the Acoustical Society of America* 112.6 (2002), pp. 2612–2622.

[58] F Mili and B Necib. “The effect of stacking sequence on the impact-induced damage in cross-ply E-glass/epoxy composite plates”. In: *Archive of Applied Mechanics* 79.11 (2009), pp. 1019–1031.

[59] Ronnie K Miller and Paul McIntire. “Nondestructive Testing Handbook. Vol. 5: Acoustic Emission Testing”. In: *American Society for Nondestructive Testing, 4153 Arlingate Plaza, Caller# 28518, Columbus, Ohio 43228, USA, 1987. 603* (1987).

[60] RSC Monkhouse, PD Wilcox, and P Cawley. “Flexible interdigital PVDF transducers for the generation of Lamb waves in structures”. In: *Ultrasonics* 35.7 (1997), pp. 489–498.

[61] RSC Monkhouse et al. “The rapid monitoring of structures using interdigital Lamb wave transducers”. In: *Smart Materials and Structures* 9.3 (2000), p. 304.

[62] Riichi Murayama and Koichi Mizutani. “Conventional electromagnetic acoustic transducer development for optimum Lamb wave modes”. In: *Ultrasonics* 40.1 (2002), pp. 491–495.

[63] Alan Musgrave et al. *Criticism and the Growth of Knowledge: Volume 4: Proceedings of the International Colloquium in the Philosophy of Science, London, 1965*. Vol. 4. Cambridge University Press, 1970.

[64] Alan T Nettles. “Basic mechanics of laminated composite plates”. In: (1994).

[65] Ching-Tai Ng and M Veidt. “A Lamb-wave-based technique for damage detection in composite laminates”. In: *Smart materials and structures* 18.7 (2009), p. 074006.

[66] Ching-Tai Ng and Martin Veidt. “Scattering of the fundamental anti-symmetric Lamb wave at delaminations in composite laminates”. In: *The Journal of the Acoustical Society of America* 129.3 (2011), pp. 1288–1296.

[67] Nan Pan et al. “A quantitative identification approach for delamination in laminated composite beams using digital damage fingerprints (DDFs)”. In: *Composite structures* 75.1 (2006), pp. 559–570.

[68] Walter L Pilant. “Complex roots of the Stoneley-wave equation”. In: *Bulletin of the Seismological Society of America* 62.1 (1972), pp. 285–299.

[69] Jürgen Pohl. “Ultrasonic inspection of adaptive CFRP-structures”. In: *NDT Database & Journal* 3.9 (1998).

[70] Catherine Potel et al. “Deviation of a monochromatic Lamb wave beam in anisotropic multilayered media: Asymptotic analysis, numerical and experimental results”. In: *ieee transactions on ultrasonics, ferroelectrics, and frequency control* 52.6 (2005), pp. 987–1001.

[71] Jianmin Qu. “Scattering of plane waves from an interface crack”. In: *International journal of engineering science* 33.2 (1995), pp. 179–194.

[72] Baldev Raj, Tammana Jayakumar, and M Thavasimuthu. *Practical non-destructive testing*. Woodhead Publishing, 2002.

[73] Lord Rayleigh. “On waves propagated along the plane surface of an elastic solid”. In: *Proceedings of the London Mathematical Society* 1.1 (1885), pp. 4–11.

[74] Brad Regez and Sridhar Krishnaswamy. “Nondestructive Evaluation of Structures”. In: *Encyclopedia of Aerospace Engineering* (2010).

[75] AH Rohde et al. “A computer simulation study of imaging flexural inhomogeneities using plate-wave diffraction tomography”. In: *Ultrasonics* 48.1 (2008), pp. 6–15.

[76] Joseph L Rose. *Ultrasonic waves in solid media*. 2000.

[77] Joseph L Rose. *Ultrasonic waves in solid media*. Cambridge university press, 2004.

[78] Riccardo Rubini and Menad Sidahmed. “Diagnostics of gear systems using the Spectral Correlation Density of the vibration signal”. In: *Proceedings of the IFAC Symposium on Fault Detection, Supervision and Safety for Technical Processes, Hull, United Kingdom*. 1997.

[79] JG Scholte. “The range of existence of Rayleigh and Stoneley waves”. In: *Geophysical Journal International* 5.s5 (1947), pp. 120–126.

[80] BV Soma Sekhar, Krishnan Balasubramaniam, and CV Krishnamurthy. "Structural health monitoring of fiber-reinforced composite plates for low-velocity impact damage using ultrasonic Lamb wave tomography". In: *Structural Health Monitoring* 5.3 (2006), pp. 243–253.

[81] Hoon Sohn and Charles R Farrar. "Damage diagnosis using time series analysis of vibration signals". In: *Smart materials and structures* 10.3 (2001), p. 446.

[82] Wieslaw Staszewski, Chr Boller, and Geoffrey R Tomlinson. *Health monitoring of aerospace structures: smart sensor technologies and signal processing*. John Wiley & Sons, 2004.

[83] ROBERT Stoneley. "Elastic waves at the surface of separation of two solids". In: *Proceedings of the Royal Society of London. Series A, Containing Papers of a Mathematical and Physical Character* 106.738 (1924), pp. 416–428.

[84] Zhongqing Su and Lin Ye. "A fast damage locating approach using digital damage fingerprints extracted from Lamb wave signals". In: *Smart materials and structures* 14.5 (2005), p. 1047.

[85] Zhongqing Su and Lin Ye. *Identification of damage using Lamb waves: from fundamentals to applications*. Vol. 48. Springer Science & Business Media, 2009.

[86] Zhongqing Su, Lin Ye, and Xiongzhu Bu. "A damage identification technique for CF/EP composite laminates using distributed piezoelectric transducers". In: *Composite structures* 57.1 (2002), pp. 465–471.

[87] Zhongqing Su, Lin Ye, and Ye Lu. "Guided Lamb waves for identification of damage in composite structures: A review". In: *Journal of sound and vibration* 295.3 (2006), pp. 753–780.

[88] Zhongqing Su et al. "Assessment of delamination in composite beams using shear horizontal (SH) wave mode". In: *Composites science and technology* 67.2 (2007), pp. 244–251.

[89] LS Sutherland and C Guedes Soares. "Effect of laminate thickness and of matrix resin on the impact of low fibre-volume, woven roving E-glass composites". In: *Composites science and technology* 64.10 (2004), pp. 1691–1700.

[90] Kenbu Teramoto and Ryoji Inoue. “Near-field Imaging of Defects Based on the Dynamic Shear Strain Analysis over the Ao-mode Lamb Wave Field”. In: *Transactions of the Society of Instrument and Control Engineers* 47.10 (2011), pp. 422–429.

[91] Leon Thomsen. “Weak elastic anisotropy”. In: *Geophysics* 51.10 (1986), pp. 1954–1966.

[92] N Toyama and J Takatsubo. “Lamb wave method for quick inspection of impact-induced delamination in composite laminates”. In: *Composites science and technology* 64.9 (2004), pp. 1293–1300.

[93] Ilya Tsvankin. *Seismic signatures and analysis of reflection data in anisotropic media*. Society of Exploration Geophysicists, 2012.

[94] SH Diaz Valdes and C Soutis. “A structural health monitoring system for laminated composites”. In: *Proceedings of DETC*. 2001, pp. 2013–2021.

[95] Christine Valle and Jerrol W Littles. “Flaw localization using the reassigned spectrogram on laser-generated and detected Lamb modes”. In: *Ultrasonics* 39.8 (2002), pp. 535–542.

[96] Martin Veidt, Tierang Liu, and Sritawat Kitipornchai. “Modelling of Lamb waves in composite laminated plates excited by interdigital transducers”. In: *Ndt & E International* 35.7 (2002), pp. 437–447.

[97] Chun H Wang, James T Rose, and Fu-Kuo Chang. “A synthetic time-reversal imaging method for structural health monitoring”. In: *Smart materials and structures* 13.2 (2004), p. 415.

[98] William J Wang. “Wavelets for detecting mechanical faults with high sensitivity”. In: *Mechanical systems and signal processing* 15.4 (2001), pp. 685–696.

[99] P Wilcox, M Lowe, and P Cawley. “The effect of dispersion on long-range inspection using ultrasonic guided waves”. In: *NDT & E International* 34.1 (2001), pp. 1–9.

[100] Paul D Wilcox et al. “Mode and transducer selection for long range Lamb wave inspection”. In: *Key Engineering Materials*. Vol. 167. Trans Tech Publ. 1999, pp. 152–161.

[101] DF Winterstein and Mark A Meadows. "Shear wave polarizations and subsurface stress directions at Lost Hills field". In: *Geophysics* 56.9 (1991), pp. 1331–1348.

[102] C Zang, M Imregun Friswell, and M Imregun. "Structural damage detection using independent component analysis". In: *Structural Health Monitoring* 3.1 (2004), pp. 69–83.

[103] GT Zheng and WJ Wang. "A new cepstral analysis procedure of recovering excitations from transient components of vibration signals and applications to rotating machinery condition monitoring". In: *Transactions of ASME*. 2001, pp. 222–229.

[104] GT Zheng et al. "Blind deconvolution of acoustic emission signals for damage identification in composites". In: *AIAA journal* 39.6 (2001), pp. 1198–1205.

[105] G Zhou. "Damage mechanisms in composite laminates impacted by a flat-ended impactor". In: *Composites Science and Technology* 54.3 (1995), pp. 267–273.